QUADRUPOLE COLLECTIVITY IN NEUTRON-DEFICIENT SN NUCLEI: ^{104}SN

By

Vincent Maximilian Bader

A DISSERTATION

Submitted to
Michigan State University
in partial fulfillment of the requirements
for the degree of

Physics - Doctor of Philosophy

2014

UMI Number: 3615483

UMI®
Dissertation Publishing

UMI 3615483

ProQuest®

ABSTRACT

QUADRUPOLE COLLECTIVITY IN NEUTRON-DEFICIENT SN NUCLEI: ^{104}SN

By

Vincent Maximilian Bader

This thesis is about the study of quadrupole collectivity in the neutron-deficient nucleus ^{104}Sn using intermediate-energy Coulomb excitation. The $B(E2; 0_1^+ \rightarrow 2_1^+)$ value for the excitation of the first 2^+ state in ^{104}Sn has been measured to be 0.180(37) e^2b^2 relative to the well-known $B(E2 \uparrow)$ value of ^{102}Cd. This result disagrees by more than one sigma with a recently published measurement [1]. The result indicates that the most modern many-body calculations remain unable to describe the enhanced collectivity below mid-shell in Tin approaching $N = Z = 50$. The enhanced collectivity is attributed to proton particle-hole configurations beyond the necessarily limited shell-model spaces and suggests the asymmetry of the $B(E2 \uparrow)$-value trend around mid-shell to originate from enhanced proton excitations across $Z = 50$ as $N = Z$ is approached.

Dedicated to my parents Verena Bader and Dr. Raoul Bader.

ACKNOWLEDGMENTS

First and foremost I would like to express my gratitude towards my adviser Alexandra Gade. She was always there to discuss ideas, answer my questions and help me out whenever I needed help. It was a great pleasure working with her. I would further like to thank my guidance committee for their support: Alex Brown, Phillip Duxbury, Wayne Repko and Michael Syphers. I would also like to give special thanks to Dirk Weisshaar without whom this experiment would not have succeeded. Furthermore I highly appreciate the help of Kathrin Wimmer who provided me with the root code for the analysis and Travis Baugher who provided me with the simulation code. Both endured countless times I bothered them with problems I encountered. There are many more people who have my thanks, all the people in the Gamma group at the *NSCL* and of course the staff working here. Not to forget my office mates Daniel Winklehner, Michael Jones and Michael Bennett who were a welcomed source of knowledge and distraction.

Last but not least I would like to thank my family without who this stay at MSU would not have been possible.

TABLE OF CONTENTS

LIST OF TABLES

LIST OF FIGURES

KEY TO SYMBOLS AND ABBREVIATIONS

A .... Atomic mass number (sum of neutrons and protons in a nucleus)

N .... Neutron number (number of neutrons in a nucleus)

Z .... Proton number (number of protons in a nucleus)

c .... Speed of light in vacuum ($\approx 3 \cdot 10^8$ m/s)

β .... Relativistic factor beta ($\beta = v/c$)

γ .... Relativistic factor gamma ($\gamma = 1/\sqrt{1 - \beta^2}$)

NSCL .... National Superconducting Cyclotron Laboratory

ECR ion source .... Electron Cyclotron Resonance ion source

ARTEMIS .... Advanced Room TEMperature Ion Source

K500 .... First cyclotron at the NSCL

K1200 .... Second cyclotron at the NSCL

A1900 .... Fragment separator at the NSCL

CAESAR .... High-efficiency CsI(Na) scintillator array; CAESium iodide ARray

RFFS .... Radio Frequency Fragment Separator

p-i-n detector .... Semiconductor detector used for energy loss measurements

PPAC .... Parallel Plate Avalanche Counter; used for position measurements

Phoswich detector .... Combination of two plastic scintillators

PMT .... Photomultiplier Tube

Chapter 1

Introduction and Motivation

One of the overarching goals of nuclear physics is the development of a comprehensive model of the atomic nucleus with predictive power across the nuclear chart. While the structure of nuclei close to stability is fairly well understood, significant modifications compared to stable nuclei have been observed for short-lived rare isotopes with unbalanced numbers of protons and neutrons. The driving forces behind these structural changes are manifold, including spin-isospin parts of the nuclear interaction [26] and various facets of many-body correlations [27]. Of particular importance for the development of nuclear models is experimental data that consistently tracks the effect of isospin and changed nuclear binding energies, for example. The chain of Sn isotopes has been a formidable testing ground for nuclear models as some spectroscopic data is available from $N = Z = 50$ ^{100}Sn [28] in the proximity of the proton drip-line to ^{134}Sn [29], beyond the very neutron-rich doubly-magic nucleus (nucleus with a *magic number* of neutrons and protons, see Sec. 2) ^{132}Sn [30]. In even-even nuclei (even number of protons and neutrons), the electromagnetic $B(E2 \uparrow) = B(E2; 0_1^+ \to 2_1^+)$ excitation strength is a measure of quadrupole collectivity (see Sec. 2.5), sensitive to the presence of shell gaps, nuclear deformation, and nucleon-nucleon correlations, for example. In the Sn isotopes, this transition strength has been reported from ^{104}Sn to ^{130}Sn, spanning a chain of 14 even-even Sn isotopes. The trend is asymmetric with respect to mid-shell and not even the largest-scale shell-model calculations have been able to describe the evolution of transition strength across the isotopic chain without varying effective charges. In this work,

the determination of the ^{104}Sn $B(E2\uparrow)$ value from intermediate-energy Coulomb excitation is reported. The value exceeds the recently published result [1] and – continuing the trend below mid-shell – is found at variance with the largest-scale shell-model calculations. It is though in agreement with the value from [7]. The drawn conclusion is very different from [1] and explains the enhanced collectivity for neutron-deficient Sn nuclei by considering proton particle-hole intruder configurations observed in neighboring nuclei and α correlations towards $N = Z$. It is suggested that the interplay of proton intruder configurations and quadrupole collectivity is a common phenomenon along proton-magic isotope chains.

Chapter 2

Physics of Nuclei

2.1 Atomic Nuclei

The atomic nucleus is a many-body quantum system. It consist of fermions, namely two types of nucleons, the protons and neutrons. Protons are positively charged and the neutrons are electrically neutral. A nucleus is made up of N neutrons and Z protons, resulting in the total number of $A = N + Z$ nucleons. A nucleus is typically referred to in the notation $^A X(Z)$, with $X(Z)$ being the chemical symbol of the element that has Z protons. Nuclei have typical radii of the order of 10 fm $= 10^{-14}$ m. The radius for nuclei near stability is usually approximated like this [31]:

$$R(A) = R_0 A^{\frac{1}{3}}, \tag{2.1}$$

with $R_0 = 1.25$ fm. Because the protons are positively charged, they are subject to the Coulomb force. This force is repulsive between protons and is proportional to $\frac{1}{r^2}$ and therefore, decreases fast with increasing radial distance. The neutrons are not affected by the Coulomb force due to their electrical neutrality. If there was only the Coulomb force, nuclear systems would not exist. The nucleons are bound together by the attractive *strong force*. This force has a typical range of the order of 10^{-14}-10^{-15} m which is of the order of the size of a nucleon [32]. It is charge independent, acts on neutrons as well as protons, and

is about 100 times stronger than the Coulomb force on the length scale of a nucleus but it is of negligible strength for longer distances. There are small difference in the strength of the attraction depending on the composition of a nucleon pair. The nucleon-nucleon force is charge symmetric, meaning that proton-proton and neutron-neutron interactions have the same strength and it is nearly charge independent, meaning that the proton-neutron interaction is only slightly different from the proton-proton interaction [31].

More than 3000 nuclei have been observed so far but only about 250 are stable and the unstable ones will eventually decay into stable nuclei. As a result of the Coulomb interaction, more neutron-rich than proton-rich nuclei exist. The boundary on the proton-rich side, the proton drip line, is more well defined than the boundary on the neutron rich side, the neutron drip line. This is because the proton drip line is closer to stability than the neutron drip line and thus easier to reach experimentally. The Coulomb force makes it harder to add protons than neutrons. A visualization of the nuclear landscape, the chart of nuclei, is shown in Fig. 2.1. The number of protons is plotted versus the number of neutrons. Each square represents a different nucleus. The black squares are the stable nuclei, the blue are the unstable but known nuclei and the red squares represent the nuclei that are assumed to exist but have not been observed yet. The so-called *magic numbers* (see below), 2, 8, 20, 28, 50, 82 and 126 are indicated as dashed lines.

There is plenty of evidence pointing to an internal structure of nuclei. The *binding energy*, $BE(N, Z)$ is the basis of four of those observables, the one-proton and -neutron *separation energies*, $S_p(N, Z)$ and $S_n(N, Z)$, and the difference in one-nucleon separation energies, $\Delta S_p(N, Z)$ and $\Delta S_n(N, Z)$. The *binding energy* of a nucleus is calculated by taking the difference of the sum of the rest mass energies of the individual nucleons building a nucleus and the measured rest mass energy of the bound nucleus itself [4]:
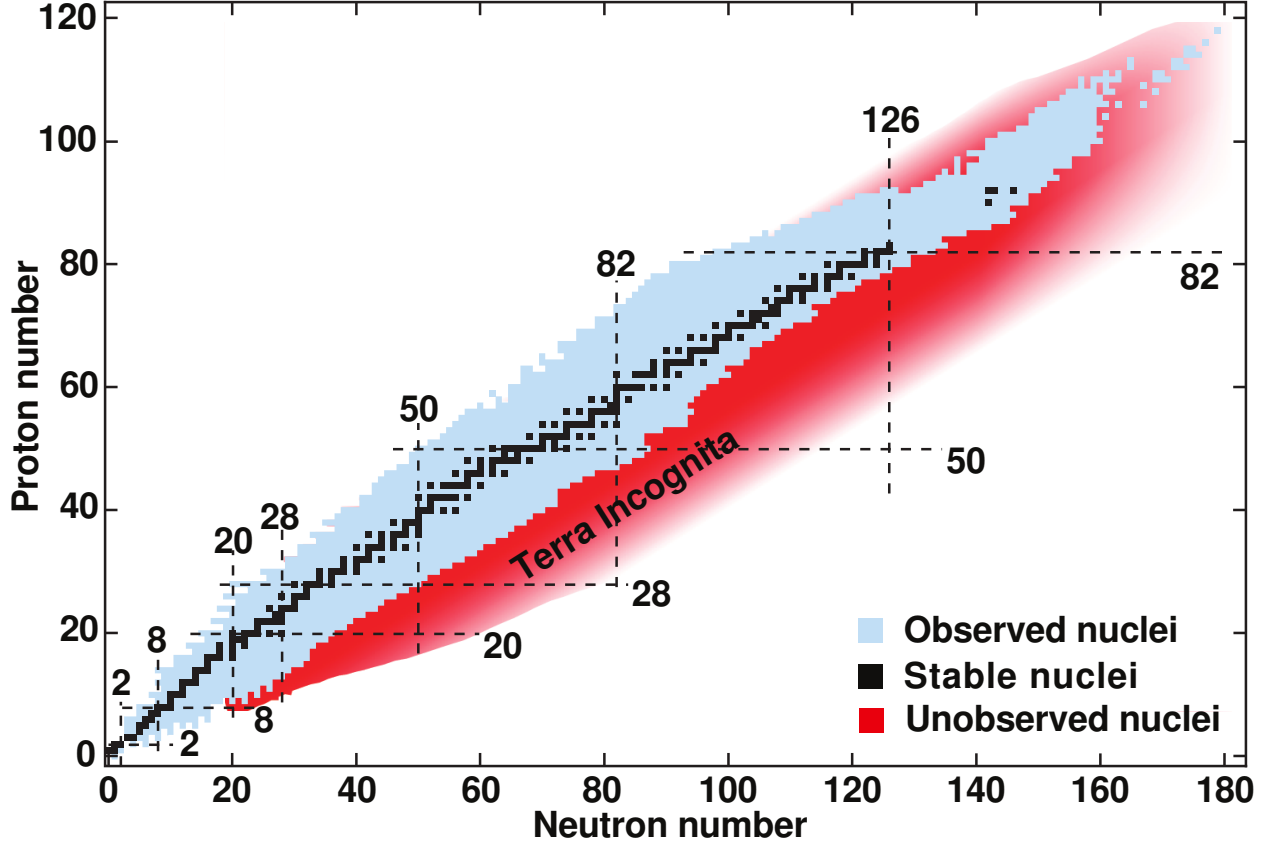
Figure 2.1 Visualization of the nuclear landscape, plot of the chart of nuclei. The number of protons (Z) is plotted versus the number of neutrons (N). Stable nuclei are shown as black boxes, observed unstable nuclei as blue boxes, and unstable nuclei predicted to exist, but not yet observed in red. *Magic numbers* (discussed in the text) are indicated by dashed lines. Figure is taken and modified from [3].

$$BE(N, Z) = \left(Zm_p + Nm_n - m(N, Z) \right) c^2. \tag{2.2}$$

In Equation 2.2, $m_p = 938.272046(21)\frac{MeV}{c^2}$ is the proton mass, $m_n = 939.565379(21)\frac{MeV}{c^2}$ is the neutron mass [33], $m(N, Z)$ is the mass of the nucleus with N neutrons and Z protons and $c = 299,792,458\frac{m}{s}$ is the speed of light [34]. The one-proton and -neutron *separation energies*, $S_p(N, Z)$ and $S_n(N, Z)$, are the energies needed to remove one proton or neutron from the nuclei respectively. They are defined as the difference between the *binding energies* of the neighboring nuclei:

$$S_{\mathrm{n}}(N, Z) = BE(N, Z) - BE(N - 1, Z), \qquad (2.3)$$

$$S_{\mathrm{p}}(N, Z) = BE(N, Z) - BE(N, Z - 1). \qquad (2.4)$$

The difference in one-nucleon separation energies, $\Delta S_p(N, Z)$ and $\Delta S_n(N, Z)$ are:

$$\Delta S_{\mathrm{n}}(N, Z) = S_{\mathrm{n}}(N, Z) - S_{\mathrm{n}}(N + 1, Z), \qquad (2.5)$$

$$\Delta S_{\mathrm{p}}(N, Z) = S_{\mathrm{p}}(N, Z) - S_{\mathrm{p}}(N, Z + 1). \qquad (2.6)$$

Plotting $S_n(N, Z)$ and $\Delta S_n(N, Z)$ for nuclei with an even number of neutrons and protons as a function of neutron number shows evidence of an internal structure. In Fig. 2.2 the two observables are plotted for even-even nuclei with $N > Z$ near stability. In the top panel where $S_n(N, Z)$ is plotted, the lines connect isotopic chains (same number of protons). At the neutron numbers 20, 28, 50, 82 and 126 there is a sudden drop in the separation energy for the next neutron, indicating that those numbers are special. The effect is even more pronounced in the bottom part of the figure where $\Delta S_n(N, Z)$ is plotted. In this representation there are clear peaks at the so-called *magic numbers*, again the solid lines connect isotopic chains.

The features that can be observed come from the fact that for nuclei with a *magic number* of neutrons an enhanced amount of energy is necessary to remove a neutron, which suggests that those nuclei are more tightly bound than their neighbors. This points to an internal structure of energy levels occupied by neutrons which have gaps at levels filled with a *magic*
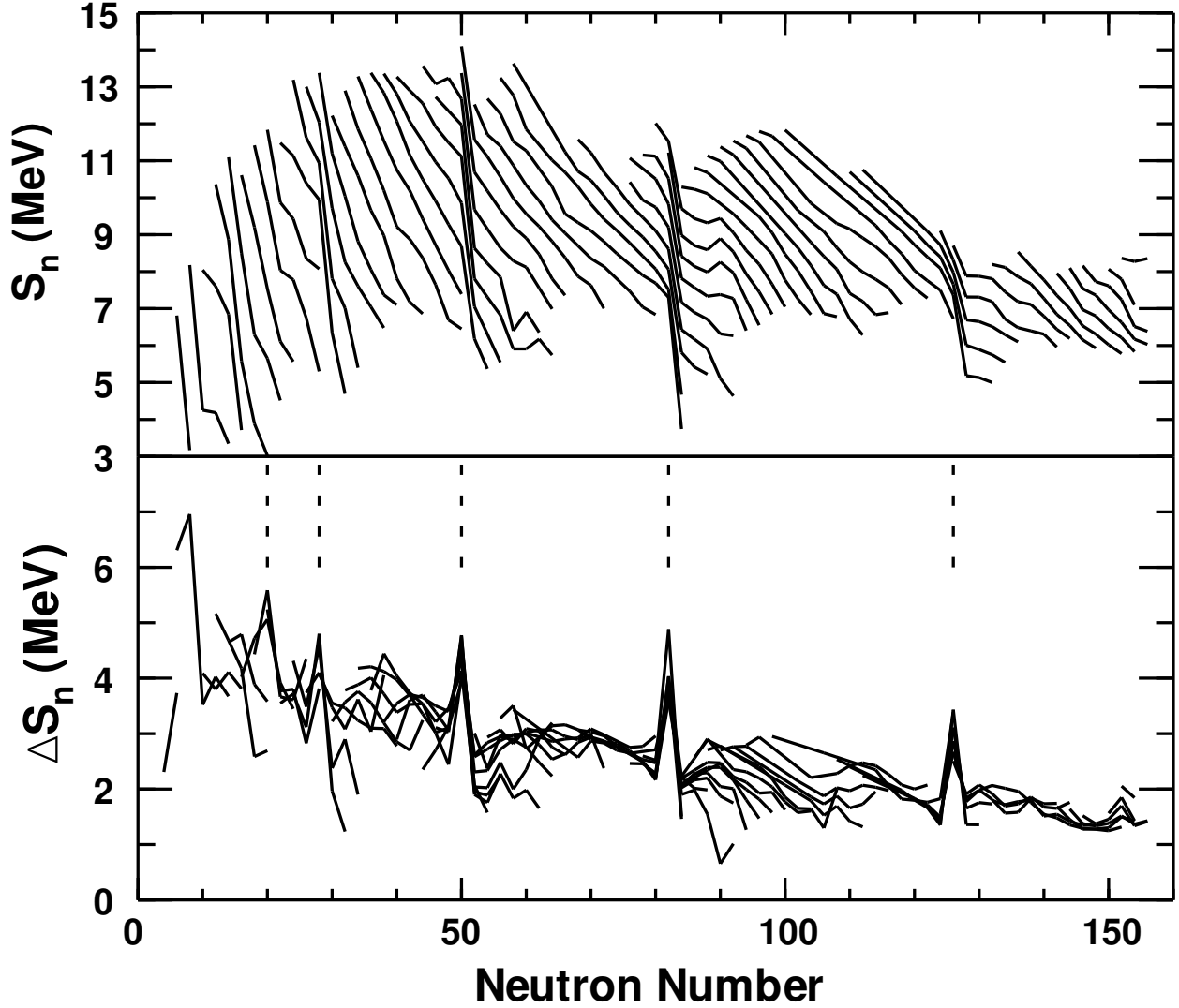
Figure 2.2 Top panel: one-neutron separation energies for even-even nuclei with $N > Z$ as a function of neutrons. Bottom panel: difference between one-neutron separation energies for the same set of nuclei. Solid lines connect isotopic chains (same Z). The dashed lines indicate the *magic numbers*, 20, 28, 50, 82 and 126. Figure is taken and modified from [4].

number of neutrons and the effects of those internal structures can be observed. The same effects can be seen for plots of $S_p(N, Z)$ and $\Delta S_p(N, Z)$ and result in the same *magic numbers*, just for protons. Nuclei that have a *magic number* of either neutrons or protons are called *semi-magic* or *magic nuclei*. Nuclei that have a *magic number* of both protons and neutrons are called *doubly magic*. As shown, *magic* and *doubly magic* nuclei are more strongly bound than their neighbors.

2.2 Nuclear Shell Model

The nuclear quantum system can be described by quantized energy levels that are available to the nucleons, also called orbitals or shells. Gaps in the energy levels give rise to the nuclear shell structure. These energy levels are characterized by a set of quantum numbers. As for all fermions, the *Pauli principle* applies to nucleons, prohibiting two nucleons to occupy a state with exactly the same set of quantum numbers. Protons are distinguishable from neutrons and the *Pauli principle* only applies to indistinguishable fermions. Therefore, they are considered separately and each can occupy their own energy levels. Both quantum systems are very much alike with very similar energy levels and gaps between the same levels. Nucleons have an intrinsic spin angular momentum quantum number $s = \pm\frac{1}{2}$ for the intrinsic spin $\vec{s}$, an orbital angular momentum quantum number $\ell = 0, 1, 2, 3, \ldots$ for the angular momentum $\vec{\ell}$ and these two couple to the total angular momentum $\vec{j} = \vec{l} + \vec{s}$ with total angular quantum number $j = \ell \pm \frac{1}{2}$. For each j exist $2j + 1$ magnetic sub-states, with the magnetic quantum number m which is the z-projection of $\vec{j}$, running from $-j$ to j in integer steps.

Energy levels are labeled by several quantum numbers, namely $n\ell_j$. The quantum number $n = 0, 1, 2, 3, \ldots$ is the principal quantum number, also called radial quantum number. It counts the times the wavefunction of this state changes its sign and is directly related to the harmonic oscillator model because the major quantum number of the harmonic oscillator model is $N = 2n + l$ (see Eq. 2.12 and 2.13). The states with $\ell = 0, 1, 2, 3, \ldots$ are usually labeled as $\ell = s, p, d, f, \ldots$ which is called the spectroscopic notation. Because every orbital j has $2j + 1$ magnetic sub-states it can be occupied by $2j + 1$ nucleons without two nucleons having exactly the same set of quantum numbers $n\ell jm$. Another characteristic of a state is

the *parity* π which describes the sign of a wavefunction when the following transformation is done:

$$x \rightarrow -x$$
$$y \rightarrow -y \qquad (2.7)$$
$$z \rightarrow -z.$$

Parity can be $\pi = \pm 1$ and is determined by $\pi = (-1)^{\ell}$.

The total angular momentum of a nucleus is labeled $\vec{J}$ and is the sum of the $\vec{j}$'s of the nucleons:

$$\vec{J} = \sum_{i=1}^{A} \vec{j} \qquad (2.8)$$

The discovery of the *magic numbers* led to the development of a theoretical nuclear model to help understand and predict observable features in nuclei [35, 36]. This model is called *Single Particle Nuclear Shell Model*. It treats the interaction of nucleons in a nucleus as the motion of a single nucleon in a mean field potential generated by all the other nucleons in the nucleus. In this model, the energies of the orbitals that can be occupied by the nucleons are called *single-particle energies*.

The nucleons occupy orbitals/shells with certain energies and there are energy gaps between certain orbitals. The nucleons that fill up all orbitals below a shell gap make up the so-called *inert core* and the remaining nucleons which are not enough to fill up all orbitals between this and and the next shell gap are called *valence nucleons*. If an orbital is filled with the

maximum number of nucleons allowed by the *Pauli principle* it is called a closed shell. Usually it is assumed that the *inert core* and the closed shells do not contribute to the total angular momentum of the nucleus and only unpaired *valence nucleons* contribute to the total angular momentum $\vec{J}$ of the ground state of the nucleus. This is especially true if there is only one more or less nucleon than the *inert core* [32]. Of course, for more realistic *shell models*, multiple nucleons outside the core have to be considered as well as mixing between different nucleon configurations [37]. For nuclei with fewer than 12 nucleons in total it is possible to include all nucleons in calculations and no cores are needed [38] (this is called the no-core shell model).

The basis for the *shell model* is the solution of the Schrödinger equation. In general the Hamiltonian of a system with A nucleons can be written like this [39]:

$$H = \sum_{i=1}^{A} \frac{\mathrm{p}_i^2}{2m_i} + \sum_{i>k=1}^{A} V_{ik}(\mathrm{r}_i - \mathrm{r}_k) \equiv T + V, \tag{2.9}$$

it describes the interaction between the different nucleons. The potential V_{ik} is the potential for the two-body interaction of two nucleons (3-body and higher-body forces are neglected here), p_i and m_i are the momentum and mass, respectively, for each nucleon. The Coulomb potential is so weak on the length scales of a nucleus that it may be neglected here. The exact form of the Hamiltonian and of the involved potentials is not known. Therefore, assumptions must be made. The first assumption, which simplifies the problem greatly, is that in first order one nucleon moves in a central potential generated by the remaining $A - 1$ nucleons. This is called the *mean-field* approximation. In this theory the nucleus is now a system of A *non-interacting* fermions (quasi particles) in an *external* potential. One can arrive at this

form of the problem by adding and subtracting a summed single-particle potential energy $\sum_{i=1}^{A} U_i(\mathrm{r})$, which is so far unspecified, to the Hamiltonian in 2.9:

$$H = \left\{ \sum_{i=1}^{A} \left[\frac{\mathrm{p}_i^2}{2m_i} + U_i(\mathrm{r}) \right] \right\} + \left\{ \sum_{i>k=1}^{A} V_{ik}(\mathrm{r}_i - \mathrm{r}_k) - \sum_{i=1}^{A} U_i(\mathrm{r}) \right\} \tag{2.10}$$

$$\equiv T_{MF} + V_{MF} + V_{RES} \equiv H_{MF} + V_{RES}.$$

H_{MF} is the *mean-field* Hamiltonian and V_{RES} is the residual interaction which is much weaker than the original interaction V [39]. The *mean-field* Hamiltonian describes the motion of a single particle in the *external mean-field* potential, V_{MF}, created by the $A-1$ remaining nucleons. V_{RES} is a small perturbative potential describing the residual interactions. It is easy to find a solution to the Schrödinger equation with just H_{MF} because the problem is now reduced to a one-particle problem. The contribution to the wavefunctions due to V_{RES} are dealt with in a perturbative way, see [39] for details.

The solutions for H_{MF} depend on the choice of the *mean-field* potential, $V_{MF} = U(r)$. A very common initial choice is the potential of a harmonic oscillator:

$$U(r) = \frac{1}{2} \mu \omega^2 r^2, \tag{2.11}$$

with μ being the reduced mass of the system and ω the oscillator frequency. The energy levels of this system depend on the major quantum number N:

$$E_N = \left(N + \frac{3}{2} \right) \hbar \omega. \tag{2.12}$$

N depends on the radial quantum number n and orbital quantum number l:

$$N = 2n + l. \tag{2.13}$$

With this simple potential it is possible to reproduce the first three *magic numbers*, N or $Z = 2$, 8 and 20 for shell closures but it cannot reproduce the higher numbers. In part (a) of Fig. 2.3 are the energy levels shown for ^{208}Pb calculated with a harmonic oscillator potential.

A more realistic choice for the potential is the Woods-Saxon potential:

$$U(r) = \frac{-V_0}{1 + e^{\frac{r-R}{a}}}, \tag{2.14}$$

with V_0 being the depth of the potential, R and a being the diffuseness and radius parameter [39]. For details on the values of the parameters see [4]. This potential breaks the degeneracy of the harmonic oscillator potential but still does not reproduce all *magic numbers*. In part (b) of Fig. 2.3 are the energy levels shown for ^{208}Pb calculated with a Woods-Saxon potential. In 1949 it was shown by Maria Goeppert-Mayer [36] and Otto Haxel, Hans Jensen and Hans Suess [35] that all *magic numbers* observed can be reproduced by adding a strong, attractive spin-orbit coupling term to the potential:

$$U_{so}(r, \vec{\ell}, \vec{s}) = U_{so}(r)\vec{\ell} \cdot \vec{s}. \tag{2.15}$$

In part (c) of Fig. 2.3 are the energy levels shown for ^{208}Pb calculated with a Woods-Saxon potential plus the spin-orbit coupling term. All the *magic numbers*, 2, 8, 20, 28, 50, 82 and 128 are reproduced.

The levels that have their origin in the same harmonic oscillator quantum number N are

usually named together. For $N = 0$ it is the $0s$ orbital, for $N = 1$ they are the $0p$ orbitals, for $N = 2$ they are the $1s0d$ (sd) orbitals, for $N = 3$ they are the $1p0f$ (pf) orbitals and for $N = 4$ they are the $0g1d2s$ (gds) orbitals.

Harmonic oscillator: N=0 (2), N=1 (8), N=2 (20), N=3 (40), N=4 (70)

Woods-Saxon: 0s (2), 0p (8), 0d 1s (20), 0f 1p (40), 0g (58), 2s 1d (92), 0h (92)

Woods-Saxon + Spin-orbit:

Orbital	[max]	total
$0h_{11/2}$	[12]	82
$2s_{1/2}$	[2]	70
$1d_{3/2}$	[4]	68
$1d_{5/2}$	[6]	64
$0g_{7/2}$	[8]	58
$0g_{9/2}$	[10]	50
$1p_{1/2}$	[2]	40
$1p_{3/2}$	[4]	38
$0f_{5/2}$	[6]	34
$0f_{7/2}$	[8]	28
$1s_{1/2}$	[2]	20
$0d_{3/2}$	[4]	18
$0d_{5/2}$	[6]	14
$0p_{1/2}$	[2]	8
$0p_{3/2}$	[4]	6
$0s_{1/2}$	[2]	2

Magic numbers (c): 82, 50, 28, 20, 8, 2
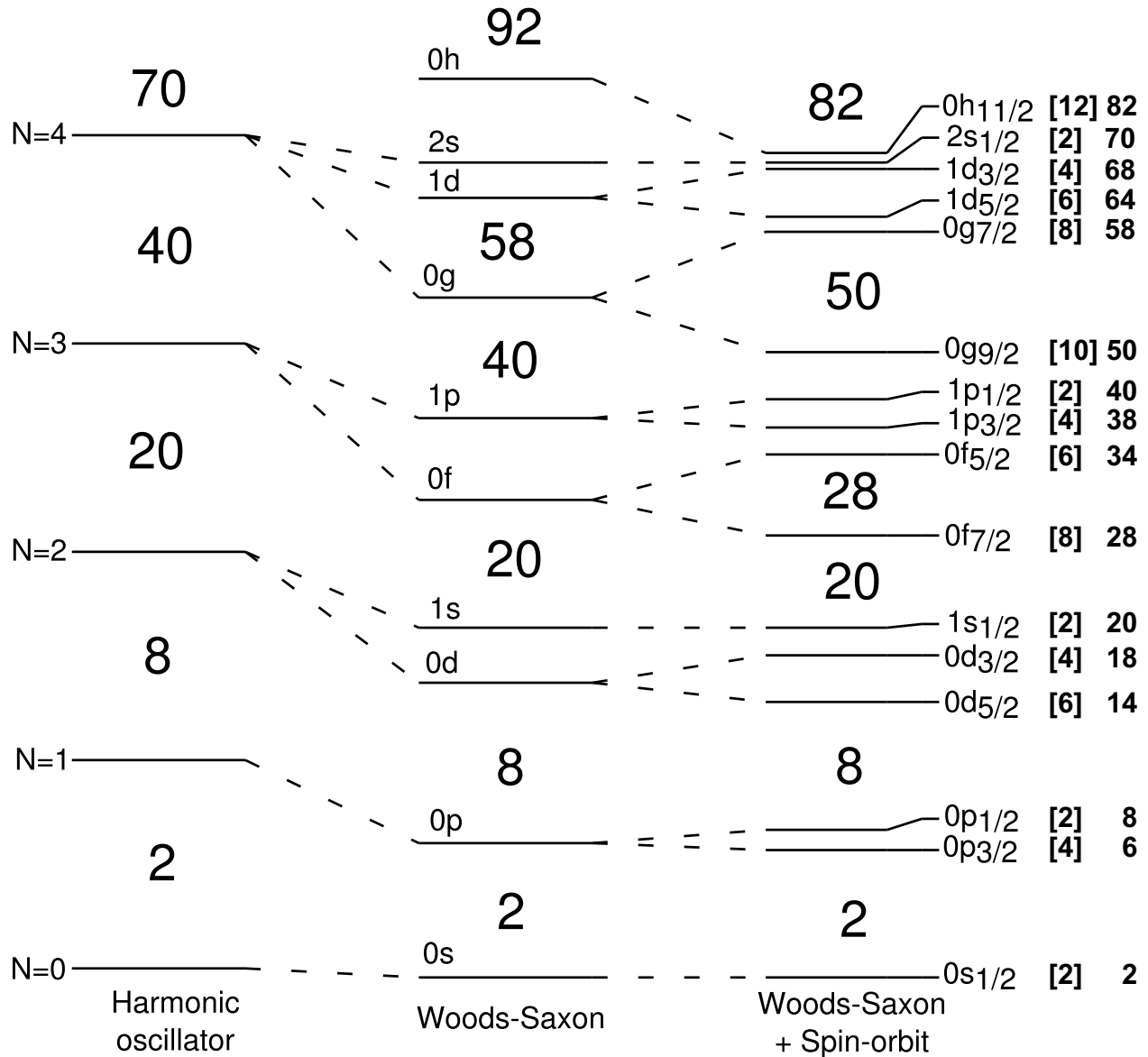
Figure 2.3 Calculated neutron single-particle energy levels for ^{208}Pb with a 3D harmonic oscillator potential (a), a Woods-Saxon potential (b) and a Woods-Saxon potential plus a spin-orbit coupling term (c). Gaps in between energy levels are marked with big numbers and they represent the *magic numbers* for each potential. The levels in (c) are also marked with their quantum numbers $n\ell_j$ and are followed by two additional numbers. The first one (in square brackets) shows the maximum allowed number of nucleons for this level and the second one counts the total number of nucleons that can be fit in all the shells up to this one. Figure is taken and modified from [4].

2.3 Shell Model Calculations and Effective Charges

For systems with more than 12 nucleons ($A > 12$), the Schrödinger equation gets so complex that it is too computationally intensive to solve it for every particle in the system. More precisely, the Hamiltonian matrix gets too big to be diagonalized in a reasonable time. For $A < 12$ it is feasible to solve the Schrödinger equation for all nucleons using the full Hamiltonian including 2-body interactions. For larger systems it is possible to find the single-particle levels easily for the *mean-field* potential (V_{MF} from Eq. 2.10) as shown in Fig. 2.3. This creates roughly the right energy levels (assuming a more elaborate potential, like the Woods-Saxon potential plus spin-orbit term, is used) but to make them more realistic, one has to include the *residual interaction* which includes V_{RES} from Eq. 2.10 of the Hamiltonian and takes into account all the two-body interactions which are not included in the *mean-field* potential. V_{RES} is usually dealt with in a perturbative way, for more details see [39].

Because of computational limits the problem needs to be simplified. This is done by choosing an inert core of A_{core} nucleons that is mostly a nearby *doubly magic* nucleus (it has always only closed shells). The remaining $A - A_{core}$ nucleons are the so-called *valence nucleons*. To further constrain the problem, a *model space* is chosen. This *model space* limits the single-particle energy levels that can be occupied by the *valence nucleons*. This space is always chosen to be as big as possible without reaching computational limits. The model space available is usually divided into two parts. The so-called Fermi energy divides the active hole orbitals (orbital energy lower than the Fermi energy) from the active particle orbitals (orbital energy higher than the Fermi energy). The Fermi energy is usually chosen in a shell gap between a completely filled shell and a not completely filled one. For Tin, the standard choice is tho have the Fermi energy between the $0g_{9/2}$ and the $0g_{7/2}$ shells for protons and

neutrons (at the *magic number* 50). Excitations are labeled by the fact where the nucleon is excited from. If the nucleon is excited from below the Fermi energy, leaving a hole, it is a hole excitation. If the nucleon is excited from a level above the Fermi energy then it is called particle excitation. In general, the excitations are labeled by the number of particle and hole excitations (np-mh). For every created hole there must be a created particle, n specifies how many nucleons are excited from levels above the Fermi energy and m specifies how many nucleons are excited out of the orbitals below the Fermi energy into levels above.

A typical shell-model calculation determines the energy levels of a nucleus in the following way. All possible multi-particle configurations of nucleons in the model space are calculated. Next, the Hamiltonian matrix is built with those basis wavefunctions and its eigenfunctions and eigenvalues are found. The lowest energy found (smallest eigenvalue) corresponds to the ground state and the corresponding combination of wavefunctions belonging to that eigenfunction determines the configuration of that state. The next higher energy and its corresponding wavefunction combination describes the first exited state and so on. For more details see [4, 39].

By restricting the calculations to a model space, effects the core or states outside of the model space might have are not accounted for. To take these effects into account, for example for the $E2$ transition operator (see Sec. 2.5 for details), *effective charges*, e_p and e_n, are introduced for protons and neutrons, respectively. The $E2$ transition rate between nuclear states depends on the transition operator

$$\mathcal{M}_{E2} = \sum_i e r_i^2 Y^2 e_i, \tag{2.16}$$

where e is the electric charge unit, e_i is the *effective charge* of the ith nucleon, Y^2 are the spherical harmonics of rank 2, r the radius and i is summing over all nucleons. See Section 2.5 for details. The *effective charges* enter Eq. 2.16 for e_i in the sum. They take into account the interactions of *valence nucleons* with the core which are not included in the calculations [38]. These interactions can disturb the core and induce a quadrupole moment to the core. The coupling of the single-particle movement of the *valence nucleons* with the quadrupole vibrational modes of the core is taken into account with the *effective charges* [40]. The *effective charges* are defined as:

$$e_p = (1 + \delta e_p) \tag{2.17}$$

$$e_n = (\delta e_n), \tag{2.18}$$

with $\delta e_{p/n}$ being *polarization charges* for the proton and neutron. For free nucleons, the clear choice is $e_p = 1$ and $e_n = 0$ which reproduces the standard values for the electric charge for protons and neutrons. In shell-model calculations, the standard choice for the *polarization charges* for *valence nucleons* is $\delta e_p = 0.5$ and $\delta e_n = 0.5$. Depending on the model space and interaction, these values are phenomenologically adapted but typically assumed to be constant. It is not clear if this assumption is correct for the whole model space in every case [40–42].

The effect of the *polarization charges* can directly be seen in the shell-model calculations of

the reduced electric quadrupole transition probability (see Sec. 2.5):

$$B(E2; J_i \to J_f) = \frac{1}{2J_i + 1}(e_n A_n + e_p A_p)^2$$
$$= \frac{1}{2J_i + 1}|M_p|^2, \tag{2.19}$$

as well as the proton and neutron transition matrix elements:

$$M_p = e_n A_n + e_p A_p$$
$$M_n = e_p A_n + e_n A_p, \tag{2.20}$$

where A_n and A_p are the neutron and proton shell-model transition amplitudes, respectively.

2.4   Excitations and Collective Excitations

Nuclei with an even number of protons and neutrons (even-even nuclei) always have a ground state with spin-parity $J^\pi = 0^+$. Their first excited state is usually a $J^\pi = 2^+$ state. For magic nuclei the energy gap between this state and the ground state is large (for example 1.3 MeV for ^{46}Ca and 1.2 MeV for ^{130}Sn). It is even larger for doubly magic nuclei (for example 3.8 MeV for ^{48}Ca and 4.0 MeV for ^{132}Sn) and smaller for non magic nuclei as can be seen in Fig. 2.4.

The single-particle shell model explains nuclear properties by the behavior of individual nucleons. This can be very accurate near shell closures where only few nucleons contribute.
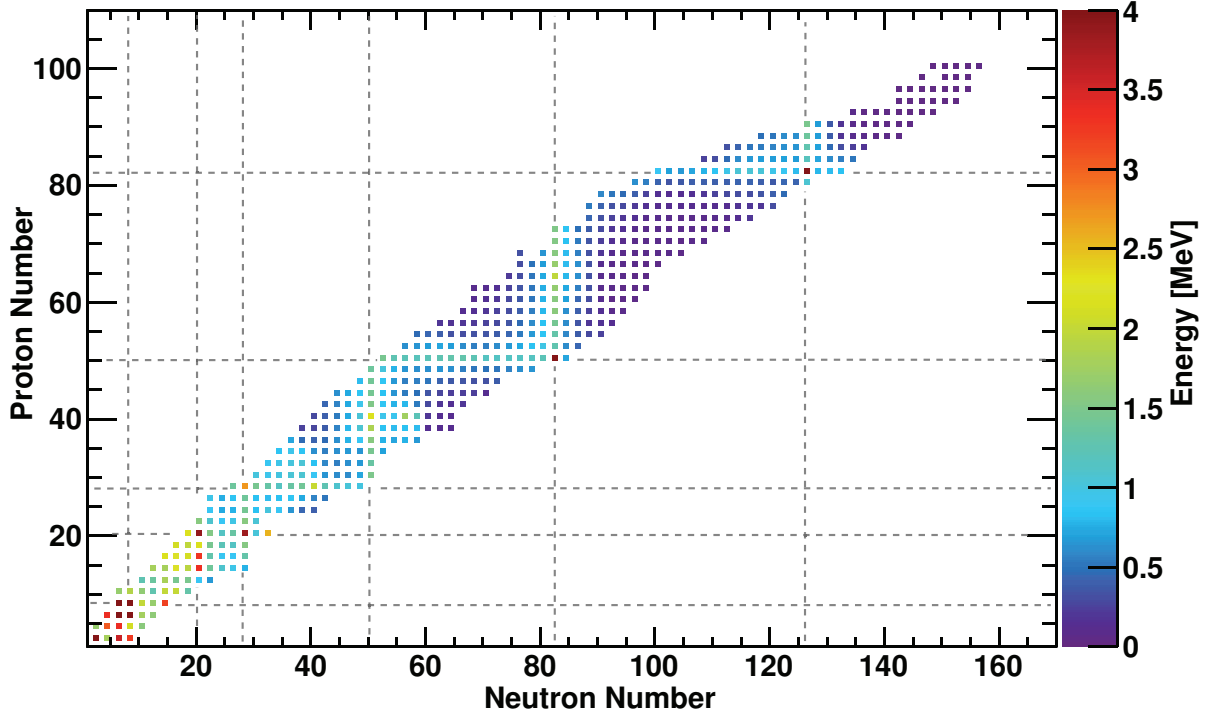
Figure 2.4 Energies of the first 2^+ states in even-even nuclei. Dashed lines mark the magic numbers. Figure is taken and modified from [5].

Away from closed shells, one can also observe collective behavior, many *valence nucleons* contribute together to the excited state energies. Geometrical models have been developed to describe the low-lying excitation energies due to the coherent motion of the *valence nucleons*. Two models will be looked at closer here. One is a *vibrational* model and another one a *rotational* model.

In the *vibrational* model, the nucleus is treated as an incompressible fluid which oscillates around an average spherical shape. The energy levels of an even-even *vibrational* nucleus are evenly spaced. They are ordered in the following way a ground state with spin-parity $J^\pi = 0^+$, then a first excited state with $J^\pi = 2^+$, ideally followed by an almost degenerate triplet with $J^\pi = 0^+$, 2^+, 4^+ and then an almost degenerate quintet with $J^\pi = 0^+$, 2^+, 3^+, 4^+, 6^+ [31]. The first excited $J^\pi = 2^+$ state comes from a single phonon. A phonon, in the quantum

theory of mechanical vibrations, is a quantum of vibrational energy which is produced by mechanical vibrations [31]. The triplet comes from the coupling of two phonons, resulting in $J = 0, 2, 4$ and an energy twice the size of the single phonon. The coupling of three phonons leads to the quintet with $J = 0, 2, 3, 4, 6$ and three times the energy of a single phonon. The energy of the nth excited state can be approximated by:

$$E_{vib}(n) = nE(2^+). \tag{2.21}$$

In the simplest *rotational* model, the nucleus is treated as a rigid, deformed rotor. The energy levels can be calculated like this [31]:

$$E_{rotor}(J) = \frac{\hbar^2}{2I}J(J+1), \tag{2.22}$$

with I being the moment of inertia of the nucleus. The deformed nucleus rotates around a axis perpendicular to the symmetry axis of the deformation. The most common form of deformation is the quadrupole deformation. It can be described by the radius, $R(\theta, \phi)$, of the nucleus which is characterized by the *quadrupole deformation parameter β*:

$$R(\theta, \phi) = R_0(1 + \beta Y_{2,0}(\theta, \phi)), \tag{2.23}$$

with R_0 from Eq. 2.1 and $Y_{2,0}(\theta, \phi)$ the spherical harmonic. The value of β determines the shape of the nucleus. A $\beta > 0$ gives a *prolate* (elongated) shape, and a $\beta < 0$ describes an *oblate* (flattened) shape.

Experimental evidence that may indicate that an even-even nucleus is collective, meaning

many nucleons participate in the excitation, is a large $B(E2; 0_{\text{gs}}^+ \rightarrow 2_1^+)$ excitation probability.

2.5   Reduced Quadrupole Transition Strength

A nucleus that is in a bound excited state, $|i\rangle$ (initial state), will most of the time decay via γ-ray emission to a lower lying state, $|f\rangle$ (final state). The γ-ray energy of this *electromagnetic transition* is equal to the energy difference of the initial and final state:

$$E_\gamma = E_i - E_f. \tag{2.24}$$

The energy that is lost due to the recoil of the nucleus can be neglected. The transitions can be ranked by the parity, π, and the angular momentum, J, carried away by the photon. The carried-away angular momentum and parity of the photon depends on the spin-parity values of the initial, J_i^π, and final, J_f^π, state of the transition. A schematic of the transition is shown in Fig. 2.5.
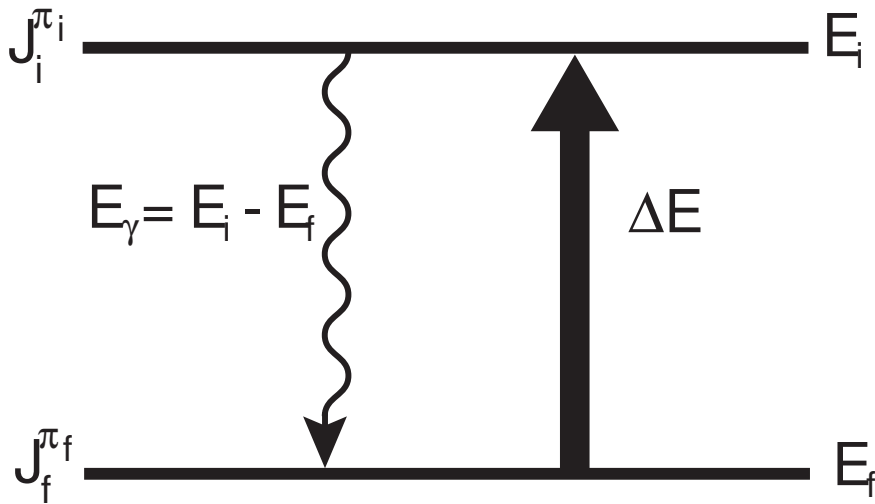
Figure 2.5 Schematic of the excitation of a nucleus (solid arrow) and the de-excitation via γ-ray emission (squiggly arrow). Figure is taken and modified from [5].

Because the photon is a spin-1 boson, it must carry away at least a total angular momentum unit of 1 and can never be 0. The rules that determine the nature of this *electromagnetic transition* are the following.

The carried-away angular momentum determines the *multipolarity*, λ, of the transition. As mentioned, $\lambda = 0$ is not allowed because the photon must at least have an angular momentum of 1. Transitions with $\lambda = 1$ are called dipole-, with $\lambda = 2$ quadrupole-, with $\lambda = 3$ octupole-transitions and so on (the order is equal to 2^λ). Because *electromagnetic transitions* conserve angular momentum, the following restriction applies:

$$|J_i - J_f| \leq \lambda \leq J_i + J_f, \tag{2.25}$$

$$\lambda \neq 0.$$

Furthermore parity has to be conserved and hence this equation:

$$\pi_i \pi_{photon} (-1)^\lambda = \pi_f, \tag{2.26}$$

has to be fulfilled. Transitions can either be electric (E), $\pi_{photon} = +1$, or magnetic (M), $\pi_{photon} = -1$. The rules that decide this are:

$$\pi_i \pi_f (-1)^\lambda = \begin{cases} +1 & \text{electric} \\ -1 & \text{magnetic.} \end{cases} \tag{2.27}$$

Transitions are labeled as either electric transitions with multipolarity λ, $E\lambda$ or magnetic transitions with multipolarity λ, $M\lambda$. A transition can have several possible *electromagnetic*

decays. All forms of *electromagnetic* radiation are allowed that fulfill Eq. 2.25 and from Eq. 2.27 it is clear that it has to be either a combination of

$$M1, E2, M3, E4, \ldots \quad \text{for } \pi_i \pi_f = (+1), \tag{2.28}$$

or

$$E1, M2, E3, M4, \ldots \quad \text{for } \pi_i \pi_f = (-1). \tag{2.29}$$

The transition probability, T, for one transition depending on π, λ and its projection μ, is calculated by the 'golden rule' of time-dependent perturbation theory and is [39]:

$$T_{fi}^{\pi\lambda\mu} = \frac{2}{\epsilon_0 \hbar} \frac{\lambda + 1}{\lambda[(2\lambda + 1)!!]^2} \left(\frac{E_\gamma}{\hbar c}\right)^{2\lambda+1} |\langle J_f M_f | \mathcal{M}_{\pi\lambda\mu} | J_i M_i \rangle|^2. \tag{2.30}$$

In this equation, $\mathcal{M}_{\pi\lambda\mu}$ is the nuclear *electromagnetic* transition operator associated with the $\pi\lambda\mu$ transition, E_γ is the energy of the transition, ϵ_0 is the vacuum permittivity and $\hbar$ is the reduced Planck constant. The magnetic sub-states are usually not observed individually, therefore Eq. 2.30 is averaged over the initial sub-states (M_i) and summed over the final sub-states (M_f) and projections μ [39]. This results in:

$$T_{fi}^{\pi\lambda} = \frac{1}{2J_i + 1} \sum_{M_i} \sum_{M_f, \mu} T_{fi}^{\pi\lambda\mu} \tag{2.31}$$

$$= \frac{2}{\epsilon_0 \hbar} \frac{\lambda + 1}{\lambda[(2\lambda + 1)!!]^2} \left(\frac{E_\gamma}{\hbar c}\right)^{2\lambda+1} B(\pi\lambda; J_i \to J_f). \tag{2.32}$$

The *reduced transition probability* $B(\pi\lambda; J_i \to J_f)$ is defined as:

$$B(\pi\lambda; J_i \to J_f) \equiv \frac{1}{2J_i+1} |\langle J_f||\mathcal{M}_{\pi\lambda}||J_i\rangle|^2. \tag{2.33}$$

The double bar notation indicates a *reduced matrix element* in the sense of the *Wigner-Eckart theorem* [39]. A normal matrix element of an operator $\mathcal{T}_{\lambda\mu}$ can be rewritten with the help of Clebsch-Gordan coefficients into a product of a geometric factor containing the projection quantum numbers M_f, λ and M_i, and a *reduced matrix element* which does not contain them [39]:

$$\langle J_f M_f|\mathcal{T}_{\lambda\mu}|J_i M_i\rangle = (-1)^{J_f-M_f} \begin{pmatrix} J_f & \lambda & J_i \\ -M_f & \mu & M_i \end{pmatrix} \langle J_f||\mathcal{T}_\lambda||J_i\rangle. \tag{2.34}$$

The relation

$$\sum_{M_f,\mu,M_i} (-1)^{J_f-M_f} \begin{pmatrix} J_f & \lambda & J_i \\ -M_f & \mu & M_i \end{pmatrix} = 1 \tag{2.35}$$

is the reason why in Eq. 2.32 the sum drops out.

The total rate of a transition from J_i to J_f is calculated by summing over all possible transitions, meaning to sum over the allowed combinations of π and λ,

$$\sum_{\pi,\lambda} T_{fi}^{\pi\lambda} = \sum_{\lambda} \left(T_{fi}(E) + T_{fi}(M) \right). \tag{2.36}$$

For more details see [39].

The $B(\pi\lambda)$ value depends on the direction of the transition. Assuming that a state b is higher in energy than a state a, the notation $B(\pi\lambda;\uparrow) \equiv B(\pi\lambda; a \to b)$ is defined for an excitation and $B(\pi\lambda;\downarrow) \equiv B(\pi\lambda; b \to a)$ for a decay. The relation between those two is [4]:

$$B(\pi\lambda; b \to a) = \frac{2J_a + 1}{2J_b + 1} B(\pi\lambda; a \to b). \tag{2.37}$$

The operators $\mathcal{M}_{\pi\lambda}$ are defined as follows. For electric transitions it is:

$$\mathcal{M}_{E\lambda} = \sum_{j=1}^{A} r_j^{\lambda} Y_{\lambda\mu}(\theta, \phi) e_j e, \tag{2.38}$$

with the sum running over all nucleons in the nucleus. e is the electric charge unit and e_j the *effective charge* of the jth nucleon and $Y_{\lambda\mu}$ is the spherical harmonic.

For magnetic transitions it is:

$$\mathcal{M}_{M\lambda} = \frac{\mu_N}{\hbar c} \sum_{j}^{A} \left[\frac{2}{\lambda+1} g_j^{\ell} \vec{\ell}_j + g_j^{s} \vec{s}_j \right] \nabla_j [r_j^{\lambda} Y_{\lambda\mu}(\theta\phi)], \tag{2.39}$$

with g_j^s and g_j^{ℓ} being the spin and orbital angular momentum g-factors, $\vec{s}$ and $\vec{\ell}$ are the spin and orbital angular momentum vectors, respectively. The values of the g-factors are $g_p^s = 5.586$, $g_n^s = -3.826$, $g_p^{\ell} = 1$, $g_n^{\ell} = 0$ for free protons and neutrons, and

$$\mu_N = \frac{e\hbar}{2m_p c} = 0.105 \ e\text{fm} , \tag{2.40}$$

is the nuclear magneton.

From the factors in Eq. 2.32 (with $E_\gamma \approx 1$ MeV) it is clear that the transition rates for electric or magnetic transitions with multipolarity λ are about seven orders of magnitude bigger than the rates for electric or magnetic transitions with multipolarity $\lambda + 2$ (also see Sec. 3.1). Therefore, in most cases, only the lowest multipole transition is important for a given type (electric or magnetic) of transition. If both electric and magnetic transitions are allowed, then the $\lambda + 1$ transitions competes with the λ transition. This is not the case for

this experiment but for experiments where it is, it is important to define the multipole mixing ratio. For the most common case, a mixing of $E2$ and $M1$, the mixing ratio $\delta(E2/M1)$, is:

$$\delta\left(\frac{E2}{M1}\right) = \sqrt{\frac{T(E2)}{T(M1)}}, \tag{2.41}$$

with the transition rate T being the inverse partial lifetime, $T = \frac{1}{\tau_p}$ (see Sec. 3.1 for details). With equation 3.4 for the $E2$ transition and Eq. 3.6 for the $M1$ transition, the mixing ratio is:

$$\delta\left(\frac{E2}{M1}\right) = E_\gamma\sqrt{\frac{B(E2)}{B(M1)}}8.29 \times 10^{-3}\frac{\mu_N}{e\text{fm}^2\text{MeV}}. \tag{2.42}$$

To judge if transitions with different multipolarities are relatively weak or strong, the reduced transition probabilities are expressed in the so-called *single-particle units* which are also called *Weisskopf units*. This *Weisskopf unit* is an estimate of the $B(\pi\lambda)$ value for a single-particle (proton or neutron) and how it depends upon mass [4]. By convention it is defined by:

$$B_W(E\lambda) = \left(\frac{1}{4\pi}\right)\left[\frac{3}{3+\lambda}\right](1.2A^{\frac{1}{3}})^{2\lambda}e^2fm^{2\lambda}, \tag{2.43}$$

and

$$B_W(M\lambda) = \left(\frac{10}{\pi}\right)\left[\frac{3}{3+\lambda}\right](1.2A^{\frac{1}{3}})^{2\lambda-2}\mu_N^2fm^{2\lambda-2}. \tag{2.44}$$

The most common ones are:

$$B_W(E1) = 0.0645A^{\frac{2}{3}}e^2fm^2, \tag{2.45}$$

$$B_W(E2) = 0.0594 A^{\frac{4}{3}} e^2 fm^4, \qquad (2.46)$$

and

$$B_W(M1) = 1.790 \mu_N^2. \qquad (2.47)$$

In general the unit in which $B(E2 \uparrow)$ values are given is $e^2 fm^4$. It can also be converted into $e^2 b^2$ by dividing the $e^2 fm^4$ value by a factor of 1000. 1 b is one barn and equal to $10^{-28} m^2$.

2.6 Physics of the Tin Isotopes: Leading to ^{104}Sn

There is a great theoretical and experimental interest in the study of nuclei far away from β-stability. The Tin isotopes offer a unique laboratory for spectroscopic studies of semi-magic isotopes ($Z = 50$) over a large range of neutron numbers. The Tin isotopes have a double shell closure for ^{100}Sn ($Z = 50$ and $N = 50$) and for ^{132}Sn ($Z = 50$ and $N = 82$).

The comparison of theoretical descriptions of nuclear excited states with spectroscopic data obtained for the Tin isotopes will help the current understanding of nuclear systems; consisting of *valence neutrons* beyond the *doubly magic* ^{100}Sn core or neutron holes relative to ^{132}Sn.

Two such properties of interest are the energy of the first excited 2^+ state of the even-even Tin isotopes and their reduced electric quadrupole transition strength from the ground state to the first excited state, $B(E2; 0^+ \rightarrow 2^+)$. The selection rules listed in Sec. 2.5 show that for a transition from a 2^+ level to a 0^+ ground state only $E2$ transitions are allowed.

The excitation energy E(2^+) and the $B(E2 \uparrow)$ strength for the light even-even Tin nuclei provide information regarding the onset of collectivity with the addition of *valence neutrons* to the doubly-magic ^{100}Sn core. The energies of the first excited 2^+ state for the majority of Sn isotopes between the $N = 50$ and $N = 82$ shell closures are well established and consistent with results from large-scale shell-model calculations. The energies of the first exited 2^+ state for even-even Tin isotopes with $N = 52 \rightarrow 82$ are shown in Fig. 2.6.
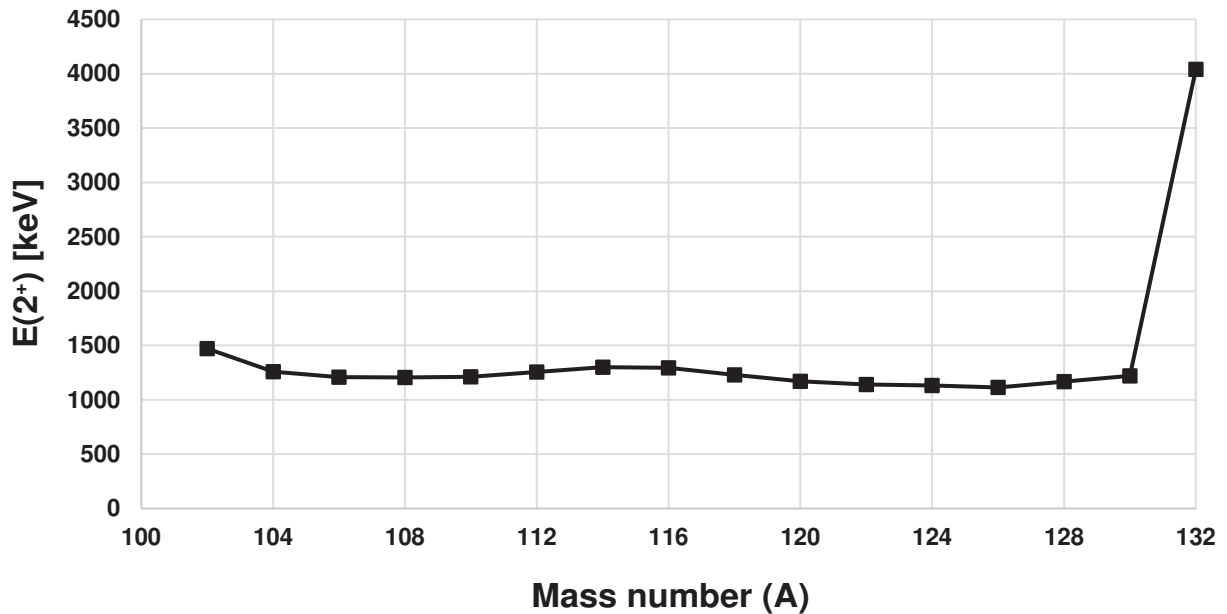
Figure 2.6 Measured energy of the first excited 2^+ state for the even-even Tin isotopes between the $N = 50$ and $N = 82$ shell closures. Data is taken from [6].

Prior to the current study, $B(E2 \uparrow)$ data for even-even Tin nuclei existed only up to ^{106}Sn. No data was available for the more neutron-deficient Tin nuclei. Measured $B(E2 \uparrow)$ values agree well with theoretical predictions of the shell model up to mid-shell (^{116}Sn). Below mid-shell, recent experiments have yielded $B(E2 \uparrow)$ values consistently higher than predicted by

theory. The enhanced $E2$ transition strengths in the neutron-deficient Sn isotopes below mid-shell are not reproduced by results from shell-model calculations. During the analysis of this experiment, two $B(E2\uparrow)$ values were published for ^{104}Sn [1, 7] which disagree with each other. In Fig. 2.7, an overview is shown of the known $B(E2\uparrow)$ values for even-even Tin isotopes. Currently, no theoretical framework exists that describes the evolution of both the energy of the first excited 2^+ state and $B(E2; 0^+ \rightarrow 2^+)$ well for the Tin isotopes between $N = 50$ and $N = 82$.
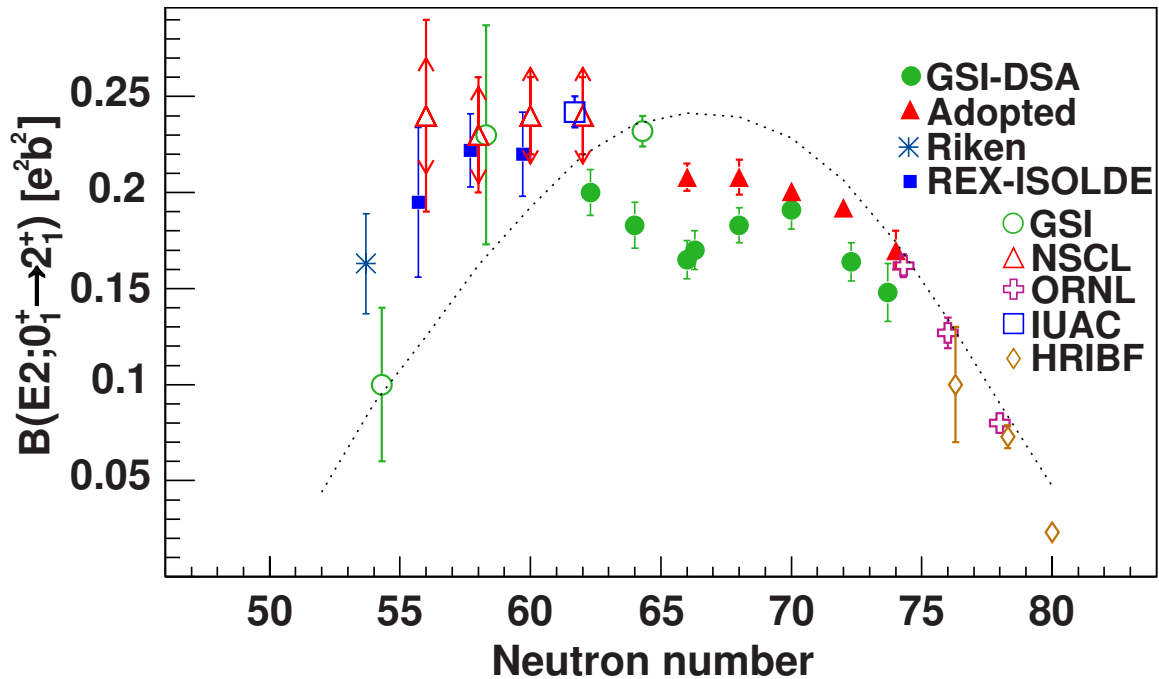
Figure 2.7 Measured $B(E2\uparrow)$ values for the chain of even-even Tin isotopes. Data are taken from: Adopted values are published by the National Nuclear Data Center [6], RIKEN [7], REX-ISOLDE [8, 9], GSI-DSA [10], GSI [1, 11, 12], NSCL [13], ORNL [14], IUAC [15], HRIBF [16]. The dotted line reproduces the theoretical calculation shown in [11] with gds ($t_\pi = 4$, see Sec. 6 for details).

The goal of the current study is to measure the intermediate-energy Coulomb excitation cross section for the population of the first excited 2^+ state of ^{104}Sn and extract the reduced transition strength $B(E2; 0^+ \rightarrow 2^+)$. Due to experimental restrictions (see Sec. 5.3.2.3), the measurement was done relative to the well-established $B(E2\uparrow)$ value of ^{102}Cd [2, 43].

^{102}Cd was more intensely present in the cocktail beam than ^{104}Sn (see Sec. 5.2 and 5.5). With that, another data point is added for the $B(E2 \uparrow)$ value of ^{104}Sn. This will help clarifying the disagreement between the current values [1] and [7]. The second goal is to find a theoretical explanation for the behavior of the $B(E2 \uparrow)$ values of the even-even Tin isotopes below mid-shell.

Chapter 3

Quadrupole Collectivity:

Experimental Methods

In this chapter, two common techniques to measure the strength of the electric quadrupole transition are described. Excited-state lifetimes are briefly discussed and the method of intermediate-energy Coulomb excitation is explained in more detail.

3.1 Excited-state Lifetimes

The lifetime τ_{if} of an excited state is directly related to the transition probability per unit time $T_{if}^{\pi\lambda}$ between an initial and final state ($|i\rangle$ and $|f\rangle$) via

$$\tau_{if} = \frac{1}{T_{if}}.$$

(3.1)

The transition probability on the other hand is related to the excitation strength value $B(\pi\lambda)$ as follows (see Eq. 2.32):

$$T_{i\rightarrow f}^{\pi\lambda} = \frac{2}{\epsilon_0\hbar}\frac{\lambda+1}{\lambda[(2\lambda+1)!!]^2}\left(\frac{E_\gamma}{\hbar c}\right)^{2\lambda+1}B(\pi\lambda; J_i \rightarrow J_f).$$

(3.2)

For the most common transitions, the partial mean lifetime τ_p and the transition probability $B(\pi\lambda \downarrow)$ are related by [4]:

$$B(E1) = \frac{0.629}{E_\gamma^3 \tau_p} e^2 fm^2 MeV^3 fs, \tag{3.3}$$

$$B(E2) = \frac{816}{E_\gamma^5 \tau_p} e^2 fm^4 MeV^5 ps, \tag{3.4}$$

$$B(E3) = \frac{1760}{E_\gamma^7 \tau_p} e^2 fm^6 MeV^7 \mu s, \tag{3.5}$$

for electric transitions and for magnetic transitions:

$$B(M1) = \frac{56.8}{E_\gamma^3 \tau_p} \mu_N^2 MeV^3 fs, \tag{3.6}$$

$$B(M2) = \frac{74.1}{E_\gamma^5 \tau_p} \mu_N^2 fm^2 MeV^5 ns, \tag{3.7}$$

$$B(M3) = \frac{0.1585}{E_\gamma^7 \tau_p} \mu_N^2 fm^4 MeV^7 s. \tag{3.8}$$

As shown, a lifetime measurement can be used to extract $B(E2 \uparrow)$ values.

3.2 Intermediate-Energy Coulomb Excitation

The technique used in this experiment is called intermediate-energy Coulomb excitation. In contrast to "safe" (energies below the Coulomb barrier) Coulomb excitation, the energy of the projectile is higher than the Coulomb barrier energy. Typically projectile energies over 50 MeV/u are used together with high-Z targets like gold. Targets with high-Z values are used

to generate strong Coulomb fields. The projectile and/or target get excited in the Coulomb field of one another, leading to excitations from an initial state $|i\rangle$ to a final state $|f\rangle$. Because this happens at energies higher than the Coulomb barrier, it can lead to situations where projectile and target get so close that it is possible for nuclear interactions to contribute to the excitation process. If this happens, the excitation process becomes complicated. For such processes, the measured excitation cross section would not be easily translated into the electric quadrupole transition strength. Only Coulomb interactions must contribute to the cross section for the least model-dependent analysis. *NSCL* (*National Superconducting Cyclotron Laboratory*) uses projectile fragmentation as an efficient production method for fast rare-isotope beams (see Sec. 4.2). At high energies, events with small scattering angles, corresponding to large impact parameters, have to be analyzed. Small impact parameters can lead to nuclear interactions. If nuclear contributions were allowed, it would make the extraction of the transition matrix element difficult and model dependent. Nuclear contributions are theoretically much more uncertain and these uncertainties would fold into the uncertainty of the transition strength.

In the present experiment, the process of interest is where the projectile nuclei ^{104}Sn and ^{102}Cd start in the 0^+ ground state (initial state), get excited to the first excited 2^+ state (final state) and de-excite again to the 0^+ ground state (final-final state which is the initial state). In all calculations the index i stands for the initial state from which the excitation process starts, f stands for the final state where the excitation leads to and ff stands for the final-final state, the state to where the final state (f) de-excites to. In this experiment, the initial (i) and final-final (ff) state are the same.

Fig. 3.1 gives an overview of the excitation and de-excitation process. The minimum allowed

impact parameter b_{min} is related to the maximum center-of-mass scattering angle θ_{max}^{cm} by [44]:

$$b_{min} = \frac{a_0}{\gamma} \cot\left(\frac{\theta_{max}^{cm}}{2}\right), \tag{3.9}$$

with $\gamma = 1/\sqrt{1-(v/c)^2}$ and a_0 is the half-distance of closest approach:

$$a_0 = \frac{Z_t Z_p e^2}{\mu v^2}. \tag{3.10}$$

$Z_{t(p)}$ is the atomic number of the target (projectile), e is the electric charge and μ the reduced mass of the system. To ensure that only events without nuclear contributions are considered, the analysis has to be restricted to impact parameters that are at least two Fermi larger than the sum of the nuclear radii of the target-projectile system ("touching-sphere system") [44]:

$$b_{\mathrm{min}} = r_0 \left(A_{\mathrm{t}}^{1/3} + A_{\mathrm{p}}^{1/3}\right) + 2 \text{ fm}, \tag{3.11}$$

where $r_0 = 1.25\,fm$.

From here on it is assumed that only the Coulomb interaction contributed to the excitation process. The following equations describe the Coulomb excitation of the projectile, to describe the excitation of the target all that needs to be done is to simply replace Z_p and Z_t in the following equations.

The excitation strength is calculated from the cross section of the Coulomb excitation process. The cross section for the intermediate-energy Coulomb de-excitation of the first exited 2^+ state to the 0^+ ground state of an even-even nucleus is deduced from the data like this:
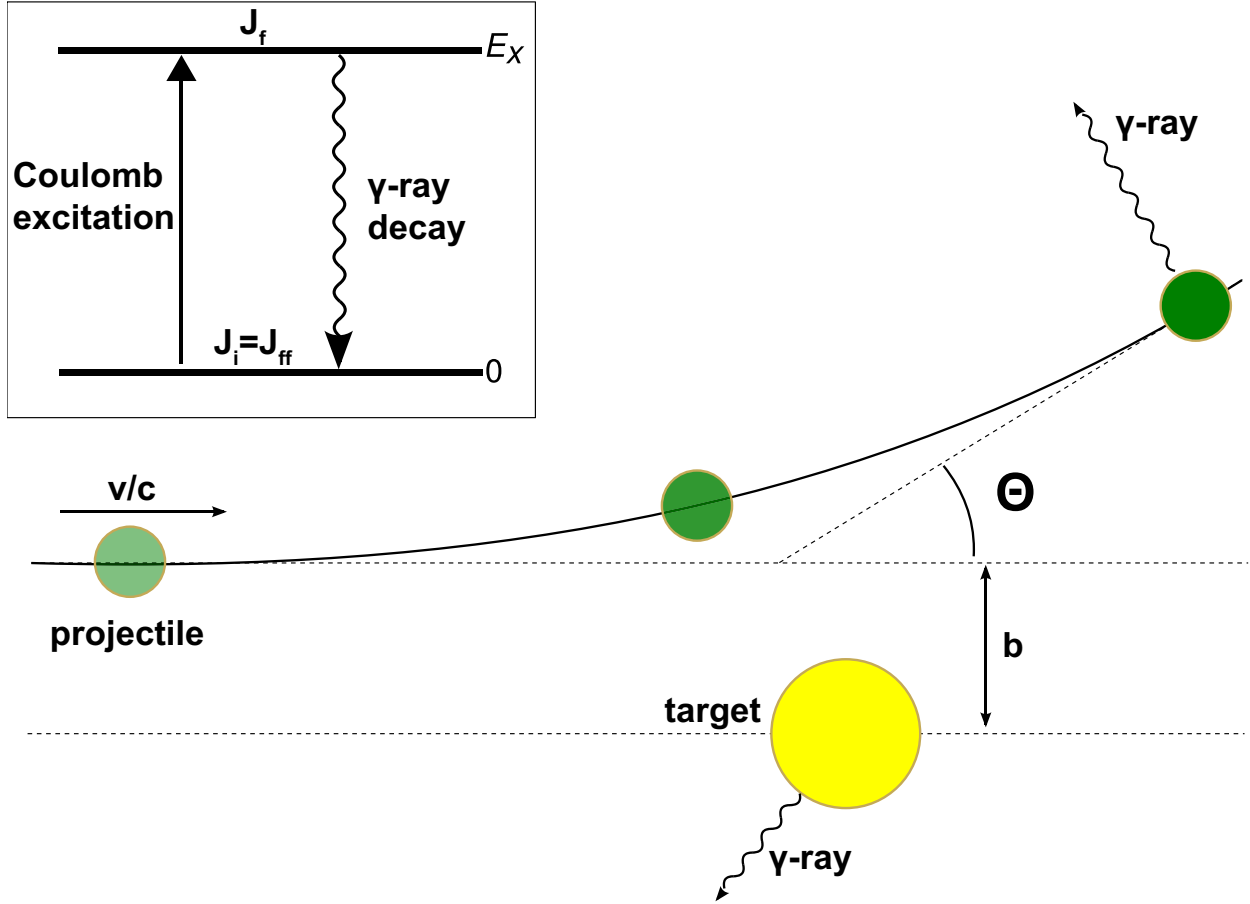
Figure 3.1 Schematic picture of the intermediate-energy Coulomb scattering process. Shown are the projectile and target nucleus as well as center-of-mass scattering angle θ and impact parameter b (see text for details). The insert shows the excitation and de-excitation process in a level scheme. The γ-ray energy is equal to the energy difference of the nuclear levels. Figure is taken and modified from [3].

$$\sigma_{2_1^+ \rightarrow 0_{g.s.}^+} = \frac{N_\gamma}{N_{Beam} N_{Target}}. \tag{3.12}$$

It is the number of γ rays emitted (N_γ) divided by the number of incident beam particles (N_{Beam}) and the area number density of target nuclei (N_{Target} in $\frac{\#}{cm^2}$).

Alder and Winther developed a semi-classical theory that connects the cross sections of intermediate-energy Coulomb excitation to the property of interest; the $B(E2\uparrow)$ value [45].

By assuming that the scattering process takes place along a classical trajectory, the total differential excitation cross section can be described as the product of the inelastic scattering Rutherford cross section [46] and the (comparably small) Coulomb excitation probability $P_{i \to f}$:

$$\left(\frac{\mathrm{d}\sigma}{\mathrm{d}\Omega}\right)_{i \to f} = \left(\frac{\mathrm{d}\sigma}{\mathrm{d}\Omega}\right)_{\mathrm{Rutherford}} P_{i \to f}. \tag{3.13}$$

The excitation probability $P_{i \to f}$ is defined by the excitation amplitude $a_{i \to f}$:

$$P_{i \to f} = \left|a_{i \to f}\right|^2. \tag{3.14}$$

This amplitude can be evaluated via time-dependent perturbation theory if it is assumed that the Coulomb potential $V_C(\mathbf{r}(t))$ is a small, time dependent perturbation:

$$a_{i \to f} = \frac{1}{i\hbar} \int_{-\infty}^{\infty} \mathrm{d}t \, \mathrm{e}^{i\omega_{fi}t} \left\langle f | V_C(\mathbf{r}(t)) | i \right\rangle, \tag{3.15}$$

with $\omega_{fi} = \left(E_f - E_i\right)/\hbar = \Delta E/\hbar$.

It is obvious now why it has to be ensured that the impact parameter is not too small. This formalism assumes that only the Coulomb potential contributes to the perturbation and this is only certain if nuclear contributions are excluded.

Now the potential $V_C(\mathbf{r}(t))$ can be expanded into its multipole components $V_{\lambda\mu}(\mathbf{r})$. In turn, these can be expressed in terms of electric and magnetic multipole matrix elements, $\mathcal{M}(\pi\lambda\mu)$, where $\pi = +1 \equiv E$ stands for electric transitions, $\pi = -1 \equiv M$ for magnetic transitions, λ is the multipolarity of the excitation and μ is its projection. The excitation amplitude written in those terms is then:

$$a_{i \to f} = i \sum_\lambda \chi_{i \to f}^{(\pi \lambda)} f_\lambda (\xi) \tag{3.16}$$

with $\chi_{i \to f}^{(\pi \lambda)}$ being a measure of the interaction strength,

$$\chi_{i \to f}^{(\pi \lambda)} \approx \frac{Z_t e \langle f | \mathcal{M} (\pi \lambda \mu) | i \rangle}{\hbar c b^\lambda}. \tag{3.17}$$

Exactly which $\mathcal{M} (\pi \lambda \mu)$ contribute to $\chi_{i \to f}^{(\pi \lambda)}$ and therefore to the sum in Eq. 3.16 depends on the initial and final state of the transition. Only certain combinations are allowed. For the transition from 0^+ to 2^+ only $\lambda = 2$ and $\pi = E$ is allowed (see Sec. 2.5). The function $f_\lambda (\xi)$ puts the cross section into connection with the *adiabaticity* of the reaction [45]. It is formulated in terms of the *adiabaticity* parameter, ξ, which can be expressed as the ratio of two time constants, namely the ratio of the collision time τ_{coll} (time the projectile spends in the vicinity of the target) and the timescale of the internal motion of the nucleus that is undergoing the excitation, τ_{nuc}:

$$\xi = \frac{\tau_{\mathrm{coll}}}{\tau_{\mathrm{nuc}}}. \tag{3.18}$$

The two times can be calculated as follows:

$$\tau_{\mathrm{coll}} = \frac{b}{\gamma v},$$
$$\tau_{\mathrm{nuc}} = \frac{1}{\omega_{fi}} = \frac{\hbar}{\Delta E} \tag{3.19}$$

with $\left(E_f - E_i \right) = \Delta E$. Low velocities, large excitation energies or large impact parameters result in a large ξ which means the reaction is adiabatic. This indicates the projectile moves gently through the Coulomb field, following the slowly changing, time-dependent potential

and it is not very likely that it gets excited. For large ξ the function $f_\lambda(\xi)$ should fall of exponentially as $e^{-\pi\xi}$. On the other hand, small values of ξ bring violent reactions and excitation is more likely to occur. As ξ approaches zero $(\xi \to 0)$ $f_\lambda(\xi)$ approaches 1.

As mentioned before it is presumed that the trajectories are straight lines which is not completely the case due to the Coulomb field repulsion. Alder and Winter showed that the introduction of a rescaled impact parameter takes this first order deviation from a straight line into account [45]. The distance of closest approach has to be increased by the following:

$$b \to b + \frac{\pi}{2}\frac{a_0}{\gamma} = b_a. \tag{3.20}$$

This results in the adjusted *adiabaticity* parameter:

$$\xi = \frac{\Delta E}{\hbar \gamma v}\left(b + \frac{\pi}{2}\frac{a_0}{\gamma}\right) = \frac{\Delta E}{\hbar \gamma v}b_a. \tag{3.21}$$

Adiabatic cutoff sets in when $\xi = 1$ and this corresponds to an impact parameter:

$$b_a = \frac{v\gamma\hbar}{\Delta E}, \tag{3.22}$$

which means that a maximum excitation energy of $\Delta E \approx \gamma\hbar v/b_a$ is possible.

The total cross section is obtained by summing up all contributions from all multipole matrix elements:

$$\sigma_{i\to f} = \sum_{\pi\lambda}\sigma_{\pi\lambda} \tag{3.23}$$

The individual cross section for the different multipole elements can be approximated by integrating the corresponding $\left|\chi_{i\to f}^{(\pi\lambda)}\right|^2$ from b_{min} to b_a:

$$\sigma_{\pi\lambda} = 2\pi \int_{b_{\text{min}}}^{b_{\text{a}}} b\, \mathrm{d}b P_{i\to f} \approx 2\pi \int_{b_{\text{min}}}^{b_{\text{a}}} b\, \mathrm{d}b \left| \chi^{(\pi\lambda)}(b) \right|^2 \tag{3.24}$$

resulting in:

$$\sigma_{\pi\lambda} \approx \left(\frac{Z_{\text{t}} e^2}{\hbar c} \right)^2 \frac{\pi}{e^2 b_{\text{min}}^{2\lambda-2}} B(\pi\lambda; 0 \to \lambda) \begin{cases} (\lambda - 1)^{-1} & \text{for } \lambda \geq 2 \\ \\ 2\ln(b_{\text{a}}/b_{\text{min}}) & \text{for } \lambda = 1 \end{cases}, \tag{3.25}$$

where $B(\pi\lambda; i \to f)$ is the reduced transition probability as defined in Eq. 2.33. For more details see Sec. 2.5. The direct dependence on Z_t, the target charge, is usually taken advantage of by using high-Z targets in experiments.

Equation 3.25 shows that there is a proportionality between the $B(E2 \uparrow)$ value and the Coulomb excitation cross section. It is also important to note again that for transitions from a 0^+ state to a 2^+ state only electric quadrupole transitions are allowed (see Sec. 2.5). This means that the sum in Eq. 3.23 has only one contribution, namely σ_{E2} and therefore there is a direct correlation between the total cross section $\sigma_{i\to f}$ and the sought after $B(E2; 0^+ \to 2^+)$ value.

All calculations using cross sections to calculate excitation strengths and calculations of angular distributions of γ rays are performed with a mathematica script described in [47]. For a more detailed calculation see [45, 47], the results are listed here. For completeness all the math that is the basis of the matematica script is included even though not all of it is used for this work.

The excitation amplitude is:

$$a_{i \to f} = -i \frac{Z_{\mathrm{t}} e^2}{\hbar v \gamma} \sum_{\pi \lambda \mu} G_{\pi \lambda \mu} \left(\frac{c}{v} \right) (-1)^\mu K_\mu \left(\xi \left(b \right) \right) k^\lambda \sqrt{2\lambda + 1}$$

$$\times \frac{\left\langle J_f M_f \left| \mathcal{M} \left(\pi \lambda - \mu \right) \right| J_i M_i \right\rangle}{e}. \quad (3.26)$$

$k = \Delta E / \hbar c$ and K_μ are modified Bessel functions. For electric transitions, the function $G_{\pi \lambda \mu} = G_{E \lambda \mu}$ is defined as ($\mu \geq 0$):

$$G_{E \lambda \mu} \left(\frac{c}{v} \right) = i^{\lambda + \mu} \frac{\sqrt{16\pi}}{\lambda \left(2\lambda + 1 \right)!!} \left(\frac{\left(\lambda - \mu \right)!}{\left(\lambda + \mu \right)!} \right)^{\frac{1}{2}} \left(\left(\frac{c}{v} \right)^2 - 1 \right)^{-\frac{1}{2}}$$

$$\times \left(\frac{\left(\lambda + 1 \right) \left(\lambda + \mu \right)}{2\lambda + 1} P_{\lambda - 1}^\mu \left(\frac{c}{v} \right) - \frac{\lambda \left(\lambda - \mu + 1 \right)}{2\lambda + 1} P_{\lambda + 1}^\mu \left(\frac{c}{v} \right) \right) \quad (3.27)$$

and for magnetic transitions, $G_{\pi \lambda \mu} = G_{M \lambda \mu}$ it is ($\mu \geq 0$):

$$G_{M \lambda \mu} \left(\frac{c}{v} \right) = i^{\lambda + \mu + 1} \frac{\sqrt{16\pi}}{\lambda \left(2\lambda + 1 \right)!!} \left(\frac{\left(\lambda - \mu \right)!}{\left(\lambda + \mu \right)!} \right)^{\frac{1}{2}} \left(\left(\frac{c}{v} \right)^2 - 1 \right)^{-\frac{1}{2}} \mu P_\lambda^\mu \left(\frac{c}{v} \right), \quad (3.28)$$

with P_λ^μ being the associated Legendre polynomials. For negative μ apply the easy relations:

$$G_{E \lambda - \mu} = (-)^\mu G_{E \lambda \mu},$$

$$G_{M \lambda - \mu} = (-)^{\mu + 1} G_{M \lambda \mu}. \quad (3.29)$$

The full cross section ends up to be:

$$\sigma_{i \to f} = 2\pi \int_{b_{\min}}^{\infty} \frac{b \, db}{2J_i + 1} \sum_{M_i M_f} |a_{i \to f}|^2$$

$$= \left(\frac{Z_t e^2}{\hbar c} \right)^2 \sum_{\pi \lambda \mu} k^{2(\lambda - 1)} \frac{B \left(\pi \lambda; J_i \to J_f \right)}{e^2} \left| G_{\pi \lambda \mu} \left(\frac{c}{v} \right) \right|^2 g_\mu \left(\xi \left(b_{\min} \right) \right), \qquad (3.30)$$

with $g_\mu \left(\xi \left(b_{\min} \right) \right)$ being defined as

$$g_\mu \left(\xi \left(b_{\min} \right) \right) = 2\pi \left(\frac{\omega}{v\gamma} \right)^2 \int_{b_{\min}}^{\infty} b \, db \left| K_\mu \left(\xi \left(b \right) \right) \right|^2$$

$$= 2\pi \int_{\xi}^{\infty} \left| K_\mu \left(x \right) \right|^2 x \, dx, \qquad (3.31)$$

which can be rewritten using modified Bessel functions:

$$g_\mu \left(\xi \left(b_{\min} \right) \right) = g_{-\mu} \left(\xi \left(b_{\min} \right) \right) = \pi \xi^2 \left[\left| K_{\mu+1} \left(\xi \right) \right|^2 - \left| K_\mu \left(\xi \right) \right|^2 - \frac{2\mu}{\xi} K_{\mu+1} \left(\xi \right) K_\mu \left(\xi \right) \right].$$

$$(3.32)$$

The angular distribution of γ rays emitted during Coulomb excitation processes is not isotropic due to the magnetic sub states not being equally populated [48]. The angular distribution can be parametrized as:

$$W \left(\theta \right) = \sum_{k \text{ even}} a_k P_k \left(\cos \theta \right) \qquad (3.33)$$

with k running from 0 to the smaller one of 2λ and $2J_i$. P_k are the Legendre polynomials. In [47] one can find that the coefficients a_k are given by:

$$a_k = \sum_{\mu L L'} \left| G_{\lambda \mu} \left(\frac{c}{v} \right) \right|^2 g_\mu (\xi) (-1)^\mu \begin{pmatrix} \lambda & \lambda & k \\ \mu & -\mu & 0 \end{pmatrix}$$

$$\times \begin{Bmatrix} J_f & J_f & k \\ \lambda & \lambda & J_i \end{Bmatrix} F_k \left(L, L', J_{ff}, J_f \right) \sqrt{2k+1} \, \delta_L \delta_{L'}. \quad (3.34)$$

The $\gamma - \gamma$ correlation function $F_k \left(L, L', J_f, J_i \right)$ is

$$F_k \left(L, L', J_f, J_i \right) = (-1)^{J_f + J_i - 1} \sqrt{(2k+1)(2J_i+1)(2L+1)(2L'+1)}$$

$$\times \begin{pmatrix} L & L' & k \\ 1 & -1 & 0 \end{pmatrix} \begin{Bmatrix} L & L' & k \\ J_f & J_i & J_f \end{Bmatrix}. \quad (3.35)$$

Chapter 4

Experimental Setup

4.1   Overview of the Setup

All measurements were performed at the *National Superconducting Cyclotron Laboratory* (*NSCL*) at Michigan State University [49]. Due to the short lifetime of ^{104}Sn, namely 21 seconds [6], this experiment had to be conducted in *inverse kinematics* with the projectile beam being excited, requiring the production of a radioactive ^{104}Sn beam. The radioactive beam for this experiment was produced by fragmentation of stable ^{124}Xe ions, also called primary beam. After the production of the primary beam ions in the *Electron Cyclotron Resonance* (*ECR*) ion source of the *NSCL*, they were accelerated to 15% of the speed of light in the *K500* cyclotron. After further stripping (producing higher charge states) and acceleration in the *K1200* cyclotron, the beam reached a velocity of roughly $\frac{v}{c} = 0.5$. The primary beam impinged upon a 240 mg/cm^2 ^{9}Be target to produce a wide variety of fragmentation products, also called secondary beam. A first selection of the fragmentation products of interest occurred within the *A1900* fragment separator [17] (see Fig. 4.1 for details).

Due to high contamination with less exotic fragmentation products, the secondary beam was sent to the *Radio Frequency Fragment Separator* (*RFFS*) [19] to increase the purity of the isotopes of interest. Finally, the beam was sent to the experimental station consisting of a 184 mg/cm^2 ^{197}Au target surrounded by the highly segmented *CAEsium iodide ARray* (*CAESAR*) [20]. In addition to *CAESAR*, other detectors were used including a Silicon *p-i-n*
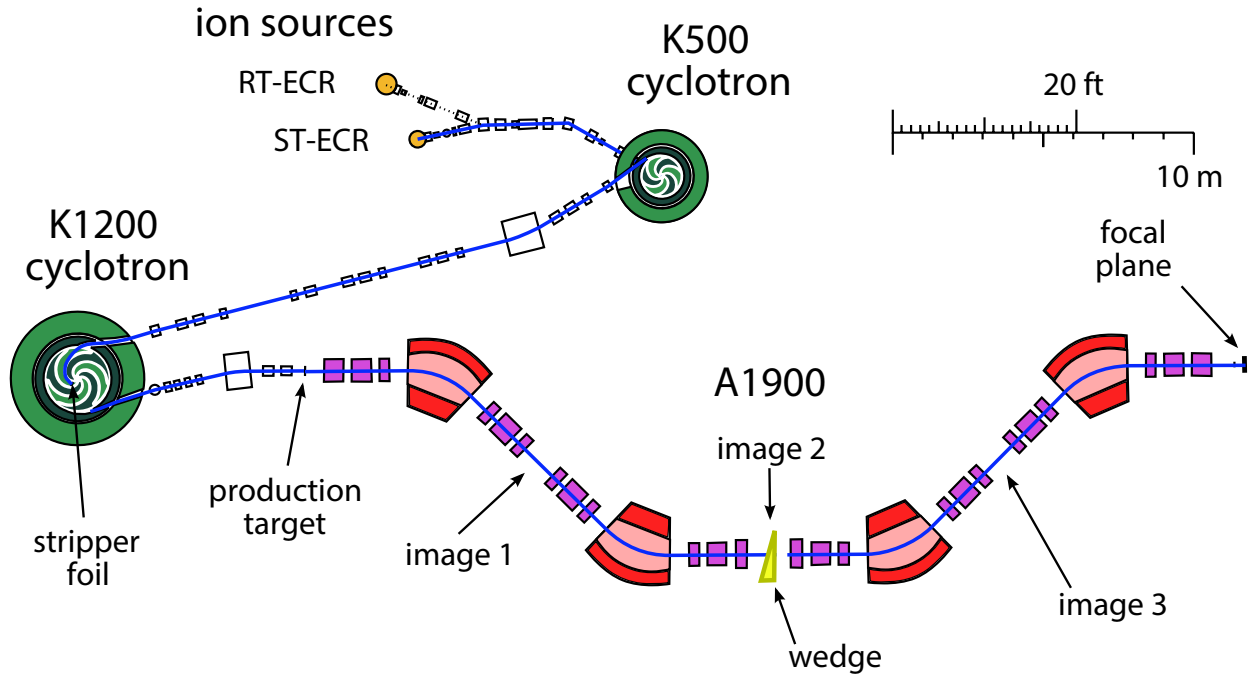
Figure 4.1 Schematic overview of the beam production at the NSCL. Figure is modified from [17].

detector for energy loss measurements, two thin plastic timing scintillators for time-of-flight (time it takes a projectile to travel a certain distance) measurements, one at the exit of the *A1900* (XFP position) and one at the exit of the *RFFS* (RF position), as well as a *Phoswich* detector for particle tagging and two *Parallel Plate Avalanche Counter* (*PPAC*) for position measurements (one in front and one after *CAESAR*). A layout drawing of the setup of the experimental station is shown in Fig. 4.2

The experiment was performed at the end of 2011 over a period of 7 days. In total 111 data runs with beam were recorded. This equals roughly 80 hours of beam data.
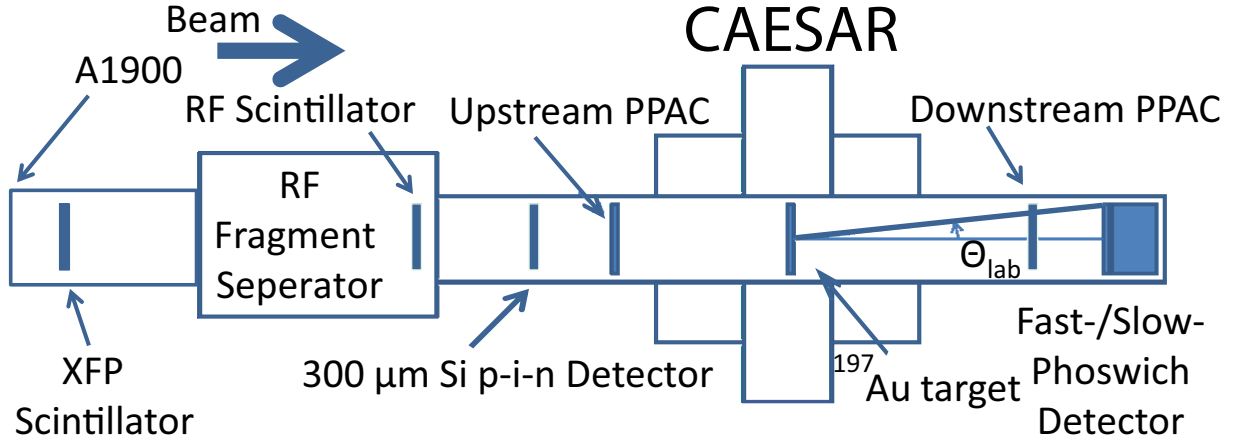
Figure 4.2 Schematic overview of the experimental setup after the *A1900* in the S2 experimental vault.

4.2 Radioactive Isotope Production

4.2.1 Primary Beam Production

The production of the stable beam starts at the ion source. Two different ion sources are available at the *NSCL* which are both based on the *Electron Cyclotron Resonance (ECR)* principle. The first one is the *Advanced Room TEMperature Ion Source (ARTEMIS)* [50] and the second one is the *Superconducting Source for Ions (SuSI)* [51,52] which was used for this experiment. The stable ^{124}Xe gas is injected into the source's plasma chamber. To create the needed plasma the few already existing free electrons are accelerated with a microwave field, this starts the ionization process which creates more free electrons and in the end the plasma. The microwave field is tuned to the electron cyclotron frequency ω_c:

$$\omega_\mathrm{c} = \frac{eB}{m_e},\tag{4.1}$$

where e and m_e are the electron charge and mass, respectively, and B is the magnetic field inside the plasma chamber. This magnetic field is created by a magnetic trap which is

needed to prevent the ions from escaping the source. The trap consists of six superconducting solenoid magnets which create a magnetic mirror field.

To reach the highest possible energy the ^{124}Xe was stripped of 20 electrons in the plasma and reached a charge state of ^{124}Xe^{20+}. At the end of the source the ions get extracted from the trap by an extraction system and then accelerated and focused before they are injected into the *K500* cyclotron.

The cyclotrons use a magnetic field (between 3 - 5 Tesla) to confine the beam and a radio frequency electric field for acceleration. The electric field is applied between the gaps of 3 "dees" and "hills" (see Fig. 4.3).

The Lorentz law gives the following dependence for the radius ρ of the motion [53]:

$$\rho = \frac{p}{Bq} = \frac{\gamma m v}{Bq}, \tag{4.2}$$

where p is the momentum, B the magnetic field strength, q the charge, γ the relativistic gamma factor, m the mass and v the velocity of the particle. The quantity $B\rho$ is often referred to as *magnetic rigidity* or just as *rigidity*. From Eq. 4.2 it is easy to see that $B\rho$ is:

$$B\rho = \frac{p}{q} = \frac{\gamma m v}{q}, \tag{4.3}$$

The radius of the circular motion of the beam depends on the velocity of the beam, as the beam gets more energetic and therefore faster, the radius grows. When the radius gets close to the radius of the cyclotron, the beam is extracted and gets transferred to the next cyclotron, the *K1200*. The final energy after the *K500* was 12.23 MeV/u for ^{124}Xe^{20+}. In the middle of the *K1200* is a carbon "stripper foil" which strips away more electrons and the result is a ^{124}Xe^{48+} beam which helps to increase the beam energy even more. After
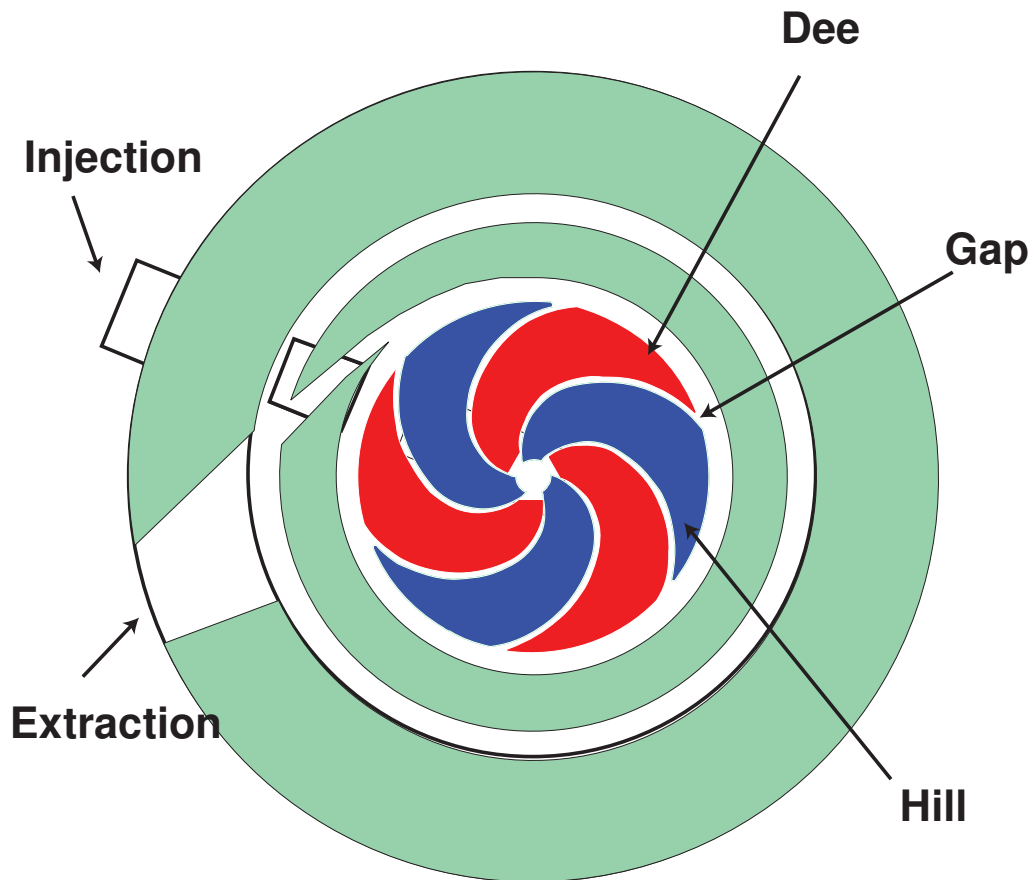
Figure 4.3 Schematic of the $K500$ cyclotron. The dees are red and the hills are blue. Figure is taken and modified from [5].

the $K1200$ the primary beam has reached a final energy of 140 MeV/u.

4.2.2 Secondary Beam Production

The beam of interest was produced by fragmentation of the primary beam on a stationary ^{9}Be target which is located after the $K1200$ cyclotron (see Fig. 4.1). A 240 mg/cm^2 ^{9}Be

production target was used. The primary beam was specifically chosen to achieve the highest yield possible of ^{104}Sn, according to a *LISE++* calculation [18]. The fragmentation can be described as a two-step process. First there is a highly excited *prefragment* created by removing some nucleons from the ^{124}Xe nucleus. In a second step, the *prefragment* decays by statistical nucleon emission [54] (abrasion-ablation model). Of course not only are the elements of interest produced but there are other, unwanted, fragmentation products, too. These "contaminants" include a wide range of stable and radioactive nuclei, as well as a high percentage of unreacted and now fully-stripped ^{124}Xe^{54+}. Therefore, it is very important to filter out the isotope of interest, which is the fully-stripped ^{104}Sn^{50+}.

The first filtering is done with *NSCL*'s *A1900* fragment separator [17, 55]. It is a three step process. It employs the $B\rho$-ΔE-$B\rho$ technique. The first step is a magnetic filtering with a $45°$ dipole magnet. Equation 4.3 shows that for a set $B\rho$ value, meaning a magnetic field with strength B and a path of radius ρ, only particles with a specific momentum to charge ratio, $\frac{p}{q}$, can pass through the dipole (p being the momentum of the particle and q its electric charge). Particles that are not in the range of this set value will either be deflected too much or too little and will run into either side of the magnet. Due to the size of the magnet, several radii are possible for the particles to take and a range of $\frac{p}{q}$ values can make it through this selection. Therefore, further purification is needed. Several slits are available that can be opened and closed in the separator. They are positioned at the image positions and at the focal plane of the $A1900$ (Fig. 4.1). Because of the difference in deflection in the dipole magnets, slits are used to block certain particles which restricts the total momentum spread. This means that contaminants that make it through the magnet but are deflected more or less than the nuclei of interest are blocked out. Several more magnets for focusing purposes are distributed along the beam line. The second step in the purification is an energy

loss filter with an achromatic Aluminum wedge degrader, consisting of a curved Aluminum foil [56]. To calculate the energy loss, the *Bethe formula* can be used [21]:

$$-\frac{\mathrm{d}E}{\mathrm{d}x} = \frac{4\pi e^4 Z_{\mathrm{p}}^2}{m_0 v^2} N Z_{\mathrm{t}} \left[\ln \frac{2m_0 v^2}{I} - \ln\left(1 - \frac{v^2}{c^2}\right) - \frac{v^2}{c^2}\right]. \tag{4.4}$$

$\frac{\mathrm{d}E}{\mathrm{d}x}$ is the differential energy loss per differential path length for a charged particle in the degrader material, e is the electron charge, Z_{p} and Z_{t} are the atomic numbers of the projectile and degrader respectively, m_0 is the electron rest mass, v is the velocity of the charged particle, N is the number density of atoms in the degrader and I stands for the average excitation and ionization potential of the degrader. Clearly the energy loss is proportional to Z_{p}^2 which means different elements lose different amounts of energy when they pass through the wedge, depending on their atomic number. This helps with the selection of the particles of interest, ^{104}Sn. In this experiment, the degrader used was a 150 mg/cm^2 Al wedge. The third and last step is again a $B\rho$ filter. The slits along the beam line were so far closed that the overall momentum acceptance was 0.41%.

This resulted in a ^{104}Sn purity of just 0.006%. The high levels of contamination originate from low-momentum tails of higher rigidity fragmentation products that extend exponentially and overlap with the momentum acceptance of the fragment separator [57]. Therefore, *NSCL*'s *Radio Frequency Fragment Separator* (*RFFS*) was used for additional filtering.

4.3 Radio Frequency Fragment Separator

The main reason for the high level of contamination are the low-momentum tails of higher rigidity fragments that extend exponentially and overlap with the momentum acceptance of the fragment separator [57]. The process of projectile fragmentation, which is used to produce

the secondary beam, leads to the fact that the produced fragmentation residues exhibit exponential-like tails on the lower end of the momentum distribution. This happens because a large fraction of the projectile's kinetic energy dissipates in the ^{9}Be target. Unfortunately, neutron-deficient isotopes like the ^{104}Sn have a smaller $B\rho$ compared to the more stable isotopes and therefore fall under those exponential tails of the more abundant isotopes. In Fig. 4.4 an example from a *LISE++* [18] simulation for the production of ^{104}Sn is shown.
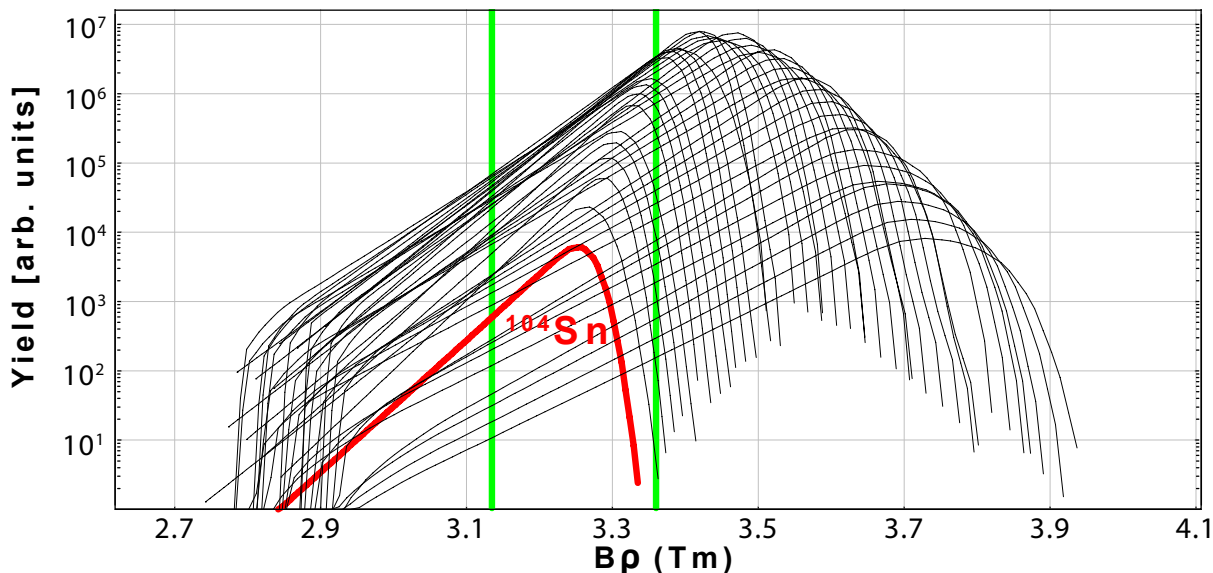
Figure 4.4 Simulation of the momentum distribution of the contaminants as well as ^{104}Sn that are produced during the fragmentation process for the settings used in this experiment. In red the ^{104}Sn is shown and in black the contaminants. The area in between the two green lines shows the momentum acceptance. The figure was made with *LISE++* [18].

It is evident that the order of magnitude of the amount of transmitted contaminants is many orders higher than the one for the ^{104}Sn isotope. It also shows that the yield of more less neutron-deficient contaminants increases exponentially with higher $B\rho$ settings, whereas the neutron-deficient isotopes show a steep fall off.

As the production and selection process within the *A1900* produces isotopes with very different velocities, this can be used as an advantage. The velocity of an isotope for a fixed $B\rho$
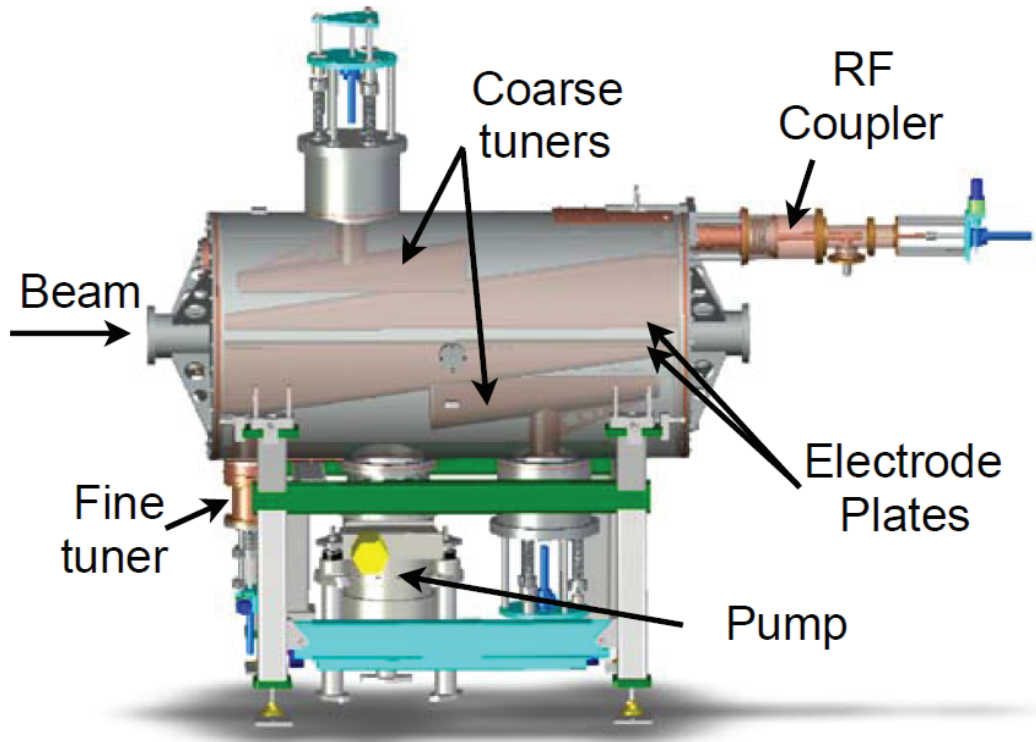
Figure 4.5 Top: Drawing of the *RFFS*; Bottom: Photo of the *RFFS*. Taken and modified from [19].

value is inversely proportional to its mass to charge ratio (see equation 4.3). This fact is used for further purification with the *Radio Frequency Fragment Separator* (*RFFS*) which is effectively a velocity filter.

A photo and drawing of the *RFFS* can be seen in Fig. 4.5. The cavity is 1.5 m long, has a gap of 5 cm, a peak voltage of 100 kV and operates at frequencies between 19 and 27 MHz (for this experiment it was tuned to match the cyclotron frequency of 23.1 MHz).

It employs a RF field perpendicular to the beam direction, synchronized with the RF of the cyclotrons. This leads to periodic deflections varying in magnitude for the different beam contaminants based on their velocities. The contaminants experience a different electric deflection than ^{104}Sn.

The transversal electric field leads to a phase dependent deflection of the different beam contaminants. It was tuned to deliver a maximum positive deflection for ^{104}Sn and a blocker was used to block out unwanted isotopes which were less deflected. In Fig. 4.6, a *LISE++* simulation for this setup is shown, where the Tin gets deflected the most in the positive direction and a majority of the contamination can be blocked out using a single-blade blocker. This process increased the ^{104}Sn purity in the secondary beam cocktail by two orders of magnitude (roughly a factor of 200). At the experimental end station downstream of the *RFFS*, the resulting rare-isotope beam was composed of 1.3% ^{104}Sn and 2.9% ^{102}Cd at average rates of 10 and 26 particles per second, for ^{104}Sn and ^{102}Cd, respectively.
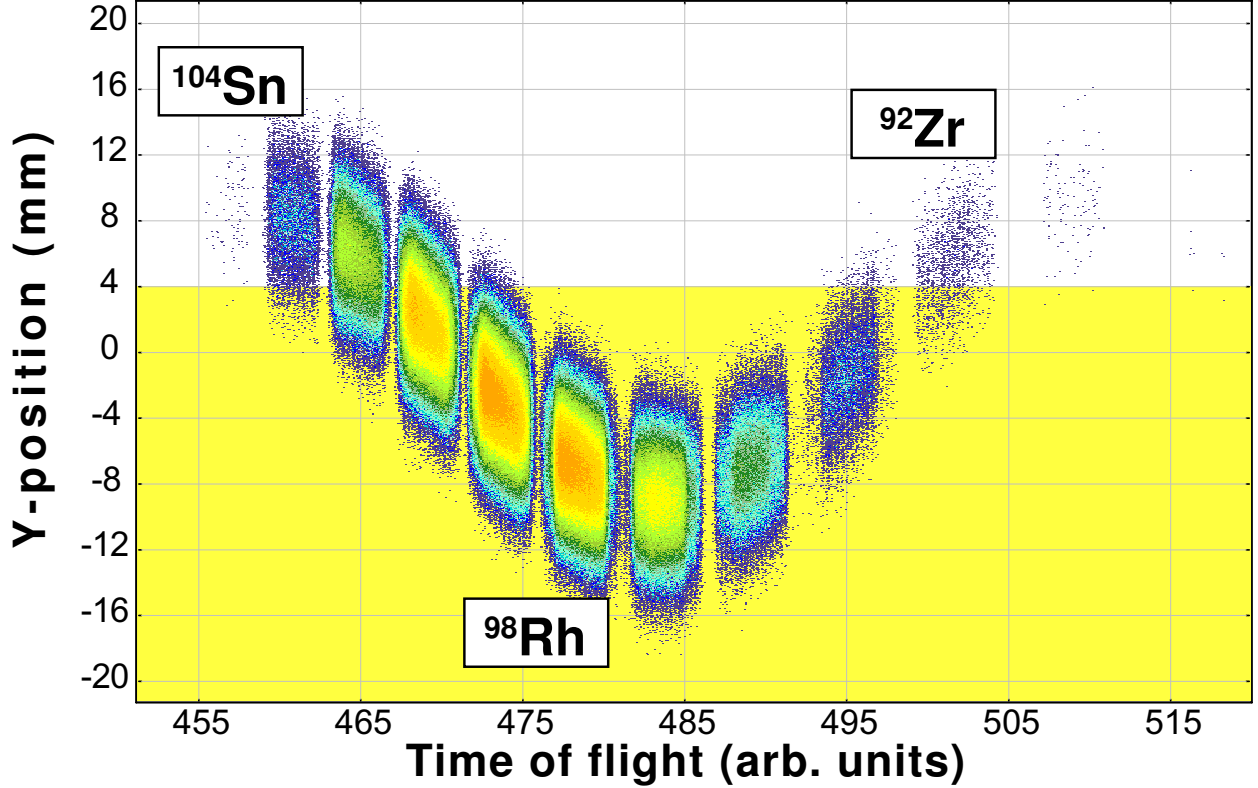
Figure 4.6 *LISE++* simulation for this setup. The yellow shaded area indicates the beam blocker at the end of the *RFFS*. Everything in the yellow area gets blocked out of the beam cocktail.

4.4   CAESAR

To measure the γ rays produced in the Coulomb excitation process, the CsI(Na) detector array called *CAESAR* [20] was used. For the intermediate-energy Coulomb excitation experiment that was performed here, the incoming even-even ^{104}Sn and ^{102}Cd nuclei were excited from the 0^+ ground state to the first 2^+ state in the Coulomb field of a gold target. This was followed by a prompt (in the order of a few pico seconds) de-excitation of the 2^+ state back to the 0^+ ground state by emission of a γ ray. To calculate a $B(E2\uparrow)$ value it is necessary to know how often this process happens compared to the total number of incoming beam particles (see Eq. 3.12 and 3.25). *CAESAR* surrounded the gold target used in this experiment. It was a 184 mg/cm^2 ^{197}Au target and placed in the center of *CAESAR*, about

12.8 m downstream from the *RFFS*. *CAESAR* consists of 192 detectors in total providing a solid angle coverage of 95% of 4π. 48 of the detectors use $3 \times 3 \times 3$ inch crystals and 144 were built with $2 \times 2 \times 4$ inch crystals. To optimize angle coverage and spatial granularity, a special geometry was applied, see Fig. 4.7 and 4.8 [20]. *CEASAR* is made out of 10 rings as shown in the figures. The first and last ring (ring A and J) hold 10 detectors each, the second and second to last ring (ring B and I) hold 14 detectors each and the remaining 6 rings (ring C-H) hold 24 detectors each. The high detection efficiency was needed due to the low production rate of the secondary beam ions ^{104}Sn (purity of just 1.3%). With this setup it is possible to reach a full-energy peak efficiency of 30% for 1 MeV γ rays. Because the nuclei are traveling at a large fraction of the speed of light, the emitted γ-ray energies are significantly Doppler shifted. This means the detected energy in the lab frame is connected to the energy in the projectile frame by:

$$E_\gamma^{\text{lab}} = \frac{E_\gamma \sqrt{1-\beta^2}}{(1-\beta\cos\theta)} = \frac{E_\gamma}{\gamma\,(1-\beta\cos\theta)}, \tag{4.5}$$

with θ being the angle of emission of the γ ray with respect to the direction of the beam. If β and θ are known, E_γ^{lab} can be *Doppler corrected* to obtain E_γ:

$$E_\gamma = E_\gamma^{\text{lab}}\gamma(1-\beta\cos\theta^{\text{lab}}). \tag{4.6}$$

As seen above, the Doppler corrected energy depends on the γ-ray emission angle. This necessitates a good spatial resolution (of the array) in order to determine the emission angle with acceptable precision (192 detectors).
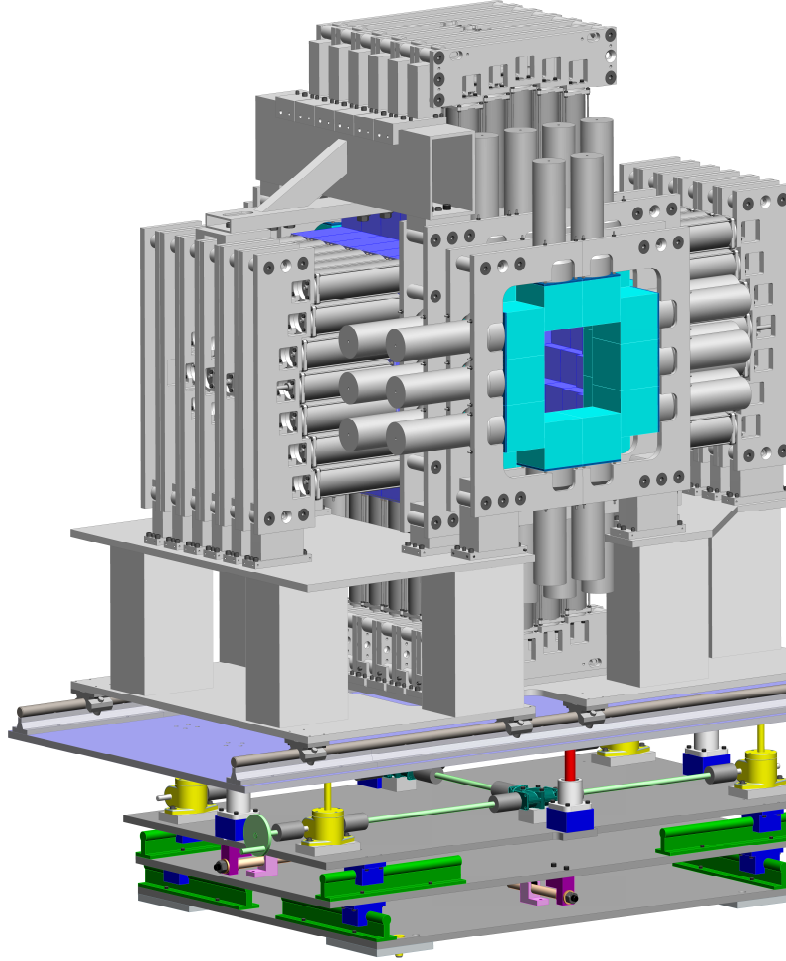
Figure 4.7 Technical drawing of the *CAESAR* setup. On the bottom is the mounting table shown with which one can move the array horizontally. On top of the table is *CAESAR* mounted. The mounting brackets are clearly visible as well as the detectors' *PMTs* and the encased crystals (green and blue).

To explain how γ rays are actually detected it is necessary to explain how they interact with matter and more precisely with the CsI(Na) crystals. There are three main processes which describe how γ rays interact with matter. These are the photoelectric effect, Compton effect and pair production. Each of these processes generates free electrons with a certain energy in the crystal which then subsequently create electron-hole pairs in the crystal. When those pairs recombine, the crystal emits light (a photon) with a wavelength in the visible spectrum (around 430 nm [21]). This light is then collected in a *Photomultiplier Tube* (*PMT*) and
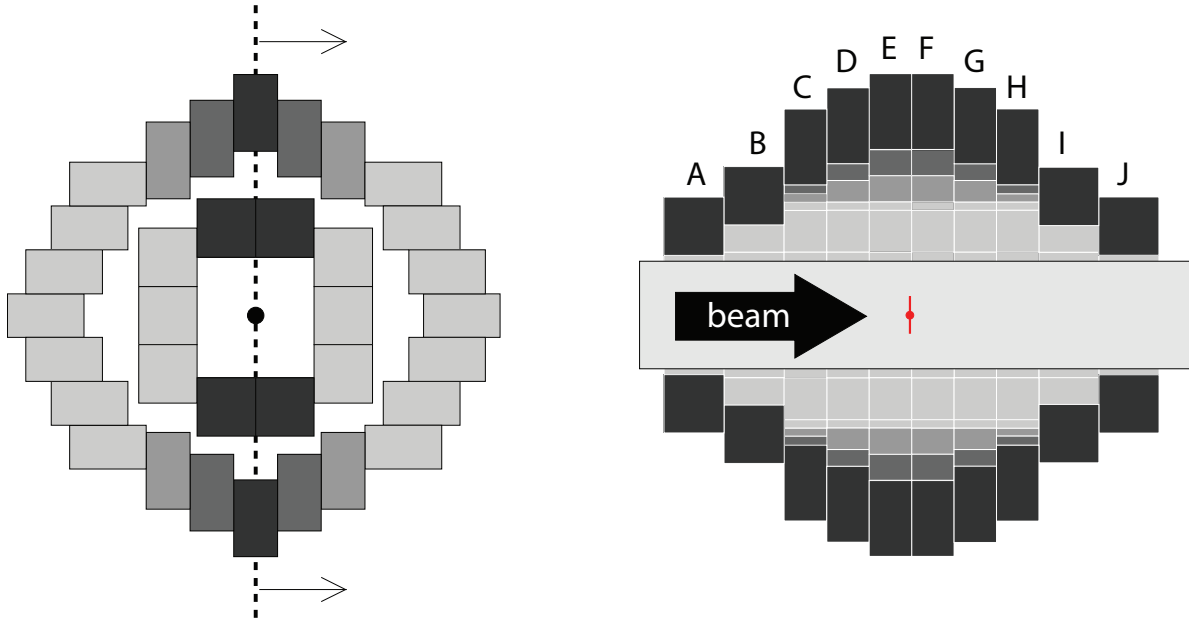
Figure 4.8 Schematic illustration of the arrangement of the *CAESAR* detectors. Left: cross sectional view of the rings F and J perpendicular to the beam axis. Right: Picture of the ten rings A (most upstream) to J (most downstream) with the target position in red. The gray scale corresponds to the position on the rings, as shown on the left. Picture taken and modified from [20].

transformed into a current that is proportional to the number of photons created in the crystal, which itself is proportional to the incoming γ-ray energy. A typical spectrum for mono-energetic γ rays is shown in Fig. 4.9. The different components of the spectrum are explained in Sec. 4.4.1-4.4.3.

4.4.1 Photoelectric Effect

The typical energy range within which the photo electric effect occurs is between a few tens of keV up to a few hundred keV. The γ ray is completely absorbed and an electron is ejected from the atom (see Fig. 4.10). The electron has a remaining kinetic energy of [21]

$$E_{e^-} = E_\gamma - E_b, \tag{4.7}$$
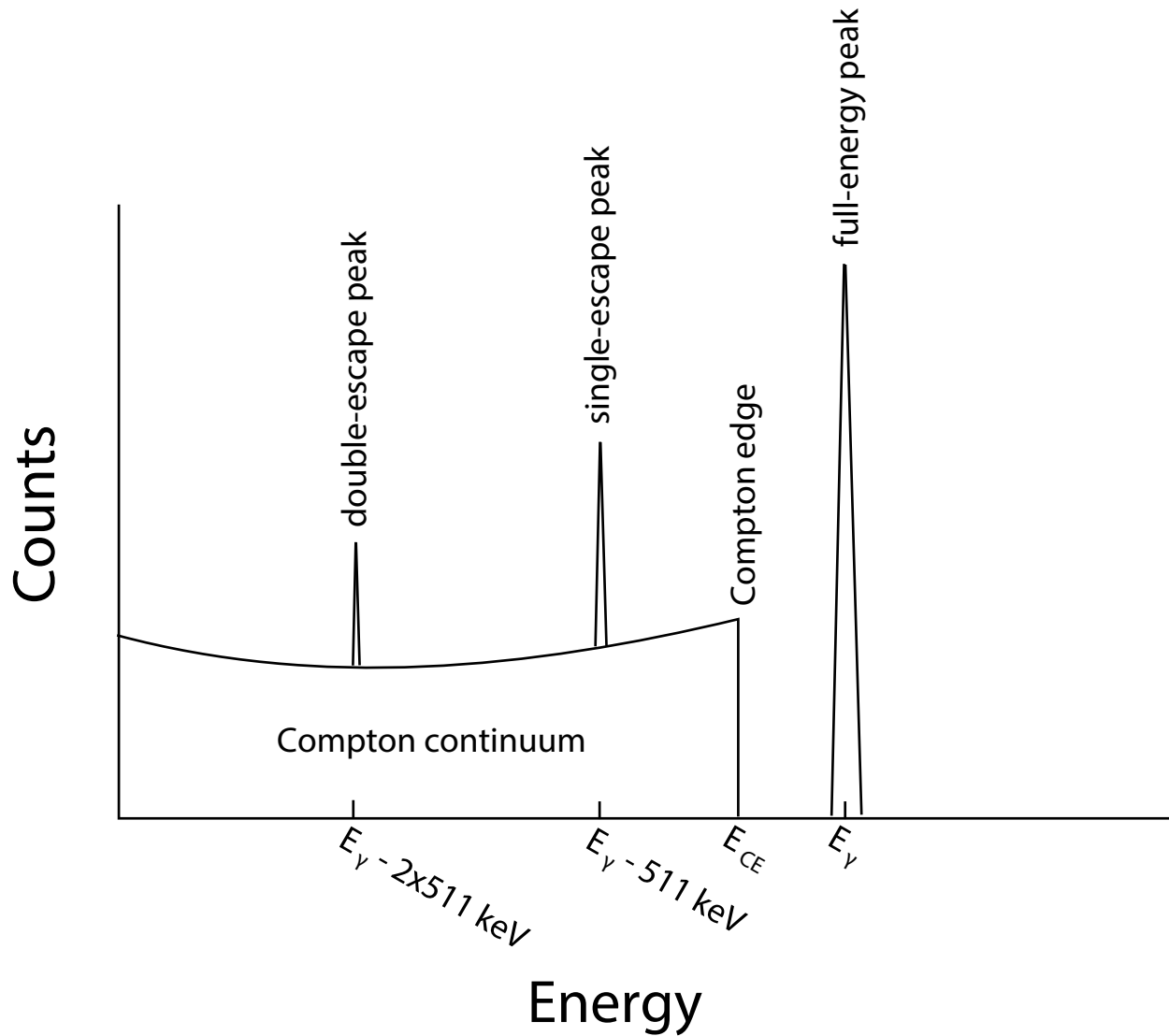
Figure 4.9 Example of a γ-ray detector response to many mono-energetic γ rays. The components of the spectrum are explained in the text. Picture taken and modified from [3].

where E_γ is the energy of the photon and E_b the binding energy of the electron. The probability per atom for this absorption to occur can be approximated by, $Z^n/E_\gamma^{3.5}$, where n slightly varies with the γ-ray energy and increases from about 4 at 100 keV to 4.6 at 3 MeV [58]. If the electron does not leave the detector volume then the full energy of the γ ray is detected and contributes to the *full-energy peak*.
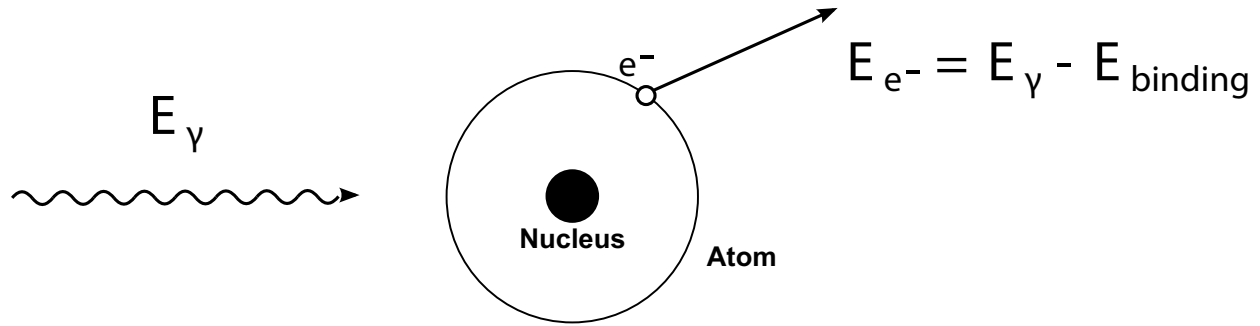
Figure 4.10 Schematic illustration of the photoelectric absorption process. Picture taken and modified from [3].

4.4.2 Compton Effect

The typical energy range within which the Compton effect occurs is between hundreds of keV and a few MeV. The photon scatters of an atom's electron and transfers some of its energy E_γ to the electron (see Fig. 4.11) (inelastic scattering). After the scattering process it has the energy E'_γ left. The partial energy transfer can be calculated as follows [59]:

$$\frac{1}{E'_\gamma} - \frac{1}{E_\gamma} = \frac{(1 - \cos\theta)}{m_e c^2},$$

(4.8)

which can be rewritten as

$$E'_\gamma = \frac{E_\gamma}{1 + \left(\frac{E_\gamma}{m_e c^2}\right)(1 - \cos\theta)}.$$

(4.9)

The transferred energy depends on the scattering angle θ. The upper and lower limits of the energy transfer are easily calculated. It is 0 MeV and

$$E'_\gamma(180°) = E_{CE} = \frac{E_\gamma}{1 + \frac{2E_\gamma}{m_e c^2}},$$

(4.10)

corresponding to the angles $0°$ and $180°$ respectively. This leads to the characteristic form

of the spectrum with the Compton edge and continuum. The broad feature in the spectrum between 0 and E_{CE} is called Compton continuum (see Fig. 4.9). If the scattered photon does not escape the crystal and gets fully absorbed after the scattering process in the same detector then this event contributes to the full-energy peak. This is because the full energy of the incoming photon is deposited in one crystal. This process has an angular distribution that follows the *Klein-Nishina formula* for the differential scattering cross section [21, 60]:

$$\frac{\mathrm{d}\sigma}{\mathrm{d}\Omega} = r_0^2 Z \left(\frac{1}{1+\alpha\,(1-\cos\theta)}\right)^2 \left(\frac{1+\cos^2\theta}{2}\right) \left(1+\frac{\alpha^2\,(1-\cos\theta)^2}{\left(1+\cos^2\theta\right)\left[1+\alpha\,(1-\cos\theta)\right]}\right),$$

$$(4.11)$$

where $\alpha \equiv E_\gamma/m_0 c^2$ and r_0 is the classical electron radius:

$$r_0 = \frac{1}{4\pi\epsilon_0}\frac{e^2}{m_e c^2} \approx 2.82 \times 10^{-15} \text{ m}.$$

$$(4.12)$$

Figure 4.11 Schematic illustration of Compton scattering. Picture taken and modified from [3].

4.4.3 Pair Production

If the incident γ-ray energy is larger than twice the rest mass of an electron ($2m_0c^2$=1.022 MeV) then pair production is possible. In the vicinity of a nucleus an electron-positron pair is produced and the energy that remains is transferred to kinetic energy (shown in Fig. 4.12).

$$E_{e^-} + E_{e^+} = E_\gamma - 2m_0c^2, \tag{4.13}$$

The positron will annihilate in the scintillator material almost immediately and thereby produce two back-to-back 511 keV γ rays. If one of those γ rays manages to escape the detector then this will show as the characteristic single-escape peak line at the energy:

$$E_{SE} = E_\gamma - 511\text{keV}, \tag{4.14}$$

and if both γ rays escape a double-escape peak is seen at:

$$E_{DE} = E_\gamma - 1.022\text{MeV}, \tag{4.15}$$

see Fig. 4.9.
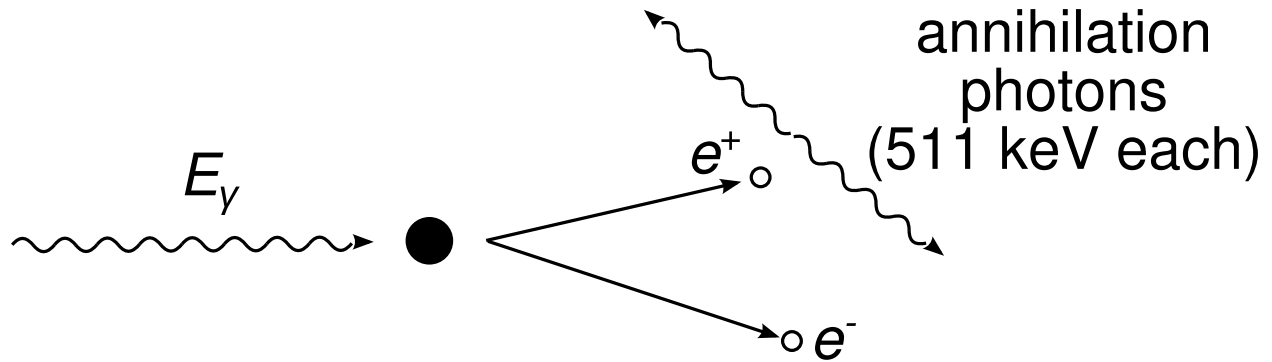
Figure 4.12 Schematic illustration of pair production. Picture taken and modified from [3].

4.4.4 CAESAR, the Array

Due to the low rates of very exotic beams, γ-ray detection efficiency plays a big role for constructing a γ-ray detector. *CAESAR* was designed to especially address this point. As mentioned, the array consists of 192 CsI(Na) detectors. It weighs roughly 300 kg in total.

The design and commissioning criteria for this array are discussed in [20]. The main goals were to achieve an in-beam energy resolution of 10% *FWHM* (full width at half maximum) or better for 1 MeV γ rays emitted from nuclei traveling at 40% of the speed of light. The material CsI(Na) was chosen to get the best cross section for interactions with γ rays which means a high-Z was important (see Eq. 4.4 and Sec. 4.4.1-4.4.3). The Sodium-doped Caesium Iodide used here has a higher stopping power than other common choices for scintillators, for example Thallium-doped Sodium Iodide (NaI(Tl)). Due to the arrangement of the detectors (see Fig. 4.8) some of them are partially shielded by others. This (and the size difference) results in the fact that not every detector detects the same number of γ rays even if they are isotropically emitted from a source at its center and simulations have to be used to model its in-beam response.

4.4.4.1 CAESAR, the Detectors

All detectors were build by ScintiTech. The housing is made of 1 mm thick Aluminum and protects the hygroscopic crystals from moisture. In between the Aluminum housing and the crystals there is a 1.5 mm thick layer of reflective material to improve the light collection. The Aluminum housing surrounds the front and sides of the crystals. The back of the crystal is attached to a round borosilicate window framed in Aluminum. This enables the connection to a *photomultiplier tube* (*PMT*).

In Fig. 4.13 a schematic of a detector is shown. The *photomultiplier tube* is coupled to the crystal. The *PMT* is necessary to convert the scintillation light into an electric current. As mentioned before, the number of scintillation photons is proportional to the energy of the detected γ ray. This results in the current being directly related and proportional to the γ-ray energy. The photons produced in the crystal hit the photocathode of the *PMT* and
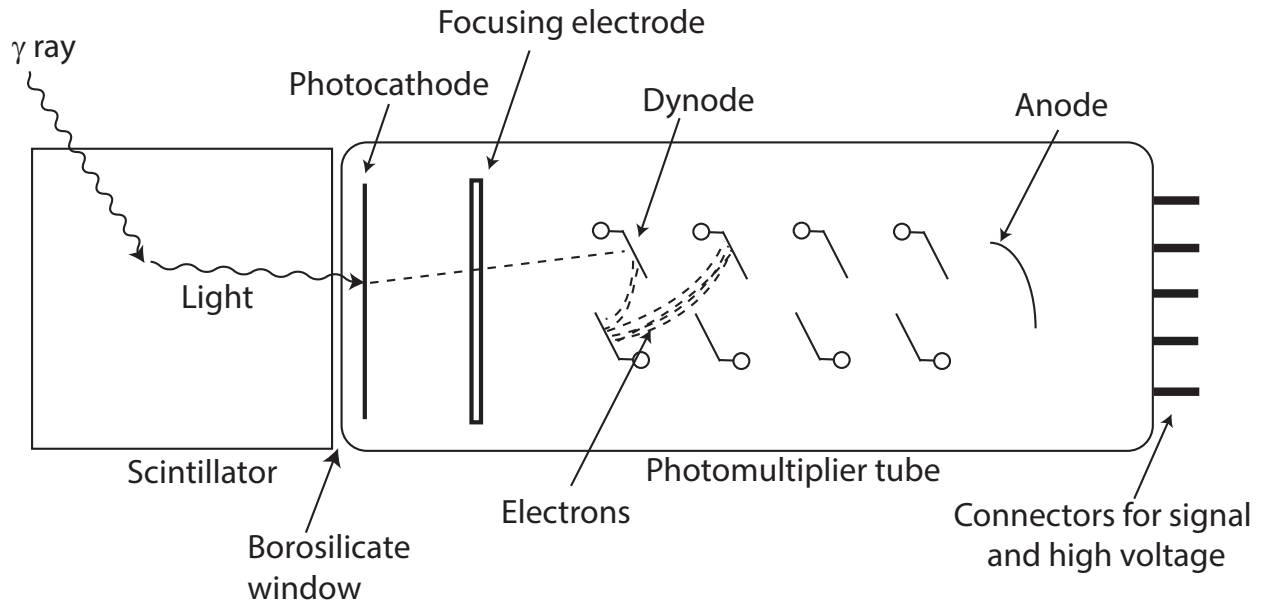
Figure 4.13 Schematic illustration of a detector. Picture taken and modified from [5].

produce electrons via the photoelectric effect (see Sec. 4.4.1). These then get focused by the focusing electrode and multiplied by a set of dynodes (see [21]). Between each dynode, a bias voltage is applied which increases from dynode to dynode. This leads to an acceleration of the electrons between each dynode. The material of the dynode is such that it produces a multiplication of the electrons every time it gets hit by an electron with a high kinetic energy. So this system leads to an amplification of the number of electrons at every dynode stage. In the end all those electrons are collected at the anode, producing a current signal which can be easily read out. It is proportional to the initial number of photoelectrons (and therefore the γ-ray energy). To get the best light transmission, the glass of the tube, placed in between the crystal and in front of the photocathode, was chosen to match the index of refraction of the detector material and window. The photo cathode itself is at the face of the *PMT* and is coupled to the crystal using optical grease. Two different *PMT*s are used for the *CAESAR* detectors, both made by Hamamatsu Photonics and also enclosed within an Aluminum casing. For the larger detectors the model R1307 (3 inch diameter) is used and

61

for the smaller detectors model R1306 (2 inch diameter). To allow for operation in magnetic fringe fields, several layers of μ-metal were added between the *PMT* and the Aluminum housing. Thanks to this shielding the detectors stay operable in fields up to 2-3 mT [20].

4.4.5 Energy Resolution

The energy resolution of the *CAESAR* detectors,

$$R = \frac{\Delta E_\gamma}{E_\gamma},\tag{4.16}$$

where ΔE_γ is the *FWHM* of the peak at energy E_γ [21], has three main contributions for in-flight data. The first part is the intrinsic energy resolution, ΔE_γ^{intr}, of the detectors for γ rays emitted from a resting source. The intrinsic resolution is defined as [21]

$$R_{intrinsic} \propto \frac{1}{\sqrt{E_\gamma^{intr}}}.\tag{4.17}$$

All *CAESAR* detectors have an intrinsic resolution that is better than 7 % for 1 MeV γ rays emitted at rest [20]. The second contribution comes from the uncertainty in the projectile's velocity, $\Delta\beta$, at the point of the γ-ray emission. The projectile looses energy (slows down) while passing through the target and for excited states with less than $\sim$ 1 ps lifetimes the γ-ray emission after Coulomb excitation can occur at any point in the target ($\sim$ 92 μm thick) and therefore results in this uncertainty. The last contribution comes from the uncertainty in the angle between the emitted γ ray and the scattered projectile, $\Delta\theta$. This uncertainty is dominated by the finite opening angles of the detectors. θ is determined for *CAESAR* by taking the angle between the center axis of *CAESAR* and the center of the individual detector that fired. In total, this results in the following energy resolution [61]:

$$\left(\frac{\Delta E_\gamma}{E_\gamma}\right)^2 = \left(\frac{\beta \sin \theta}{1 - \beta \cos \theta}\right)^2 (\Delta \theta)^2 + \left(\frac{\cos \theta - \beta}{\left(1 - \beta^2\right)\left(1 - \beta \cos \theta\right)}\right)^2 (\Delta \beta)^2 + \left(\frac{\Delta E_{\text{intr}}}{E_\gamma}\right)^2.$$
(4.18)

All quantities on the right hand side of Eq. 4.18 are in the lab frame. *CAESAR* has been optimized so that the intrinsic contribution is matched by the contribution of $\Delta \theta$ and $\Delta \beta$ for 1 MeV γ rays for velocities between 30% and 40% of c, leading to a total in-beam energy resolution of better than 10% FWHM [20].

4.4.6   Efficiency

To determine an absolute cross section for a specific γ-ray transition, it is important to know the number of emitted γ rays with this specific energy, not just the number of total detected γ rays. The number of observed γ rays, N_γ^{obs} is related to the number of emitted γ rays, N_γ via the absolute detection efficiency, ϵ:

$$\epsilon(E_\gamma) = \frac{N_\gamma^{obs}}{N_\gamma} = \frac{\# \text{ of detected } \gamma \text{ rays}}{\# \text{ of emitted } \gamma \text{ rays}}.$$
(4.19)

The efficiency is energy dependent and decreases with increasing energy of the γ ray. If the source of the emission is moving then the Doppler-shifted energy (see Eq. 4.5) has to be taken. In the case of a moving source, the Lorentz boost has to be taken into account, too, which effectively changes the solid angle coverage of the system. The angle of detection in the lab frame is related to the angle of emission in the projectile frame for photons ($\beta = 1$ and $E = pc$) by [46]:

$$tan(\theta_{lab}) = \frac{sin(\theta_{cm})}{\gamma(cos(\theta_{cm}) + 1)} \qquad (4.20)$$

with $\theta_{lab/cm}$ the angles of emission in the lab/projectile frame. If the angular distribution of the γ rays is isotropic in the projectile frame, then this leads to a forward focusing in the lab frame. The result is that the efficiency for a 1 MeV γ ray emitted at rest is different to one emitted at 30% to 40% of the speed of light. For spherical symmetric systems, the difference can be taken into account for the total efficiency by folding the detection efficiency with the boosted angular distribution of the emitted γ rays ($W(\Omega)$) [48]. But *CAESAR* is not spherically symmetric and therefore another approach is needed to obtain in-beam efficiencies. For this reason, T. Baugher *et al.* developed a *Geant4* [62] simulation [63] of the *CAESAR* array to take into account the complicated geometry of *CAESAR*, the target position, thickness and material, the aluminum housing, small gaps between detectors, the beam pipe, velocity of the projectile at the point of emission of the γ ray as well as lifetime effects and other experimental conditions. Measured source spectra and efficiencies agree with the *Geant4* simulations which were used to model the in-beam spectral response of *CAESAR* [63] (30% full-energy peak efficiency at 1 MeV [20], see also Sec. 5.4). The simulation takes into account detection efficiencies, angular distributions and the Lorentz boost. For more details on the simulation see Sec. 5.4.

4.5 Other Detectors

Three more detectors were used in this experiment. They are explained in detail in Sections 4.5.1-4.5.3.

4.5.1 *P-I-N* Detector

A *p-i-n* detector was used for energy-loss measurements of the incoming beam. This measurement was necessary for the particle identification process. The different incoming beam components can be distinguished by their difference in energy-loss and time-of-flight (see Sec. 5.2). A *p-i-n* detector is a type of semiconductor detector. In this case it was made out of Silicon and was 300 μm thick. It consists of three major layers. The main layer is the intrinsic Silicon semiconductor. Intrinsic means the material is not doped and has the highest possible purity. Due to the fact that every material has some impurities, the starting point was a slight p-type (positively doped) Silicon crystal and the so-called Lithium ion drift process [21, 64] was used to create an "intrinsic" Silicon crystal by compensating the acceptor impurities. This process creates also a highly doped n^+ layer which is used as an electrical contact on one side of the crystal. On the other side, due to the process, a p-type doped Silicon crystal was generated which is used as a contact, too, or a heavily doped p^+ layer is added (Fig. 4.14).
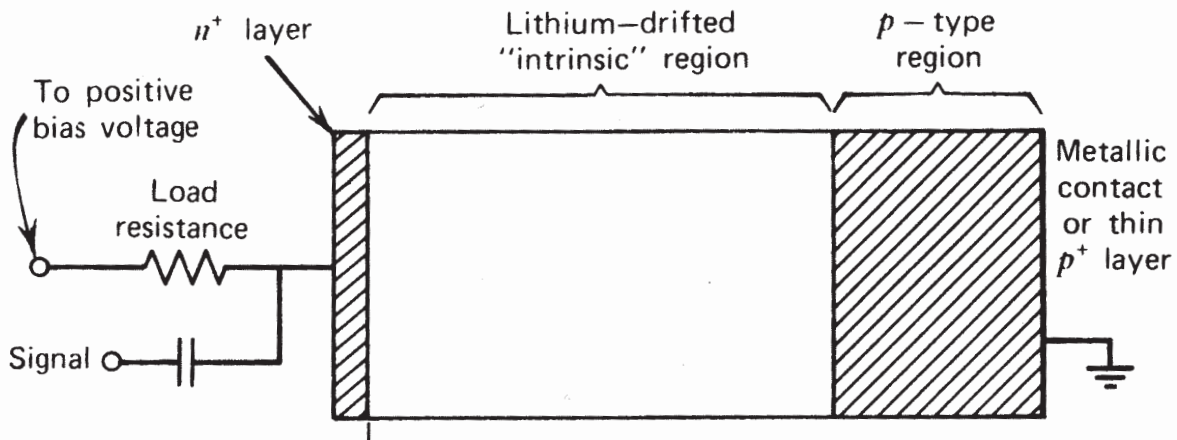
Figure 4.14 Schematic illustration of the regions in a *p-i-n* detector. Picture taken and modified from [21].

The crystal's compensated region is completely depleted and almost no leakage current exists

thanks to the p^+ and n^+ contacts. Because the intrinsic region ideally has no net charge and is completely depleted, every electron-hole pair created by beam passing through the material is collected. Therefore, the current signal provides a good measure of the energy loss of the ion passing through the detector. The name "p-i-n" comes from using the three different layers of the Silicon semiconductor, p-layer, intrinsic and n-layer.

4.5.2   Parallel Plate Avalanche Counters

*Parallel Plate Avalanche Counter*s (*PPAC*s) were used for position measurements, for example for the scattered particles after the reaction in the target. The *PPAC* used for this measurement was 583 mm downstream of the gold target. The *PPAC*s were developed and built at the *NSCL*. They provide a very small, uniform, energy loss (they do not influence the projectile too much, energy loss is less than 0.5 MeV per nucleon) while still having a good position resolution [65]. They consist of two parallel planar electrodes on either side of a central biased electrode. The central anode and cathode are close together, namely 3 mm apart, and the whole setup is enclosed by a container filled with the proportional gas isobutane at 5 to 7 Torr. A homogeneous electric field of approximately 600 V is applied between the electrodes. The two electrodes are stripped readout foils connected to a resistive divider chain, see Fig. 4.15.

When a charged particle passes through the detector, it creates two independent avalanches. The four signals at the end of the two resistor chains can be used to obtain a position measurement. This is done by comparing the strength of the two measured induced charges at one chain (see Fig. 4.16), performing a relative measurement this way.
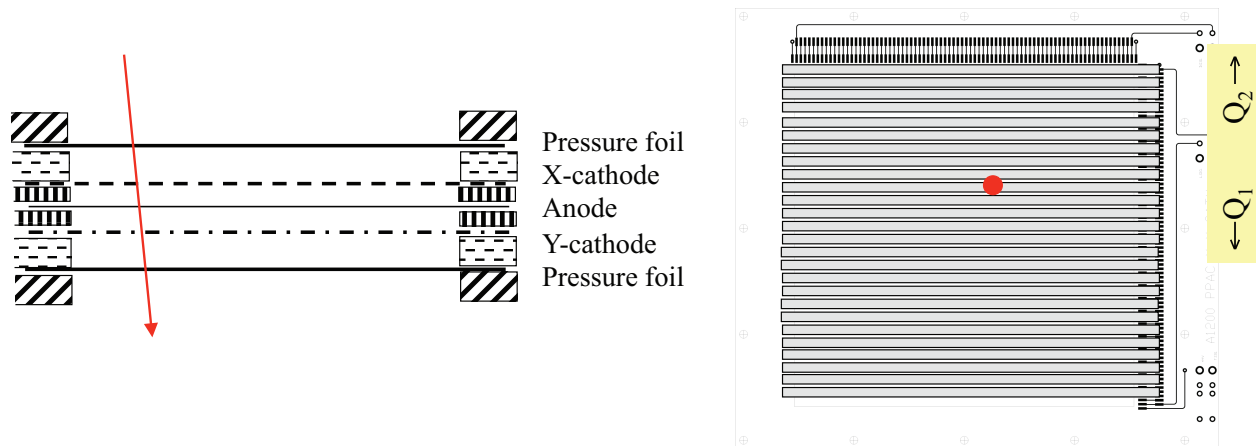
Figure 4.15 Schematic illustration of a PPAC detector. Left side is a cross section and the right side shows one side. Picture taken and modified from [22].

$$Position \propto \frac{Q_1 - Q_2}{Q_1 + Q_2} \tag{4.21}$$

Because the $PPAC$ is stripped in x and y, a clear position measurement can be achieved after it is calibrated with a "position mask" (see Sec. 5.1.2).
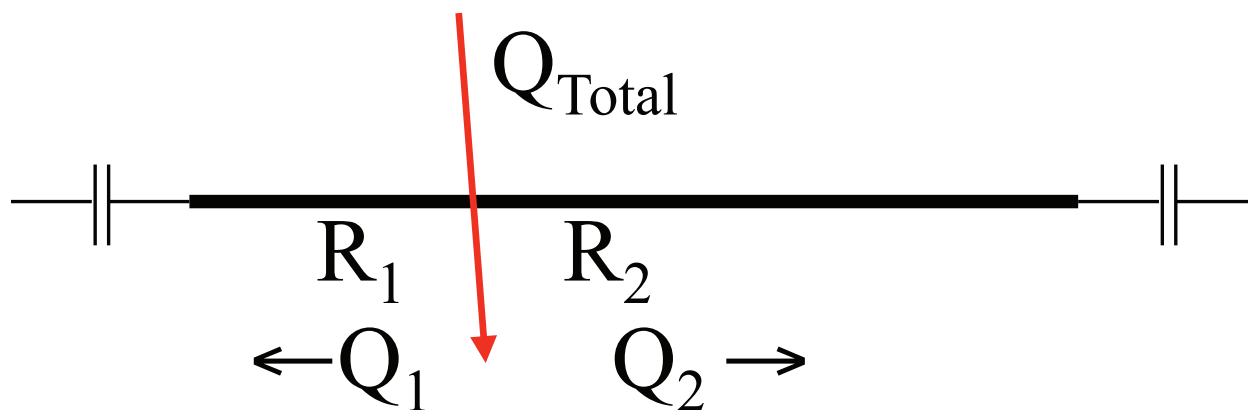
Figure 4.16 Schematic illustration of the resistor chain. Picture taken and modified from [22].

For more details on the specifications of how this detector is constructed, see D. Swan *et al.*, "A simple two-dimensional PPAC" [65].

4.5.3 Phoswich

A *Phoswich* detector is usually used for ΔE-E measurements and made out of two plastic scintillators and a single *PMT*. For this experiment it was mainly used as a particle trigger. *CAESAR* was read out in coincidence with it. The detector was located 0.96 m downstream of the gold target. The two scintillators are optically coupled and have two very different decay times. The first scintillator is a thin scintillator (1 mm) from ScintiTech with a very fast decay time. The second scintillator, also from ScintiTech, was thick enough (2 inches) to completely stop all particles in the beam cocktail and had a slow time constant. Both had a diameter of 6 inches and were connected to the *PMT* via a 6 inch long light guide that had a diameter of 6 inches on one side and 3 inches on the other. To prevent loosing energy in a dead layer between the fast and slow scintillator a special optical glue was implemented which was optimized for this purpose to connect all the parts. In Fig. 4.17 is a schematic shown of the detector.

The two different decay times of the scintillators lead to a very specific shape of the output pulse of the *PMT*. It is an overlap of the very fast signal and the slow signal (see Fig. 4.18). Depending on the relative contribution of the scintillation light from the two scintillators, the signal changes it shape [21, 66]. The two different decay times are needed so that it is clear which part of the resulting signal stems from which part of the detector.

Being able to distinguish between the two components is important for the ability to use the detector for ΔE-E measurements. To get the full energy deposited, it is necessary to integrate over the full signal of the *Phoswich* (fast and slow part combined) and to get the the energy loss information the same signal was integrated but with a constant time offset. The time offset enables skipping the first part (the fast part of the signal, main source of energy
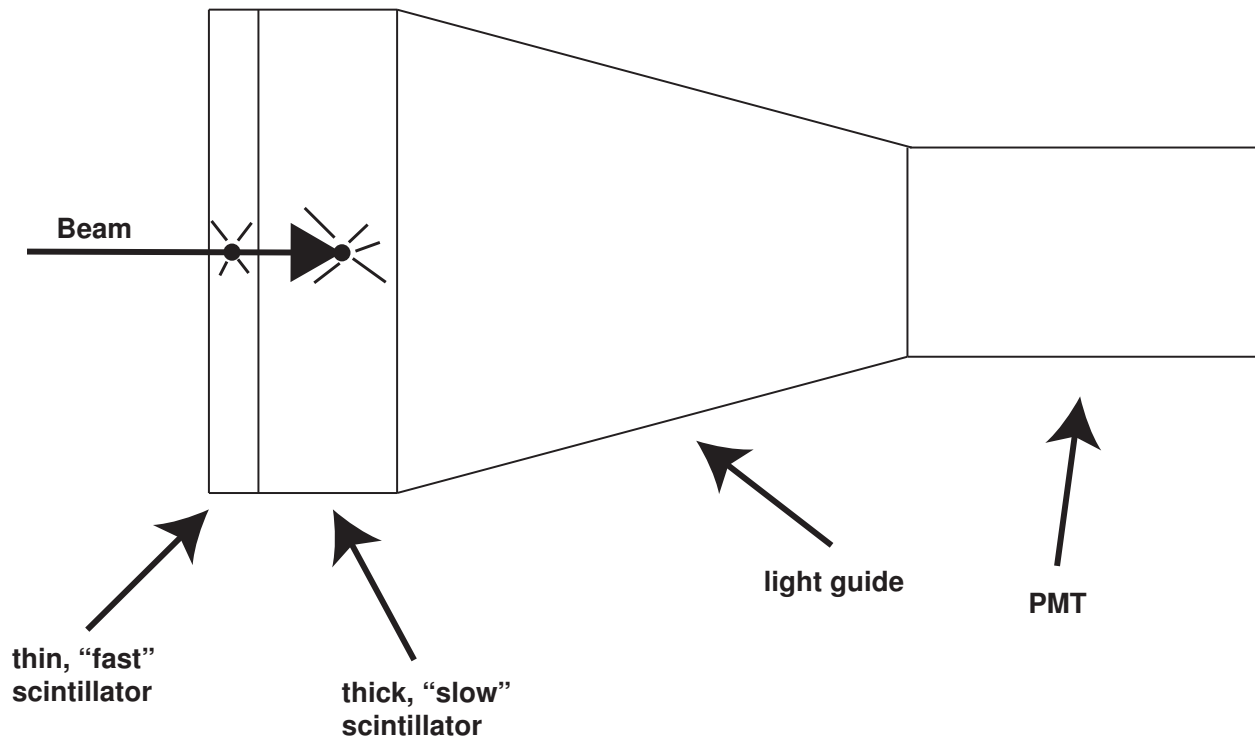
Figure 4.17 Schematic illustration of the *Phoswich* detector.

loss) and integration occurs only over the slow part [66] (see Fig. 4.18 for details). The result is an indirect measure of ΔE because the main energy loss happens in the first thin part of the *Phoswich* and integrating over the second part of the signal gives the information for E-ΔE.

Because of the limited resolution of the *Phoswich* detector for high-Z nuclei used here, it was not used mainly for ΔE-E measurements but as a particle trigger. A photo of the detector is shown in Fig. 4.19.

full signal, "fast" and "slow" part combined

energy loss integration range

"slow" part of the signal

"fast" part of the signal

full energy integration range
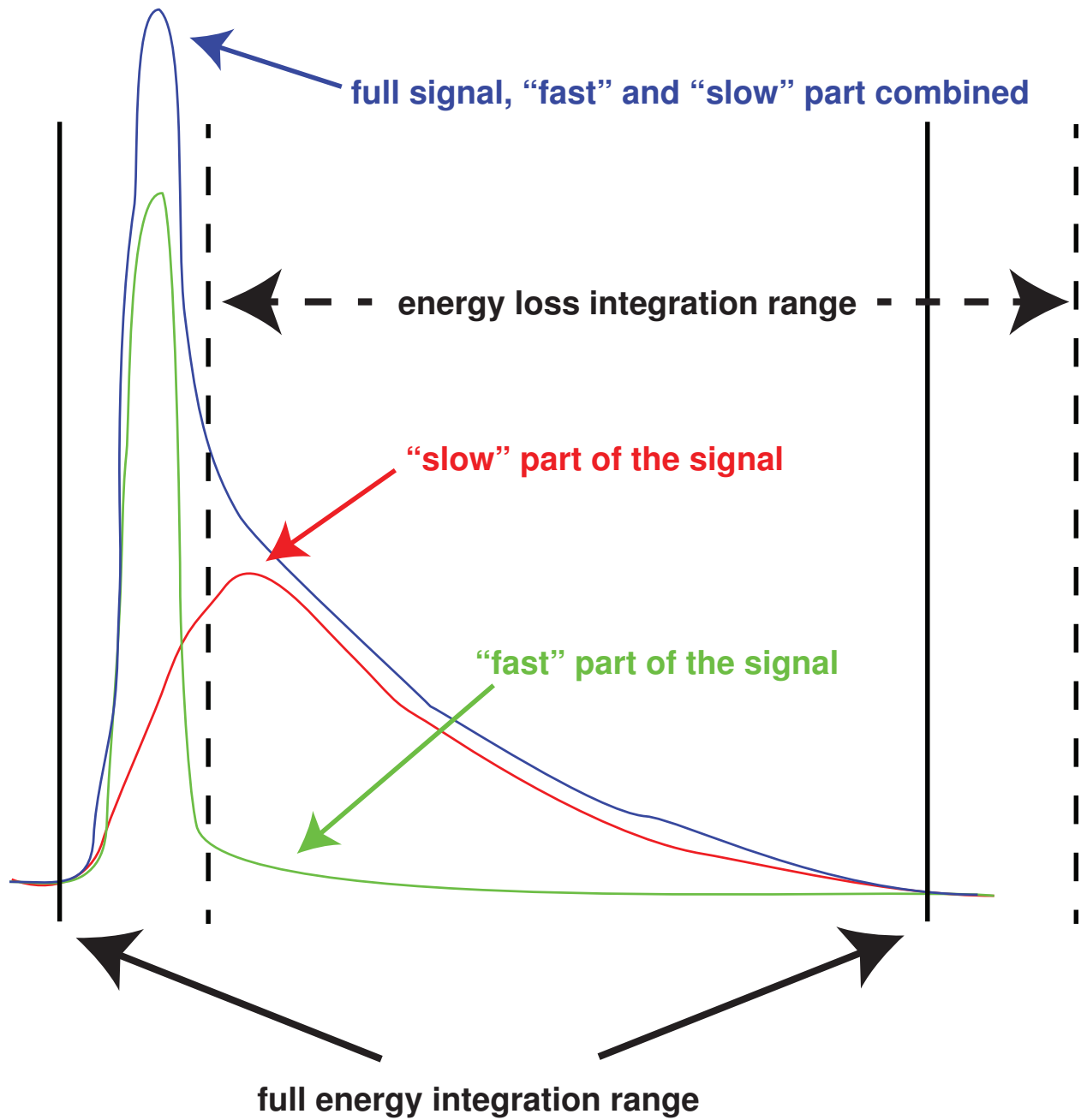
Figure 4.18 Schematic illustration of the *Phoswich PMT* signals and the integration ranges.

Figure 4.19 Picture of the *Phoswich* detector.

Chapter 5

Data Analysis

5.1 Calibrations and Corrections

The first step of the data analysis was to calibrate all detectors and also apply some corrections where necessary. In the following sections it is explained how the calibrations and corrections were done as well as why they were needed.

5.1.1 Energy and Time Calibration

The first calibrations done were energy and time calibrations of all 192 *CAESAR* detectors. The sources used for the energy calibrations are listed in Table 5.1.

Source	γ-ray energy 1 [keV]	γ-ray energy 2 [keV]
^{22}Na	511	1275.5
^{137}Cs	661.7	–
^{88}Y	898.0	1836.1
^{133}Ba	302.8	356.0
^{60}Co	1173.2	1332.5
background (^{40}K)	1460.8	–
background (^{208}Tl)	2614.5	–

Table 5.1 Calibration sources and energies.

Every peak in the source spectra was fitted with a Gaussian on top of a linear background. This was done for every single detector in the array. This way, the exact position of the

peaks in channel numbers was extracted. Fig. 5.1 shows the fit for a ^{88}Y source for one detector, where the x-axis shows the channel numbers.

After obtaining this information for every energy listed in Table 5.1 for every detector, the fitting for the energy calibration was done. To do the calibration fits, the γ-ray energy (in keV) is plotted versus the channel number and a polynomial of order two is fitted to the points for each detector. In Fig. 5.2 the calibration fit for one *CAESAR* detector is shown. The obtained function was then used to convert channels to energy (in keV).

All detectors were calibrated like this. Fig. 5.3 shows that the calibration worked well. It shows all 192 detectors on the x-axis and on the y-axis is the γ-ray energy (in keV) of a ^{88}Y source shown. For simplicity, 24 detector channels were plotted for all 10 rings but as mentioned previously (see Sec. 4.4), the first and last ring only have 10 detectors and the second and second to last ring only 14 instead of 24. This is why there are white bands visible in the Fig. 5.3. Proof that the calibration worked well is that the two main peaks in the ^{88}Y spectrum are clearly visible as horizontal bands and that they are aligned.

Next the timing information of every detector was calibrated. Every detector has its own timing information with 250 ps per channel dispersion. To ensure that all detectors are aligned and have the same time offset, the following was done. A part of the in-beam data with enough statistics was used and the timing information of all the detector hits with lab energies bigger than 1000 keV were plotted. This resulted in a strong peak due to *prompt* γ rays and a second, weaker peak due to *off-prompt* γ rays (see Fig. 5.4). *Prompt* γ rays come from reactions with the target and *off-prompt* γ rays come from reactions with material downstream of the target (e.g. the *Phoswich*). Because the *Phoswich* was located 0.96 m downstream of the gold target, the nuclei needed more time to reach it and therefore γ rays coming from reactions with it have this delay. These spectra were fitted for every detector
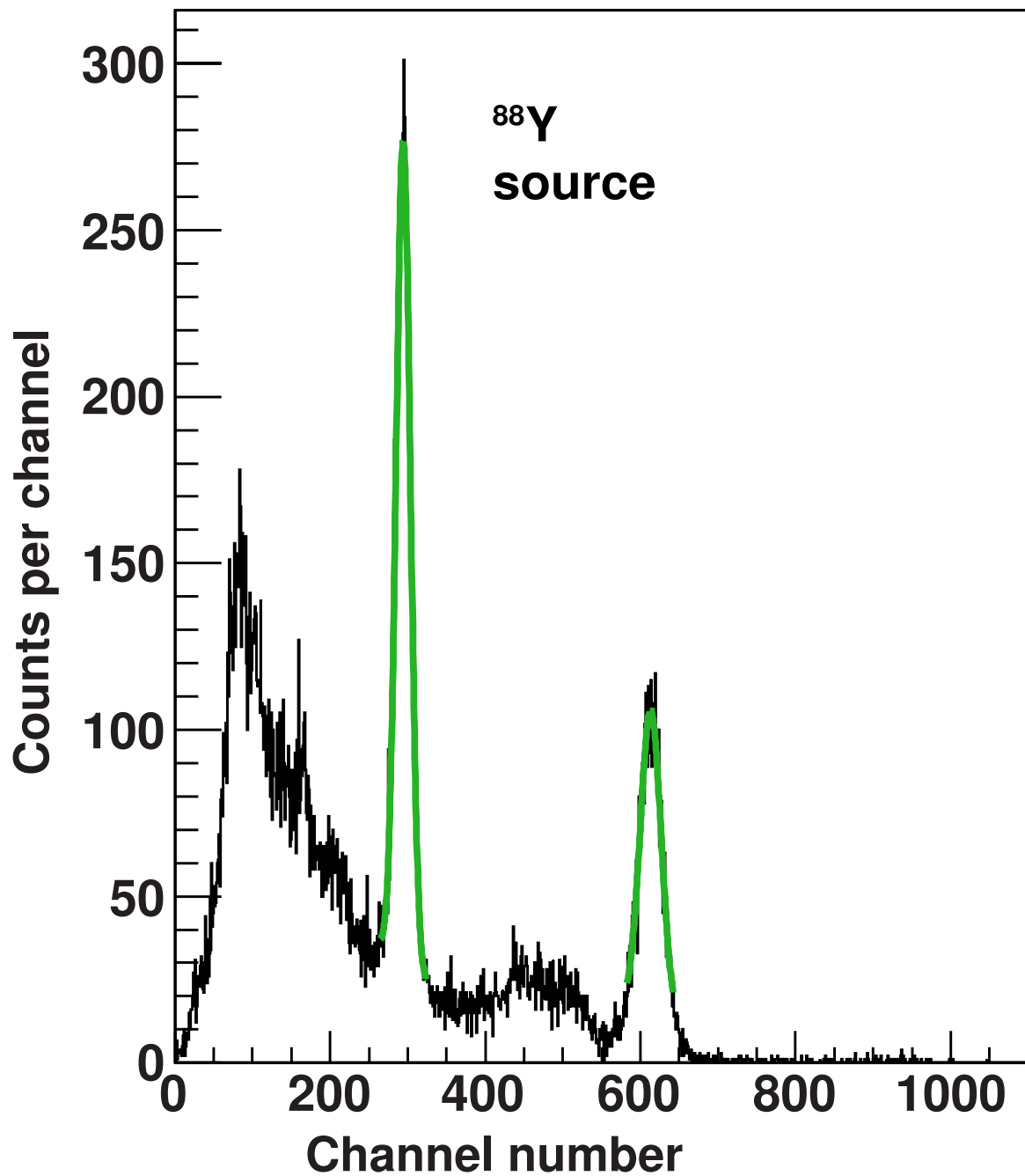
Figure 5.1 Uncalibrated ^{88}Y source spectrum for one *CAESAR* detector. The green lines show the two Gaussian fits used to determine the position of the peaks in channel numbers.
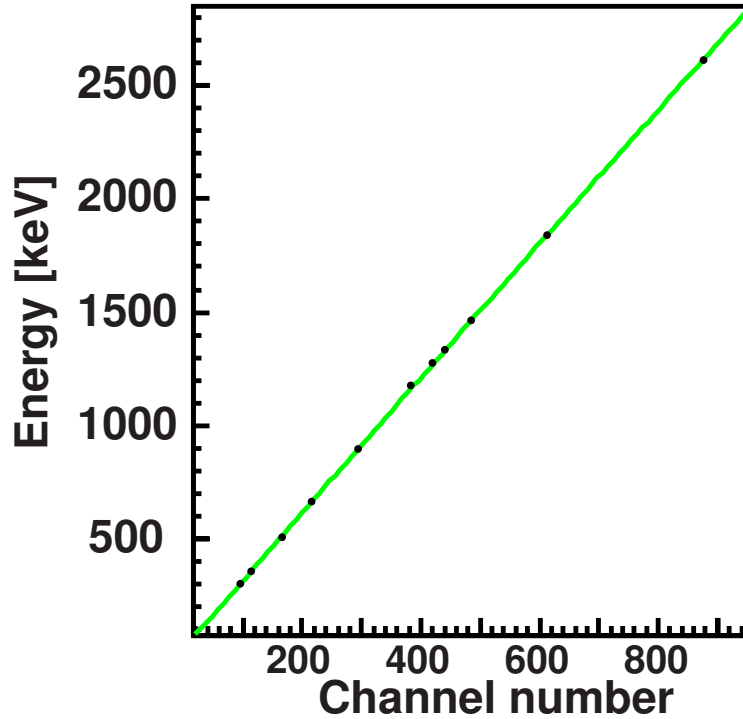
Figure 5.2 Source peak energies vs channel numbers for one detector. The green line is a polynomial of order 2 fit.

with a double Gaussian and the mean of the Gaussian corresponding to *prompt* γ rays (the first peak) was used as offset to center the timing for every detector. In Fig. 5.4 an example of the fit for one detector is shown. The blue line is the total fit, the green is the *prompt* part and the pink the *off-prompt* part.

That this method worked well can be seen in Fig. 5.5. All detectors are shown on the x-axis and the calibrated timing information on the y-axis. It is very clear that the times are very well aligned after the calibration. The white vertical lines have the same origin as the ones in the energy calibration (see Fig. 5.3).

To make sure that there was no shift during the experiment, the prompt position for all 111 runs for energies bigger than 500 keV were checked. The positions changed by less than 8 channels (equaling 2ns) which is a lot smaller than the width of the *prompt* timing peak therefore no additional corrections were needed (see Fig. 5.6).
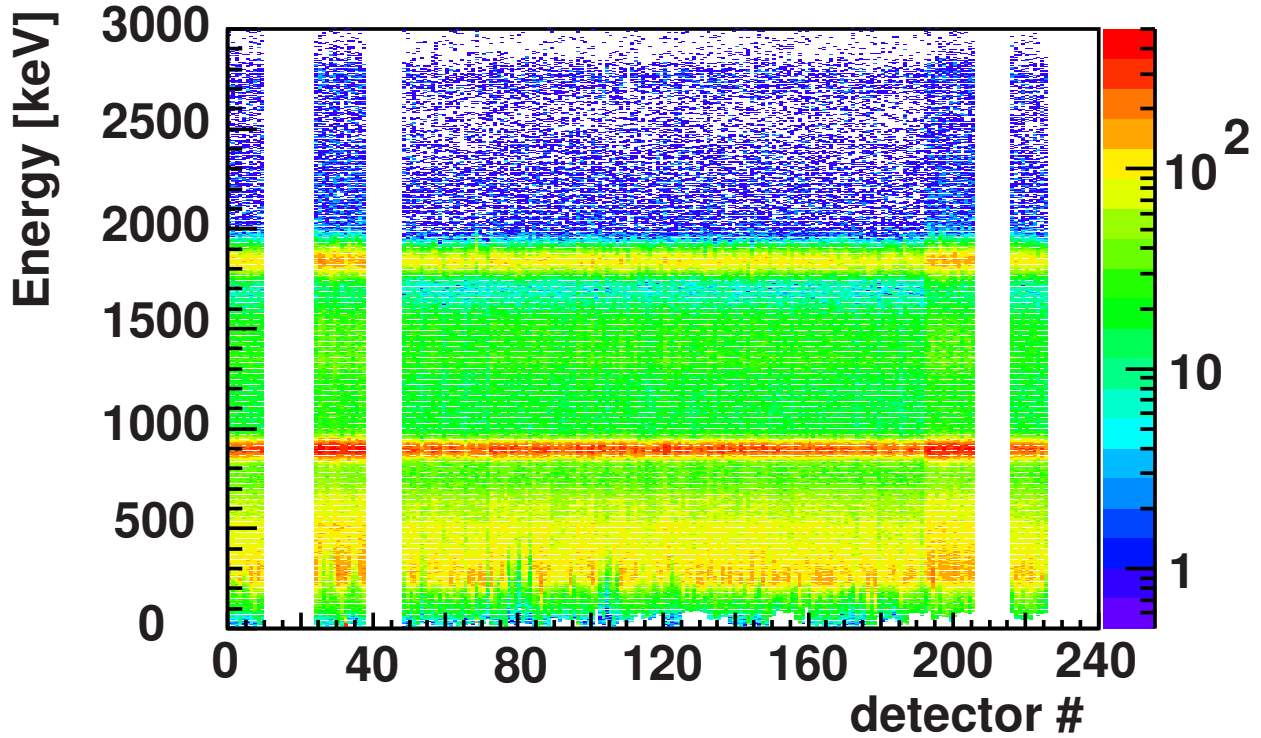
Figure 5.3 Overview of all detectors and their calibrated energies for a ^{88}Y source.

The times needed to be aligned so that one universal time-cut could be applied to all *CAE-SAR* detectors simultaneously (see Sec. 5.3.2.1).

5.1.2 PPAC Calibration

The calibration of the *PPAC* was done with a position mask. In front of the downstream *PPAC* was a mask which was used for the position calibration. The position mask was made out of a piece of metal with very well defined small holes and openings (in the order of few millimeters). If the position mask is inserted in front of the *PPAC* in the path of the beam, then the ions can only pass through the well-known openings. There was no position mask in front of the upstream *PPAC* but it was possible to do a coarse calibration by using the calibration of the downstream *PPAC* and the known dimensions of the *PPACs*.

In Fig. 5.7 a calibration run for the downstream *PPAC* is shown. With the knowledge of how
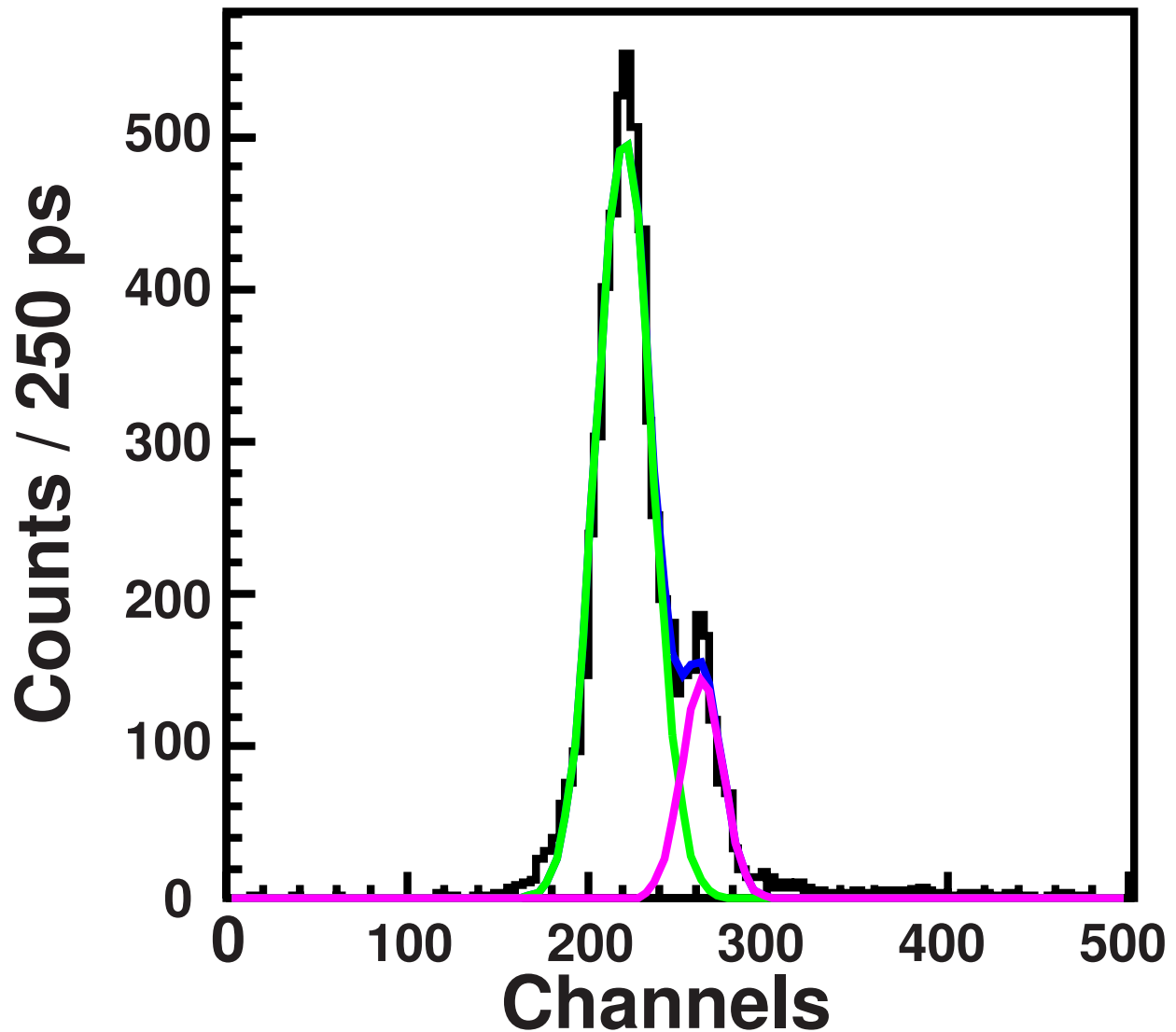
Figure 5.4 Example of the time calibration fit, see text for details.

far apart the different holes in the mask are, the gain in the x and y direction was determined.

To determine the positions of the holes in channel numbers the mean values of the features

corresponding to the holes were used. This was done for all clearly visible holes and the gain

was calculated for every row and column of holes. As a final value for the gain in the x and y

direction, the mean value of the different gains for the different rows and columns was used

respectively. The uncertainty of the position measurement was $\sigma = 1.5$ mm. It was also

checked that there was no pillow effect (because the $PPAC$ is filled with gas (see Sec. 4.5.2)
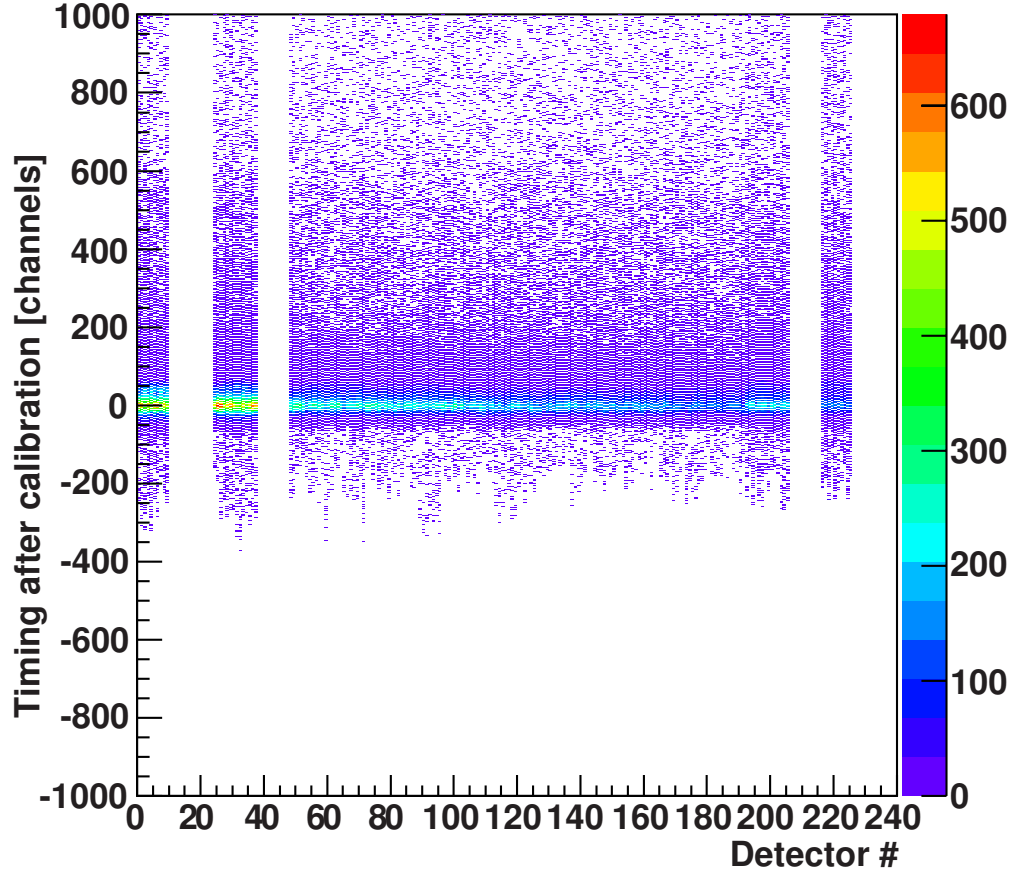
Figure 5.5 Overview of all detectors and their calibrated timing information.

the surface of the *PPAC* could have been bent outwards). The necessary offset in the x and y direction was determined for every beam component individually. It was made sure that the *PPAC* was centered for coincidence data which was used for the scattering angle cuts. This was done because only one *PPAC* was available behind the target and therefore the assumption was made that on average the beam was centered. See Sec. 5.3.2.2 for details. The total difference in the offsets for ^{104}Sn and ^{102}Cd was 12 mm (7.1 mm in x and 9.6 mm in y).

With this knowledge it was possible to do a coarse calibration of the upstream *PPAC*, too. It was done by ensuring that the gains used for the upstream *PPAC* resulted in the fact that the overall image size of the *PPAC* was the same as the downstream *PPAC*.
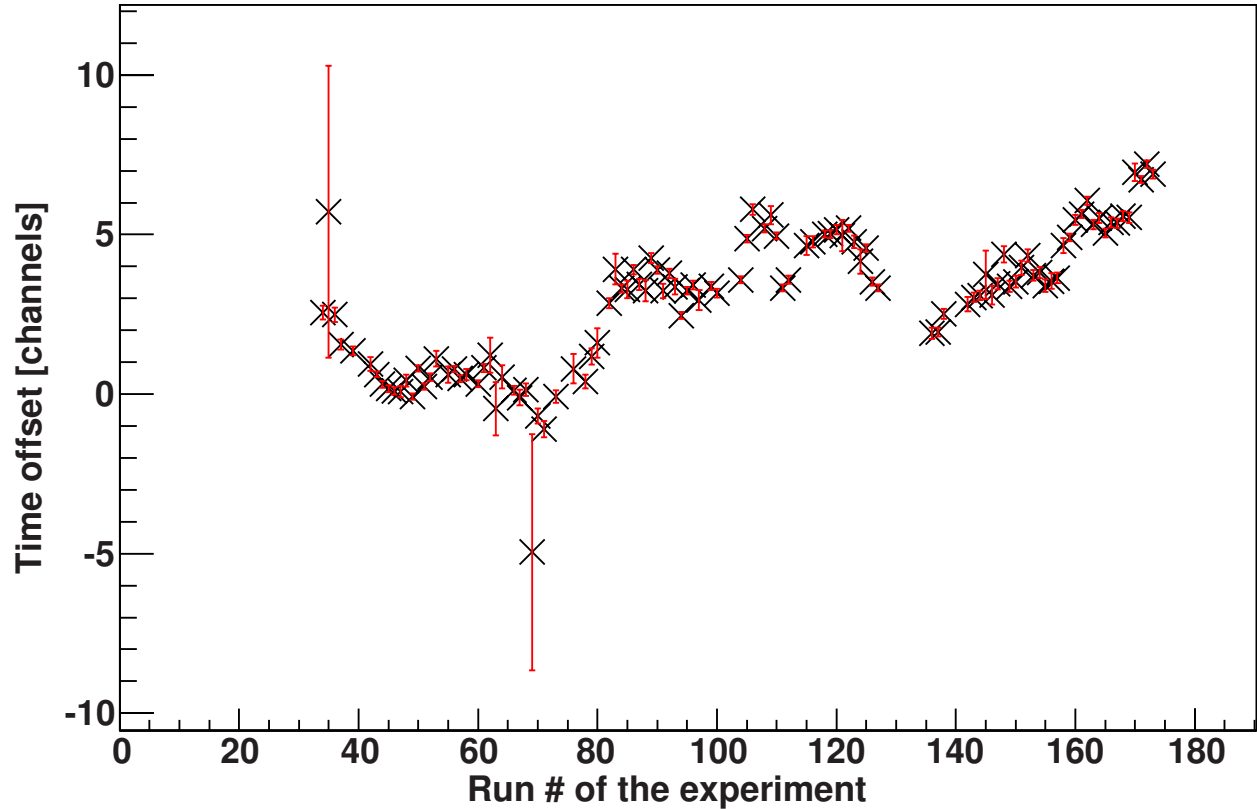
Figure 5.6 *Prompt* timing peak position for all 111 runs of the experiment for γ-ray energies greater than 500 keV.

All events with a bad position measurement were omitted from the analysis. This means events where only the left or right information or only one up or down information was available and therefore it was not possible to get an x or y position (see Sec. 4.5.2).

During a dedicated pilot beam, tuning, no-target run it was made sure that the beam was focused at the target position. A good focus was achieved during the available time. In Fig. 5.8 the x versus corresponding angle and y versus corresponding angle plots are shown at the target position, upstream *PPAC* and downstream *PPAC* position.

With this no-target run, the beam spot size at the target position was determined, too. Fig. 5.9 shows the projection onto the x-axis and y-axis in mm for the beam species ^{102}Cd. The beam spot has a $\sigma \leq 5.5$ mm in any direction and is the same for any beam species that is
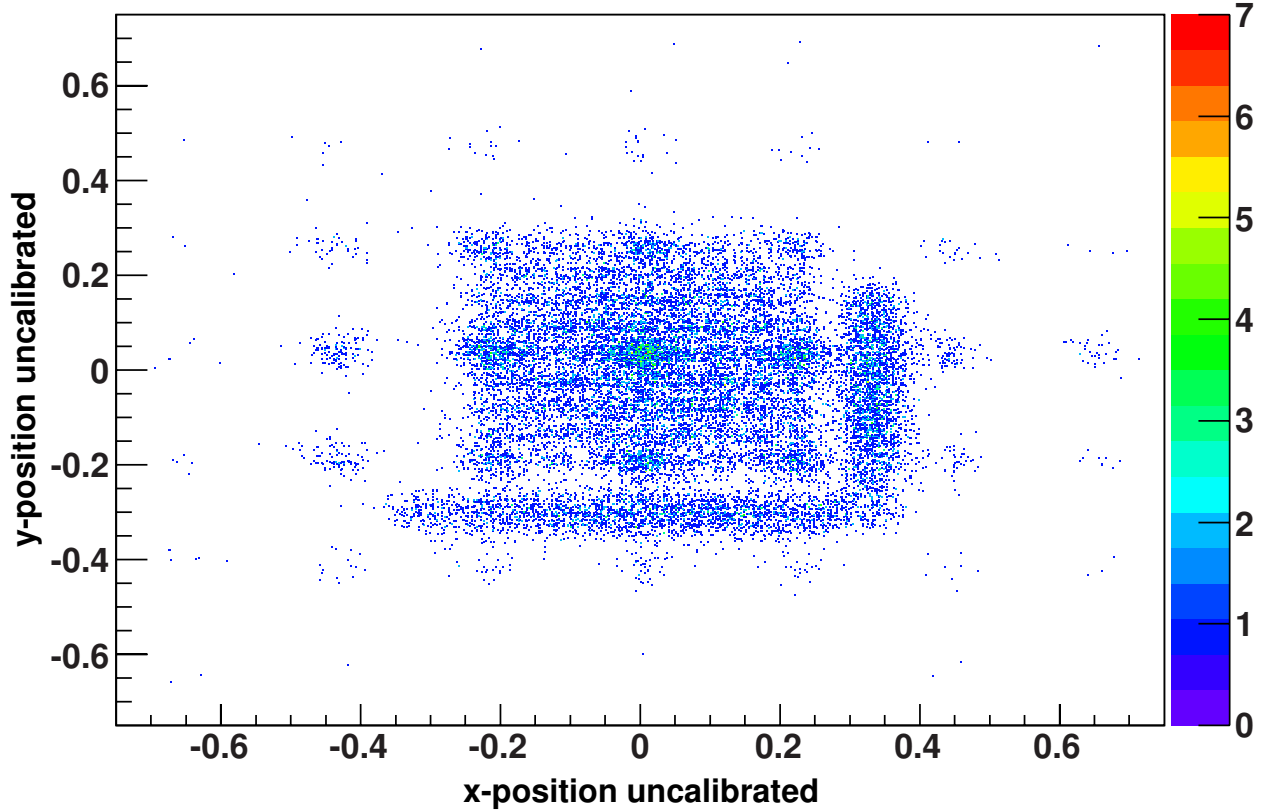
Figure 5.7 Uncalibrated mask run for the downstream *PPAC*. The positions of the different features correspond to the positions of the holes and slits in the mask placed in front of the *PPAC* during the calibration.

present in the beam cocktail. Therefore, any position uncertainty is dominated by this value. But this measurement was performed as a relative measurement (see Sec. 5.3.2.3) and these systematic uncertainties will not play a role for the final result.

To ensure that the beam spot did not move during the experiment, the mean value, rms value and skewness of the upstream and downstream beam spots were monitored for all runs. This was done while gated on different beam components. As shown in Fig. 5.10 and Fig. 5.11 for ^{102}Cd the spots did not really move and stayed constant. The mean values moved by less than 5 mm which is smaller than the beam spot size and the second and third moment (rms and skewness) also do not show any unexpected jumps or shifts. The same behavior was observed for the other beam components.
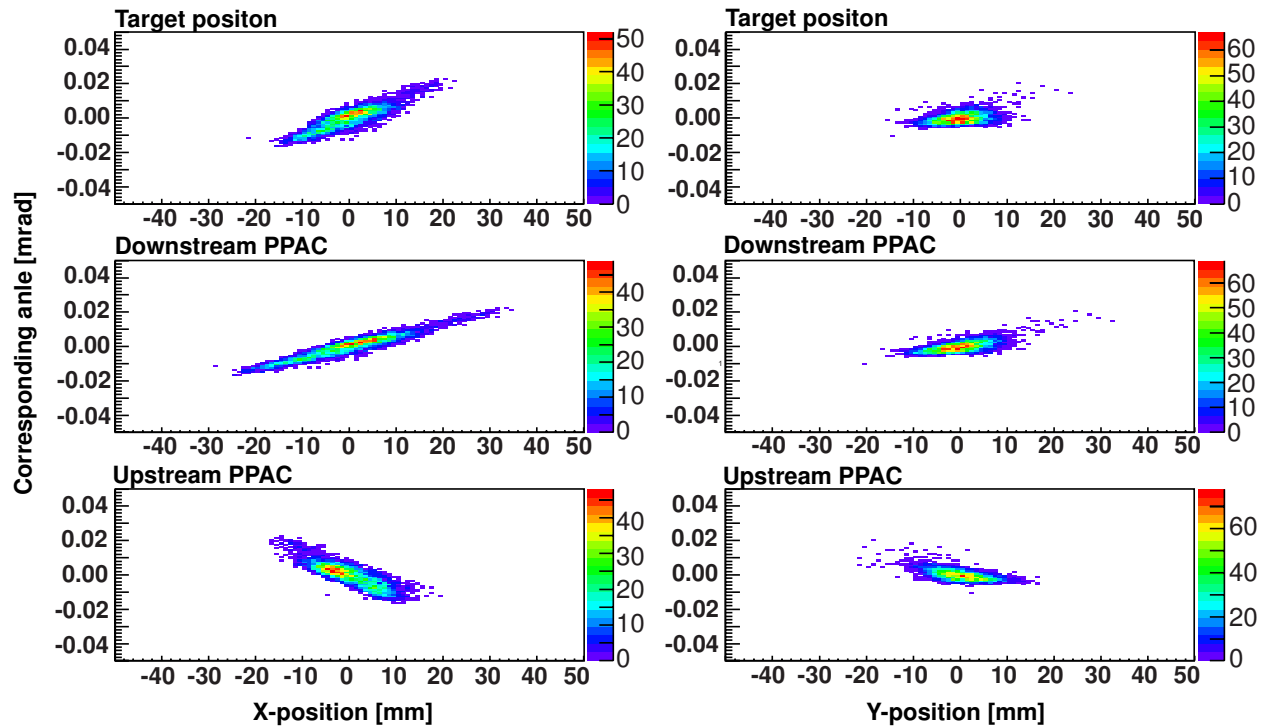
Figure 5.8 Position data taken using the pilot beam and no target. Left column has the x-positions and the corresponding angles. Right column has the y-positions and the corresponding angles. The first row is at the target position, the second at the downstream position and the third at the upstream *PPAC* position.
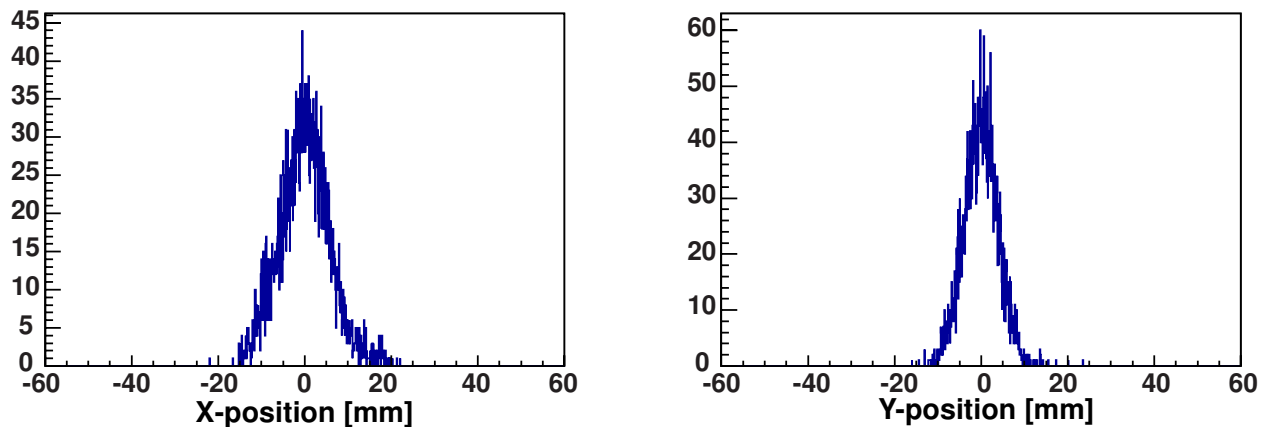
Figure 5.9 X and Y projections of the beam spot at the target position.

5.1.3 Corrections

Because the experiment was running for over 7 days and had high beam intensities, it was necessary to do several re-tunes of the beam and among other thing move the plastic timing
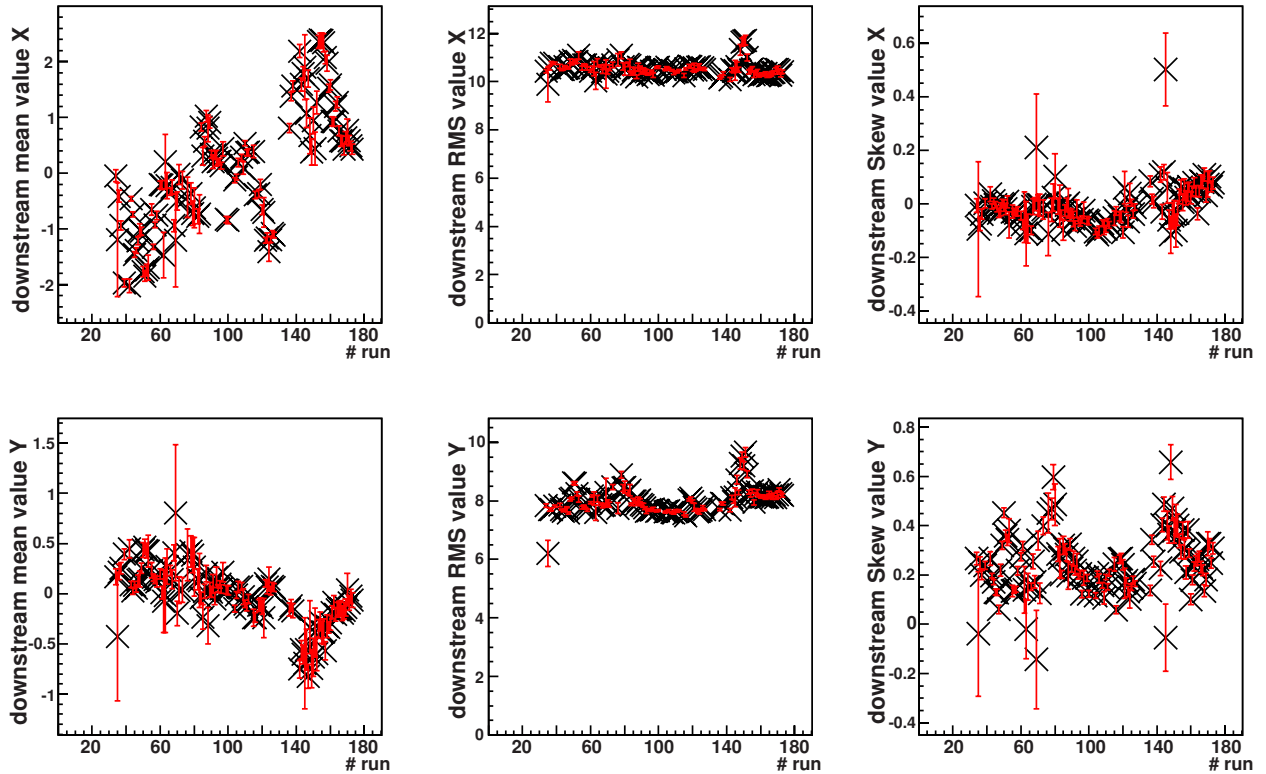
Figure 5.10 Downstream $PPAC$ beam spot position for ^{102}Cd over time.

scintillators (see Sec. 4.1) to use different spots after radiation damage. Due to radiation damage, the plastic scintillators were not able to detected particles with a high efficiency anymore (the detectors were experiencing roughly a rate of nuclei of a little more than 1 kHz). But the affected areas were small and it was possible to move to "unused" spots on the plastic scintillators. This was necessary to keep running with a high efficiency. This also made it necessary to apply corrections in the data analysis to account for small differences due to different spots on the plastic scintillator detectors. Also the re-tunes sometimes changed the secondary beam composition slightly and in combination with the long run time and heavy use of the p-i-n detector, the energy loss measurements of the secondary beam components were also affected. Therefore, this had to be taken into account, too.

All changes to detectors and re-tunes occurred in-between runs so it was possible to look
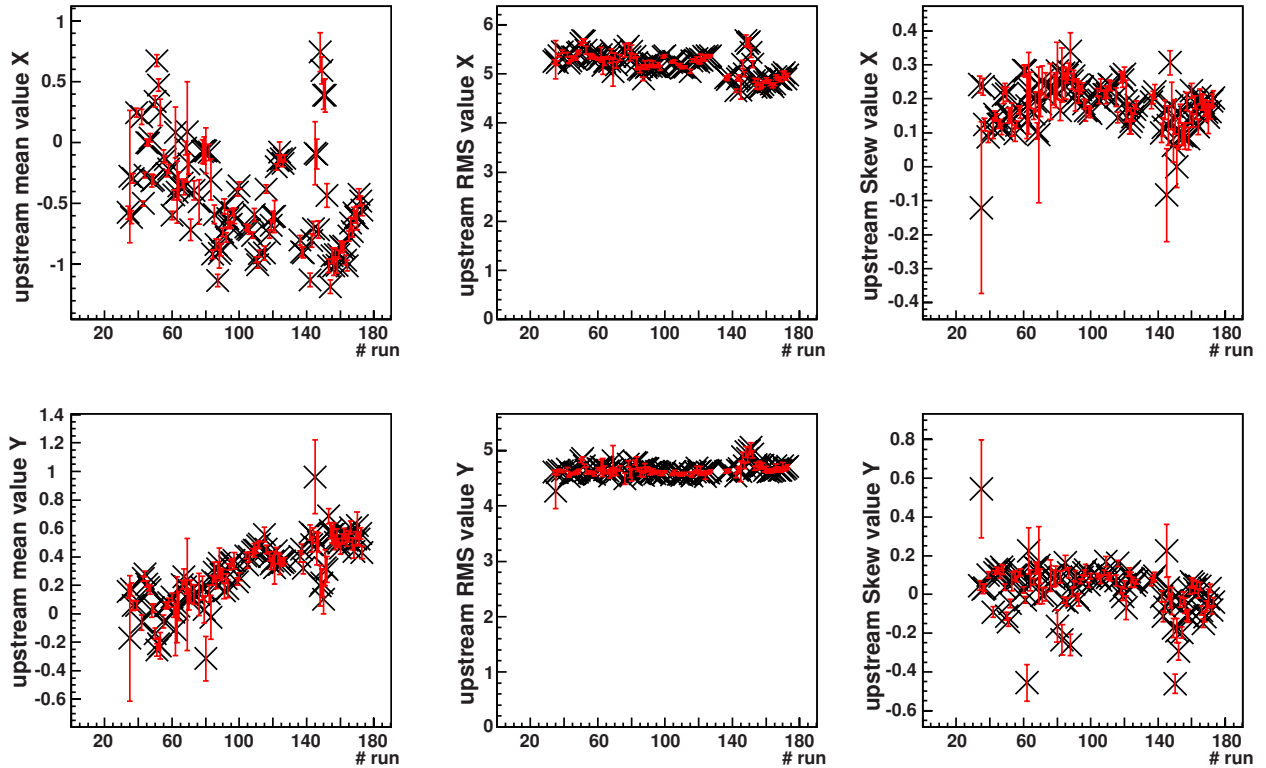
Figure 5.11 Upstream *PPAC* beam spot position for ^{102}Cd over time.

at data run-by-run with no change in the experimental conditions during the runs. For the corrections, *PID* plots (see Sec. 5.2) and gates on the strongest beam component (^{101}Cd) were made for every individual run.

The next step was to gate the variables that needed to be corrected on this strongest beam component. After that the mean values for every 250 entries of the gated variables were retrieved. Those mean values were then used as offsets to correct the variables.

The corrected variables were the timing information from the plastic scintillators at the RF and XFP position and the difference of both. (Only the timing information from the XFP position is used in the analysis because it has the longest time-of-flight information and therefore gave the best resolution for the *Particle Identification*, see Sec. 5.2). The same correction was done for the energy information of the *p-i-n* detector. The effects of the corrections are shown in Fig. 5.12.
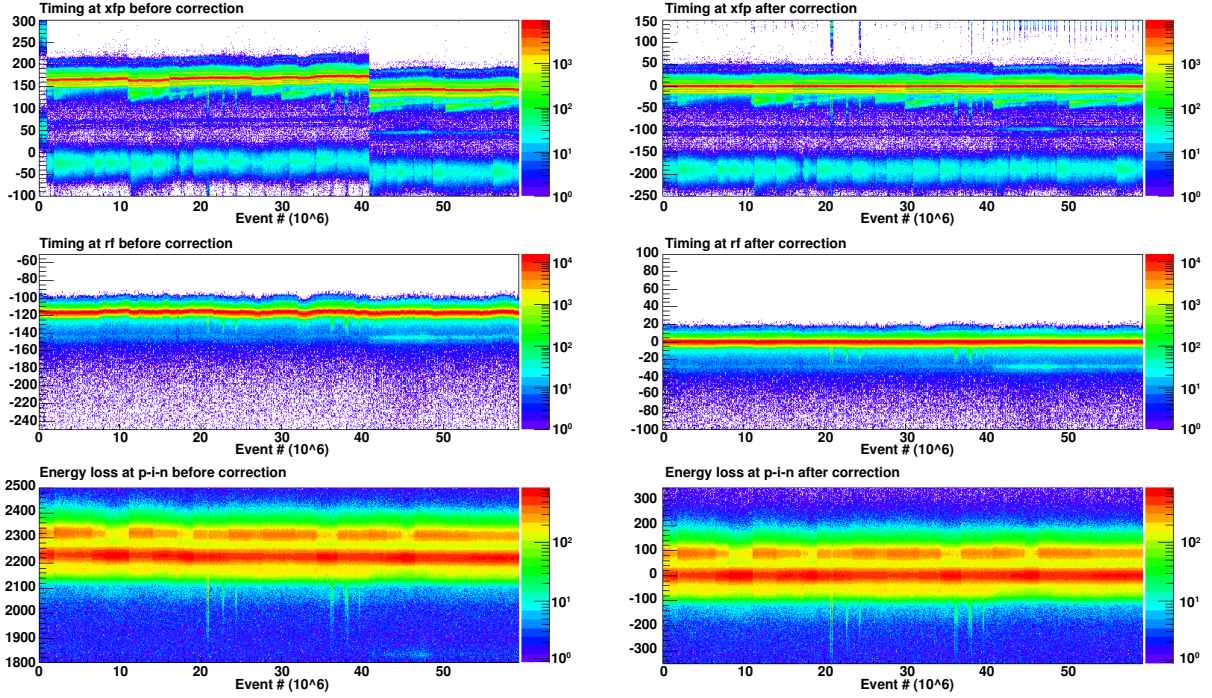
Figure 5.12 Corrections. The left side shows uncorrected data for all events that were recorded during the experiment and the right side shows the same data but with the run-by-run corrections applied as explained in the text.

5.2 Particle Identification

For this experiment, it was of course important to identify the incoming nuclei. It was done with an incoming *Particle Identification* (*PID*) plot. Identification of the different beam components is achieved by looking at an energy loss vs. *time-of-flight* (*tof*) plot. The energy loss is proportional to the Z^2 value of the isotope (see Eq. 4.4) and the *tof* is proportional to the $\frac{A}{q}$ value (mass over charge).

5.2.1 PID

The *tof* was measured between the XFP scintillator and the *Phoswich* detector. This was used because it provided the longest *tof* and with that the best resolution. It would have been preferable to use the difference between the RF and XFP timing information because it

would have eliminated the common *Phoswich* but the *tof* was too short and the resolution not good enough. The energy loss was measured with the *p-i-n* detector. In Fig. 5.13 the *PID* plot is shown. The different beam components are marked with the incoming gates in red. The assignment of the different species was confirmed by the observation of characteristic γ rays in *CAESAR* found at [6]. It is also clearly visible that the separation between the different beam components is not perfect. This is taken into account in the analysis (e.g. for the total number of particles detected, see two dimensional fits in Sec. 5.2.2).
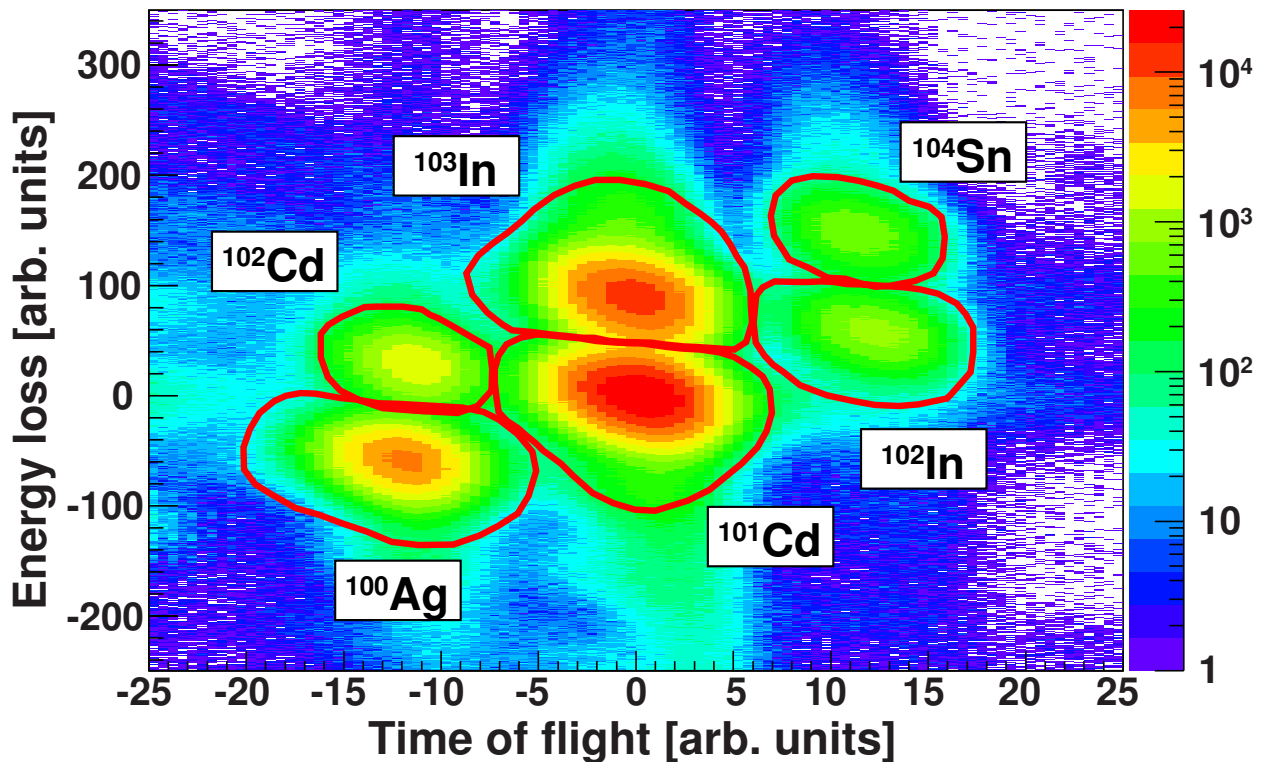
Figure 5.13 *Particle Identification* spectrum for the neutron-deficient projectile beam passing through the Au target. The energy loss measured in the *p-i-n* detector is plotted versus the ion's flight time. ^{104}Sn and ^{102}Cd can be clearly identified. The red lines show the incoming gates. See text for details.

5.2.2 Trigger Modes and Contamination

Three different trigger modes were used during the experiment. The first and most common was a coincidence trigger. The coincidence condition required a detected particle in the *Phoswich* and a detected γ ray in *CAESAR* within a time window of 600 ns. The second one was a downscaled particle singles trigger. For very 50th event that detected a particle (independent of whether or not it was in coincidence with a γ ray) a trigger was issued. This condition was needed to calculate the total number of incoming particles which is needed for the $B(E2 \uparrow)$ calculation (see Sec. 5.6). The downscaler of 50 was necessary so that the data acquisition would mainly record coincidence events which are the main part of this experiment and far less common. The last trigger condition required that the first two occurred at the same time. After a careful analysis, it was noticed that trigger condition two (downscaled particle singles) caused a time offset in the *tof* compared to the other two trigger conditions. It was an offset of 3.5 ns. This offset was applied as a correction to the events with this trigger condition.

Something else that had to be taken into account is the contamination of neighboring beam components entering into the individual incoming gates. To account for this, two dimensional fits were done. The two dimensional *PID* plot was taken and all 6 beam components were fitted at the same time (see Fig. 5.14). For every component a two dimensional Gaussian was used. With the functions obtained from the fits it was possible to calculate how many particles in an incoming gate came from neighboring beam components. The corrections for the two beam components of interest, ^{104}Sn and ^{102}Cd, were smaller than 2.5%. They were calculated with the functions obtained from the fits of the downscaled particle singles trigger *PID* plot. This trigger condition had to be used because the number of incoming ions was

counted with this plot. All the entries in this plot in an incoming gate have to be multiplied by 50 which gives the total number of incoming ions for this gate. In Fig. 5.14 the *PID* plot just for downscaled particle singles is shown and the two dimensional Gaussian fits are shown superimposed.
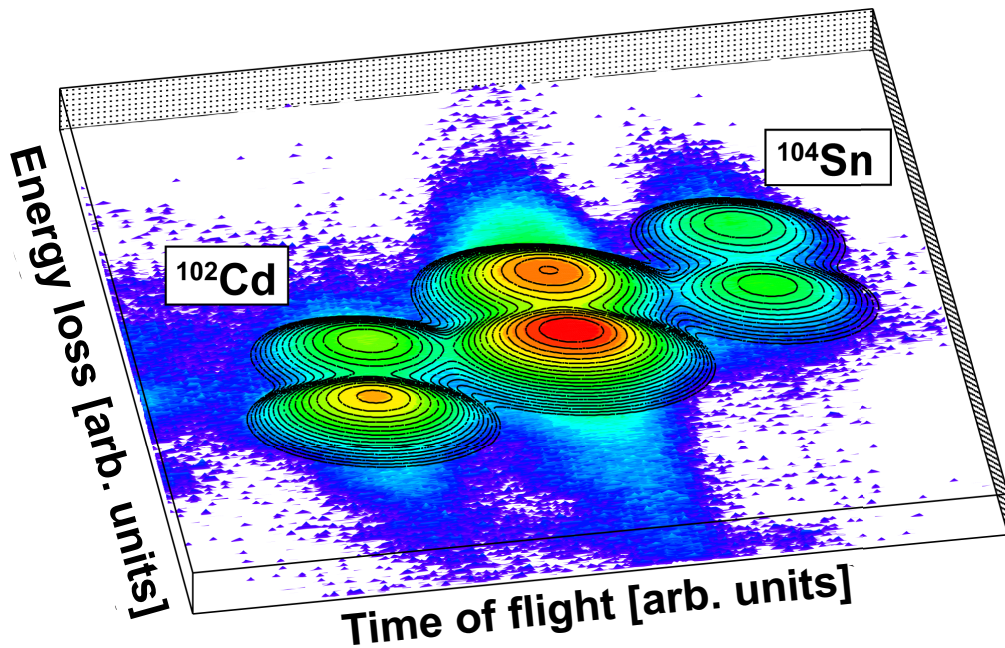
Figure 5.14 *PID* plot for downscaled single events with two dimensional Gaussian fits (black lines). See text for more details.

5.3 γ-ray Spectra

In this section, it will be described how the γ-ray spectra, on which the results of this experiment are based, were created. All γ-ray spectra are so-called singles spectra. That means that no addback was used to create them. Every detector was taken by itself without adding back events that scattered into neighboring detectors (Compton scattering for example). The trigger condition was the particle-γ ray coincidence trigger condition.

5.3.1 Velocity Determination

It was important to find the right $\beta = \frac{v}{c}$ to do the Doppler correction for the γ-ray spectra. This was done by dividing the array into a forward and backward part (5 forward rings and 5 backward rings) for ^{104}Sn and for the higher statistics ^{102}Cd case into 2 forward parts (2 and 3 rings) and one backward part. Then the β for the Doppler correction was systematically changed while tracking the position of a γ-ray peak which is characteristic for the incoming nucleus. The positions of the γ-ray peaks were tracked separately for the forward and backward parts of the array. For the right β the positions of the γ-ray peaks of the forward and backward parts have to line up. In Fig. 5.15 and Fig. 5.16 the results of this analysis are shown. For ^{104}Sn the red points mark the γ-ray peak position for the forward part of $CAESAR$, the blue the backward part and the pink is for all of $CAESAR$. The yellow is the $FWHM$ of the simple Gaussian fit for all of $CAESAR$. For ^{102}Cd the red points mark the most forward part of $CAESAR$, the green the second forward part, the blue the backward part and the pink and yellow is the same as for ^{104}Sn. It is clear that $\beta = 0.345$ is the right β for ^{104}Sn and $\beta = 0.335$ the right β for ^{102}Cd, because for those β values the γ-ray peaks of the forward and backward parts of the array line up the best while simultaneously having a small FWHM. Those results are consistent with the theoretical energy loss calculations performed with $LISE++$ [18] that gave a before, mid and after target β of 0.382, 0.361 and 0.336 for ^{104}Sn and 0.375, 0.354, 0.328 for ^{102}Cd.

5.3.2 Gating

Several gates are applied to the data to clean up the γ-ray spectra. The first gate applied is a low-energy cut. It is necessary due to a lot of low-energy counts coming from atomic
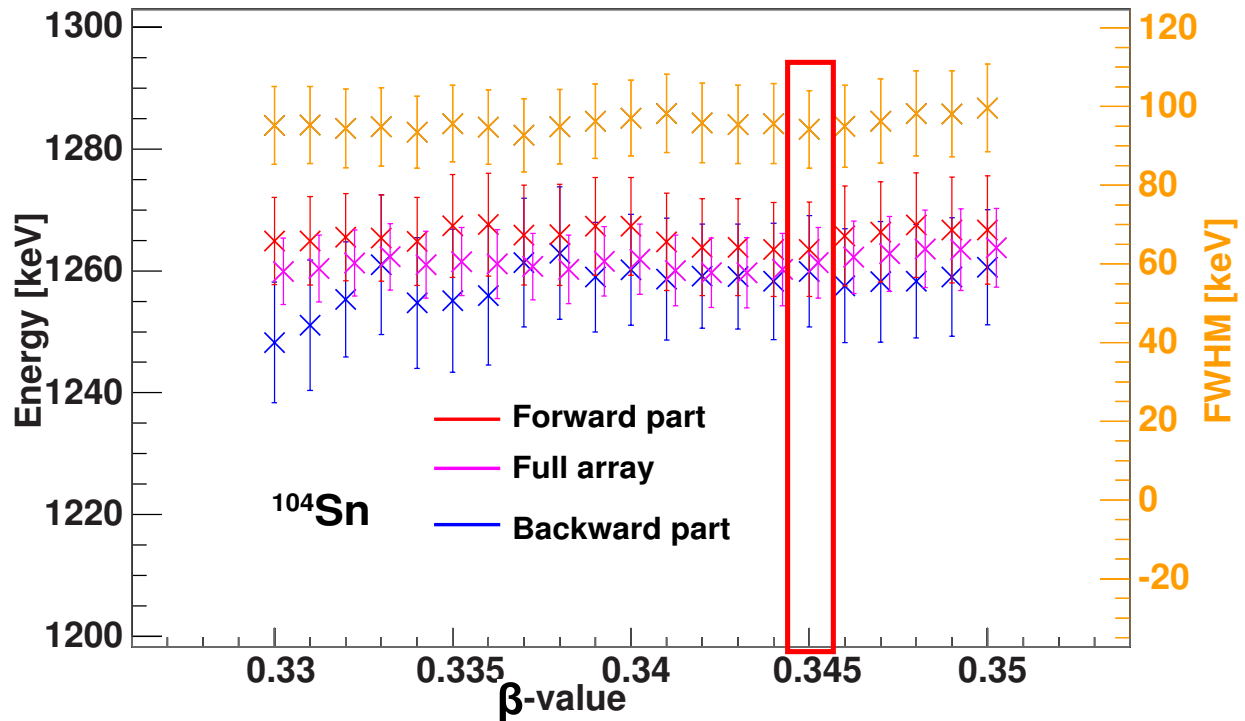
Figure 5.15 Plot to find the right β for the Doppler correction of ^{104}Sn. The γ-ray energy is at 1260 keV [6]. For details see the text.

background. This background consist mainly of four components [67]:

- K and L shell X-rays from ionized gold target atoms,

- radiative electron capture (REC) of the gold target electrons into the projectile K and/or L shells,

- primary Bremsstrahlung (PB) from target electrons produced by the collisions with the projectile,

- secondary Bremsstrahlung (SEB) from energetic knock-out electrons re-scattering in the target and/or the surrounding material.
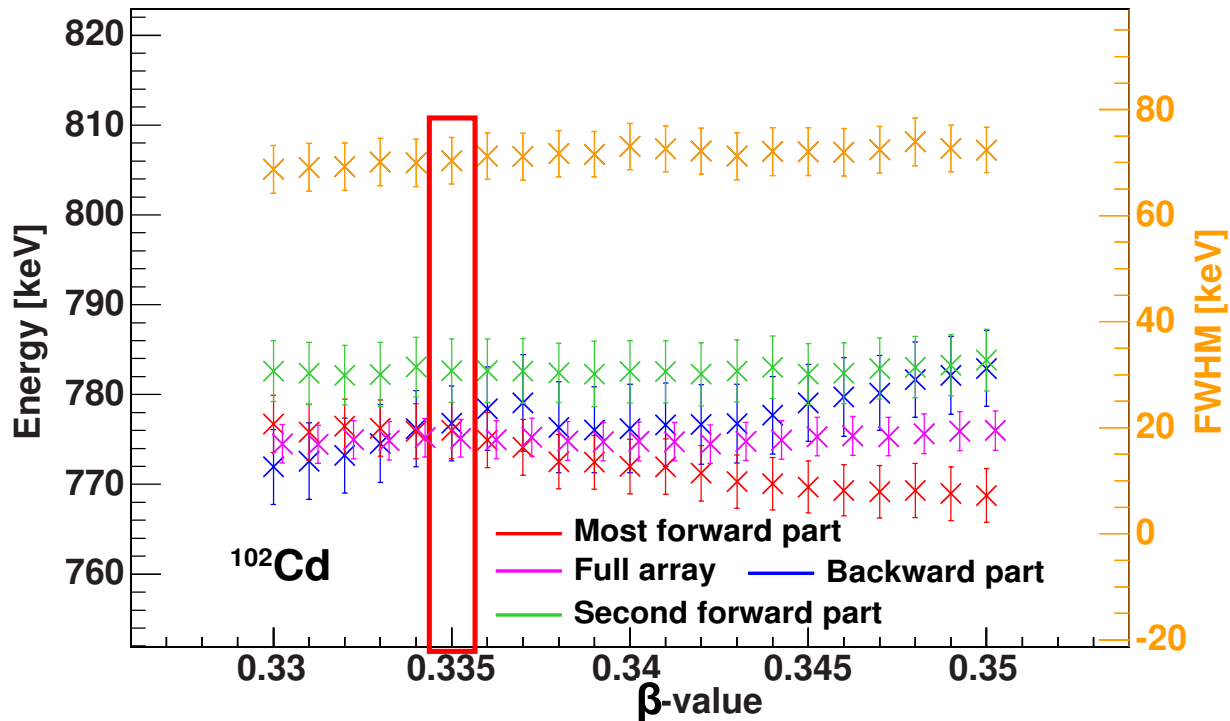
Figure 5.16 Plot to find the right β for the Doppler correction of ^{102}Cd. The γ-ray energy is at 777 keV [6]. For details see the text.

To avoid being dominated by this background all energies below 100 keV in the lab frame were cut out. The other gates that were used are explained below.

5.3.2.1 Prompt γ-ray Timing

Another very important gate was the prompt γ-ray time-cut. This cut eliminated random coincidences, especially of γ rays that were produced by nuclei hitting the *Phoswich* detector that was placed 0.96m downstream of the target. Fig. 5.17 shows a plot of lab energy versus timing for all events with only 1 hit in *CAESAR* (no incoming gate). Only the one hit events are shown. The cutoff at 100 keV is visible and so are two main features. The main feature at time zero is from γ rays produced at the target position and the second feature with roughly a 10 ns delay (the x-axis has 250 ps per channel) is from delayed reactions

e.g. in the *Phoswich*. The plot also clearly shows the two horizontal background lines from ^{40}K with 1460.8 keV and the other one from ^{208}Tl with 2614.5 keV stemming from random coincidences with room background. The red line indicates the gate region which was used to only allow *prompt* γ rays in the analysis. In this plot it might look like there are more *off-prompt* γ rays than *prompt* ones but that is because of the choice to only show events with 1 γ ray detected in *CAESAR*. It should also be noticed that the random events a bit further away from the prompt events are not evenly distributed. Therefore it was decided not to perform a random background subtraction.
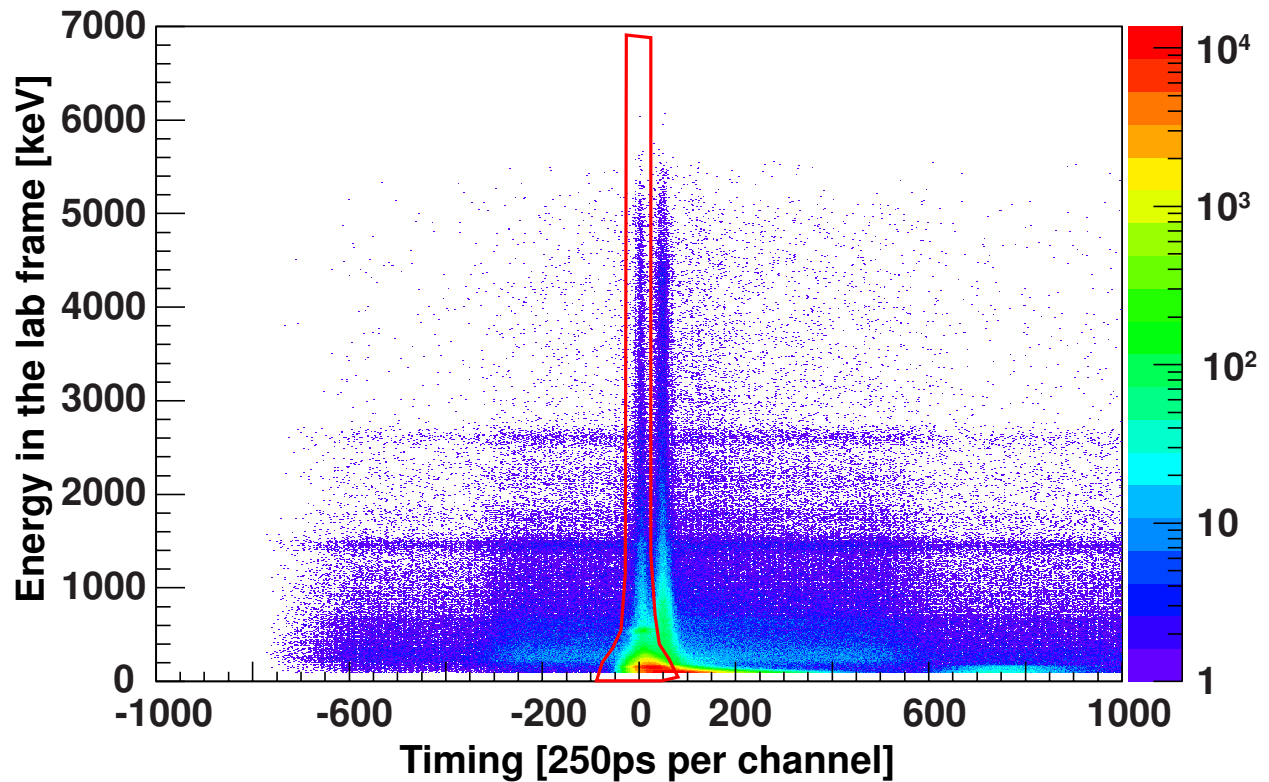
Figure 5.17 Plot to show the prompt γ-ray time gate (red). Only 1 hit events in *CAESAR* are displayed. The two main features from *prompt* and *off-prompt* γ rays are clearly visible as well as the two horizontal background lines at 1461 keV and 2615 keV. For details see the text.

5.3.2.2 Particle Scattering Angle Cuts

A "safe" angle cut was employed, too (see Sec. 3.2). As described, this is necessary to make sure there are no nuclear contributions to the Coulomb excitation cross section by focusing on events with large impact parameters, corresponding to small scattering angles. Calculations for the maximum safe angle were performed with the Eq. 3.9 using $b_{\min}$ from Eq. 3.11. In SI units, this formula is expressed as follows (exactly the same as Eq. 3.9):

$$b_{\min} = \left(\frac{Z_p Z_t \alpha \hbar c}{\lambda \beta^2 m_{nuc} c^2 \left(\frac{A_p A_t}{A_p + A_t} \right)} \right) cot \left(\frac{\theta_{cm}^{max}}{2} \right), \tag{5.1}$$

with $m_{nuc}c^2 = 931.494$ MeV the average bound nucleon mass, $\alpha = 0.007297$ the fine structure constant, $\hbar c = 197.327$ MeV, $Z_{p/t}$ the projectile/target proton number and $A_{p/t}$ the projectile/target mass number.

The maximum scattering angle was calculated in the center-of-mass frame for the two beam species of interest, ^{104}Sn and ^{102}Cd, with the assumption that the reaction happened mid target ($\beta = 0.361$, $\beta = 0.354$, respectively) as well as at the front of the target ($\beta = 0.382$, $\beta = 0.375$). The conversion to lab frame angles was performed with $LISE++$ [18]. This resulted in the following maximum scattering angles in the lab frame: $3.126°$ and $2.756°$ for ^{104}Sn as well as $3.206°$ and $2.821°$ for ^{102}Cd. To be conservative, it was decided to restrict the data to an even "safer" (meaning larger impact parameter) maximum scattering angle, namely 45 mrad which corresponds to $2.578°$. This was done for ^{104}Sn and ^{102}Cd. In Fig. 5.18, the distribution of all scattering angles for all events of our two species of interest are plotted. The different scattering angle cutoffs are shown, too. The red line corresponds to the mid-target β, the green line to the front of the target β and the blue line marks the actual cut-off used.
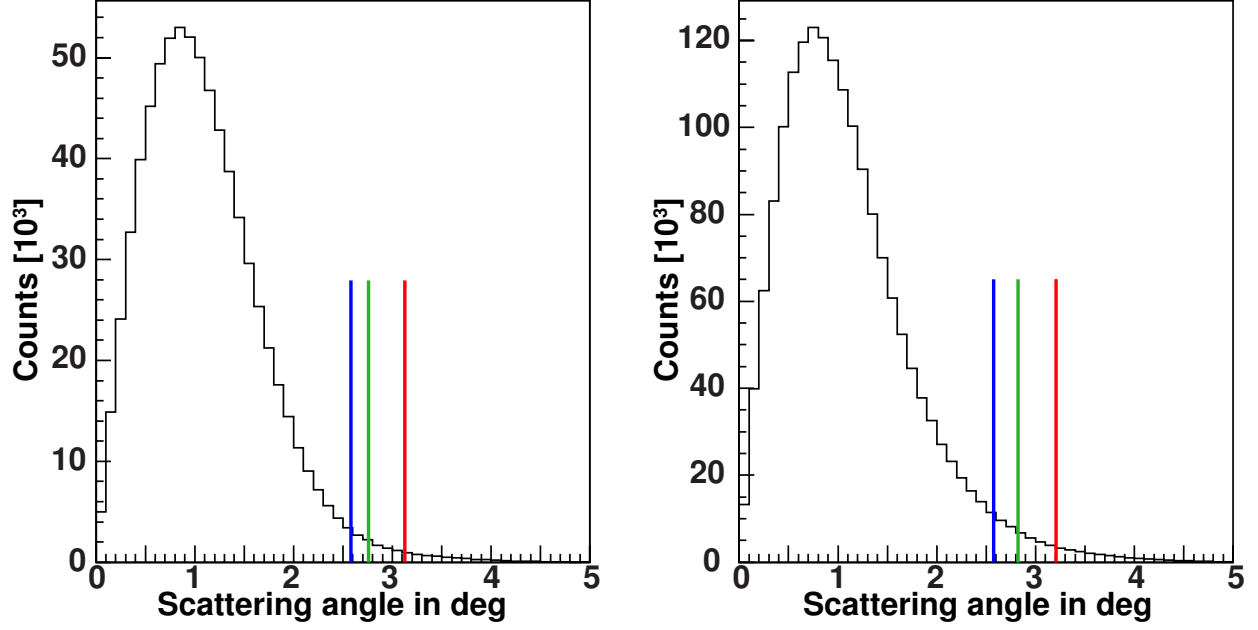
Figure 5.18 Scattering angle distribution for ^{104}Sn (left) and ^{102}Cd (right). Blue line: "safe" angle which was used, green line: "safe" angle for beginning of the target, red line: "safe" angle for middle of the target.

The measured scattering angles were determined the following way. The distance between the target and the downstream $PPAC$ was measured to be 583 mm. As the distance and the x and y position in the $PPAC$ are known, this makes it easy to calculate the scattering angle. With the $PPAC$ position information d, the distance from the center of the $PPAC$ to where the nucleus hit the $PPAC$, can be calculated in millimeters:

$$d = \sqrt{x^2 + y^2}. \tag{5.2}$$

The scattering angle θ has therefore the following dependence:

$$\theta = atan\left(\frac{d}{583}\right). \tag{5.3}$$

For every species, different offsets had to be used (see Sec. 5.1.2). The offsets were chosen

in a way that made sure that all coincidence events together have a mean x and y position of zero on the *PPAC*. This lead to a difference in offsets between ^{104}Sn and ^{102}Cd of 12 mm in total (7.1 mm in x and 9.6 mm in y). The centered downstream *PPAC* plots can be seen in Fig. 5.19.
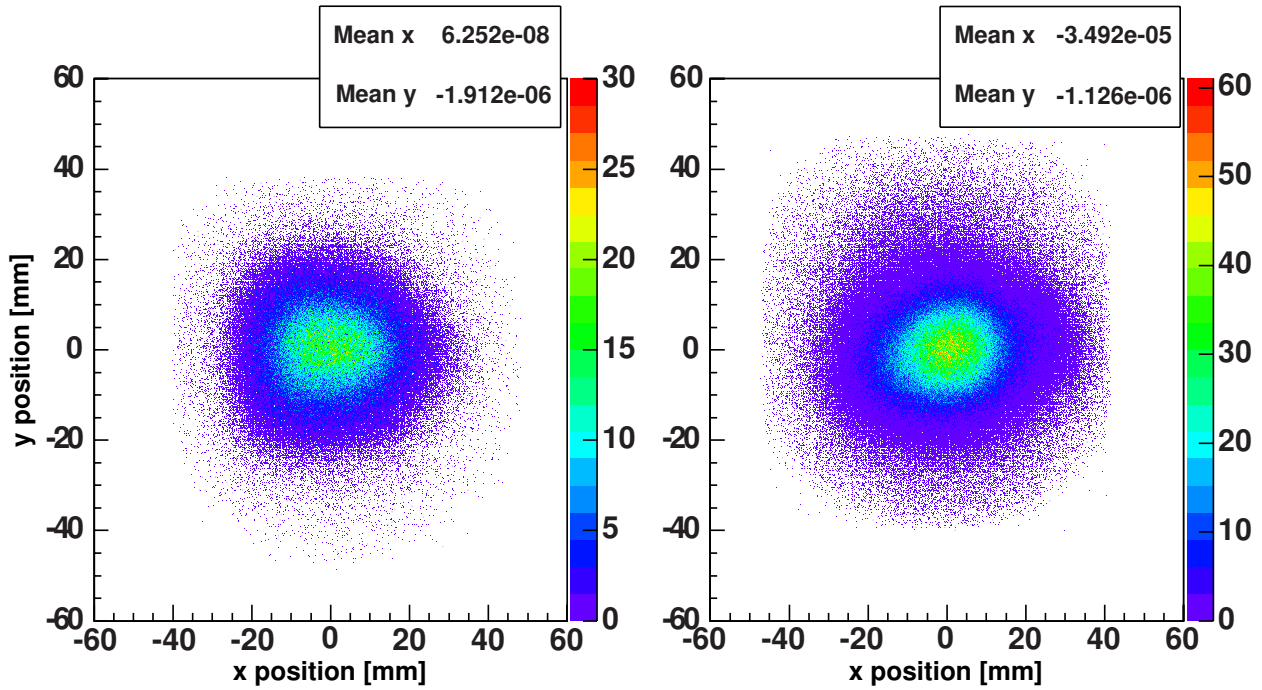
Figure 5.19 Downstream *PPAC* gated on coincidence events, centered and gated on ^{104}Sn (left) and ^{102}Cd (right).

LISE++ [18] was used to calculated the angular straggling and it is less than $\sigma = 0.4°$. This was then used as an input for a Monte Carlo Simulation to estimate how big the effect of straggling would be on the angle cuts. The straggling effect makes it appear that an event has an acceptable angle (below cutoff) where in fact it does not (and vice verca). This was done for both cases of interest for the singles scattering angle spectra but only the higher statistics case ^{102}Cd is displayed here. The downscaled singles trigger condition was applied to avoid a bias towards elastic or inelastic scattering processes. An input distribution was chosen that would reproduce the measured angular distribution after folding it with the

straggling distribution. The straggling distribution is a Gaussian distribution with $\sigma = 0.4°$ from which a random straggling angle was taken and then this angle was randomly added in the full 3D space to the initial angle. For both ^{104}Sn and ^{102}Cd it was determined that for all angles larger than $1.5°$, about 0.7-1.5% of the counts originate from larger scattering angles that fulfill the maximum angle cut since they straggled to smaller angles (blue) and about 3-4% of the events that would have fulfilled the maximum angle cut without angular straggling are lost (green). The results for ^{102}Cd can be seen in Fig. 5.20.
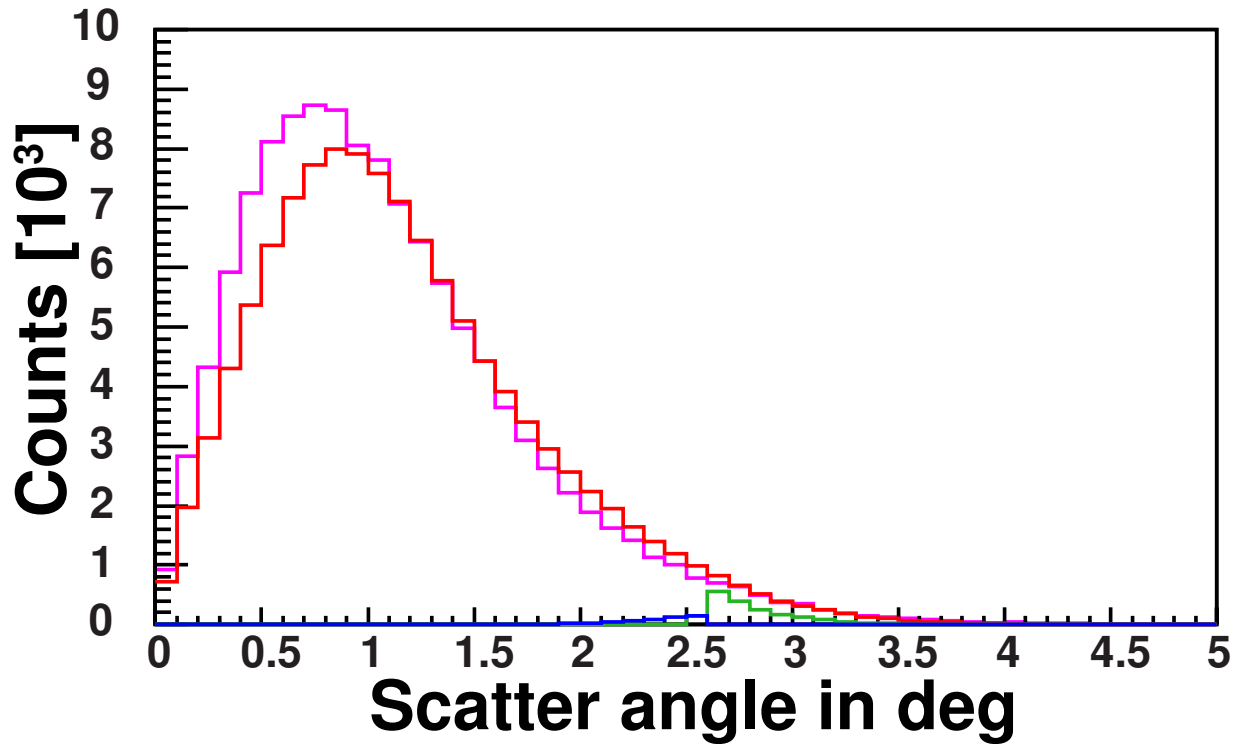
Figure 5.20 Effect of straggling. Pink is the measured distribution with downscaled singles trigger condition. Red is the result of the whole Monte Carlo simulation. Blue are the events that fulfilled the scattering angle cut condition but started with angles bigger and green are the events that did not fulfill the angle cut condition but started with angles smaller.

5.3.2.3 Multiplicities

Very early in the analysis the problem surfaced that even with a prompt γ-ray time gate and incoming *PID* gate it was not possible to see any γ-ray peaks unless the spectrum was restricted to low *CAESAR* detector multiplicities. Multiplicities are determined by the number of detectors hit in *CAESAR* during one event. When a prompt γ-ray time gate is applied then the multiplicity takes only γ rays into account that lie in the gate. One problem with this setup was the *PID* resolution of the *Phoswich*. The resolution was not good enough to use the detector for particle identification after the reactions at the target. This is one of the main reasons why no peaks were visible unless the analysis was restricted to low multiplicities. An investigation into this matter revealed that events were present with huge multiplicities (up to 60 hit detectors in *CAESAR* per event). Those high multiplicity events contribute hugely to the background and obscured any peak. The source of those high-multiplicity events was determined. It is now clear that they come from very violent reactions in the target such as fragmentation. During those violent reactions, a lot of γ-rays and charged particles, interacting with surrounding matter, are produced and it is likely that one of the light charged particles hits one of the *CAESAR* detectors, causing it to go into overflow (the detected energy was higher than the sensitive range of the electronics).

Looking at the multiplicity distribution for a single run (see Fig. 5.21) clearly shows that events with no detector in overflow (blue) dominate the low-multiplicity range and that the high-multiplicity events are dominated by events where at least one detector went into overflow (orange). This confirms the assumption that the high multiplicity events are connected to violent reactions and charged particles with high energies being detected in some of the detectors.
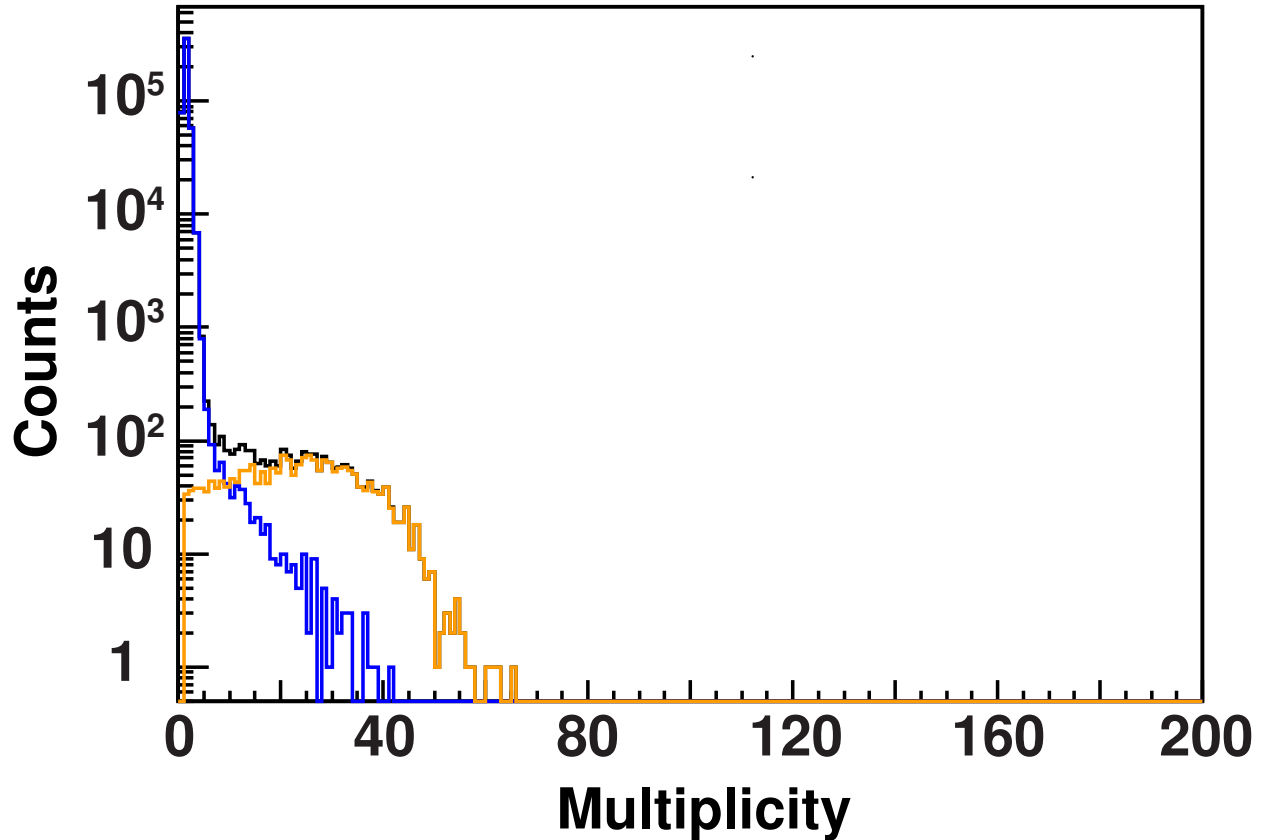
Figure 5.21 *CAESAR* multiplicities for a single run. Black: all events; blue: events with no *CAESAR* detector in overflow; orange: at least one detector in overflow.

To confirm that it actually was fragmentation that occurred, two additional effects were investigated. First, if there is an event with a detector going into overflow, then it mostly happened in the forward rings (0, 1 and 2) of the array, see Fig. 5.22. This shows that those events are heavily forward focused, supporting the hypothesis.

Secondly, the *Phoswich* detector was considered. Even with its rather modest energy (ΔE and E) resolution, it was possible to see trends. Fig. 5.23 shows a trend going to higher multiplicities. On the x-axis is the full energy E displayed and on the y-axis the energy loss $E - \Delta$E. There is a shift to the left along the x-axis visible and almost no shift along the y-axis. This can be explained by the following. On the x-axis is the full energy deposited in the *Phoswich* (integration over the full *PMT* signal) and on the y-axis is E-ΔE shown
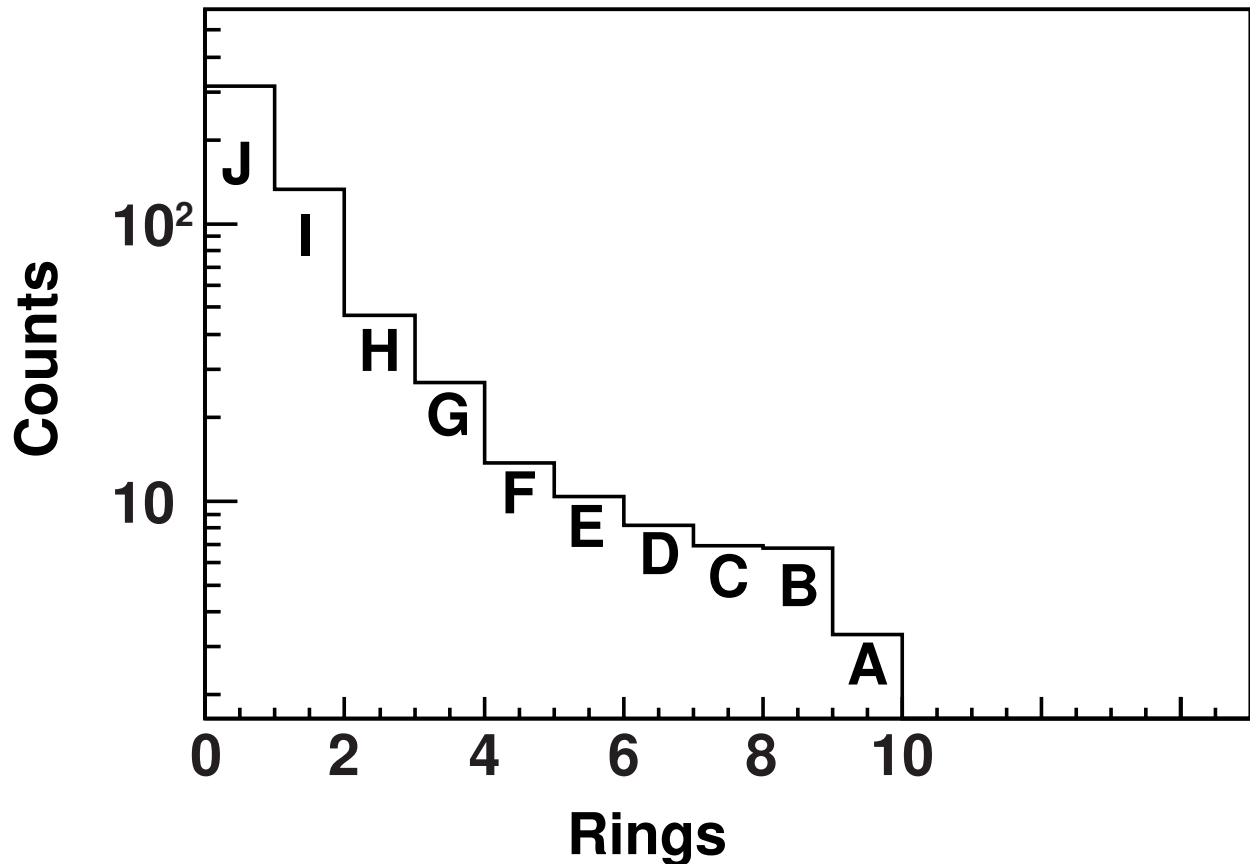
Figure 5.22 Ring distribution of *CAESAR* detectors in overflow. Ring 1 (J) is the most forward ring and 10 (A) the most backward.

(integration with delay over the slow part of the *PMT* signal) which is an indication for the energy loss (for details see Sec. 4.5.3). So this shift means that the particles loose less energy in the thin, first part and almost the same energy is deposited in the thick second part. This confirms that the particles associated with higher multiplicity events have lost protons because the energy loss is proportional to Z^2. So this also supports the theory of violent processes in the target where nucleons are removed from the projectile. Some light, charged particles hit *CAESAR* and surroundings and some lighter, projectile-like residues make it into the *Phoswich*. This is the reason why the analysis had to be restricted to small multiplicities and the decision was made to only allow multiplicity 1 events.

This greatly improves the peak-to-background ratio. The majority of the counts belong
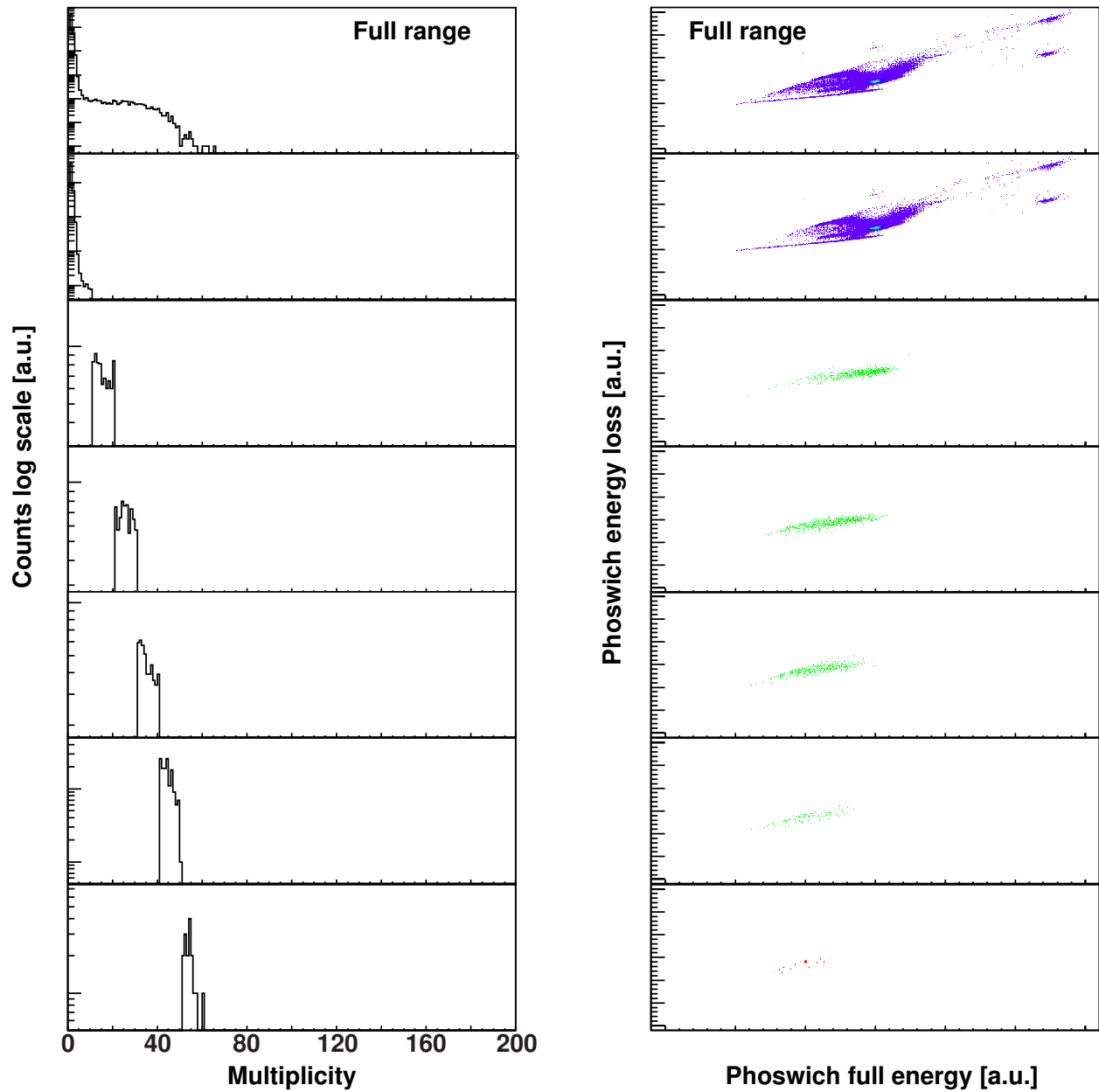
Figure 5.23 Phoswich energies for different multiplicity ranges. On the left side the different multiplicity ranges are shown in steps of 10 and on the right side the corresponding *Phoswich* energies. All detected events were used to generate these plots. The very top panel of both columns has no gates applied, the full multiplicity range is used.

to multiplicity 1 events. Restricting the analysis to multiplicity 1 events and because this setup and data acquisition system are not characterized as well as in previous work at the *S800* spectrograph (see [68], for example), it was not possible to establish reliable absolute

in-beam efficiencies for all detector systems. Therefore, a relative $B(E2 \uparrow)$ measurement was done where most absolute efficiencies cancel out. The measurement was done relative to the well-known $B(E2 \uparrow)$ value of ^{102}Cd [2, 43]. ^{102}Cd was present in the beam cocktail with a higher intensity than ^{104}Sn and provided good statistics for a relative measurement (see Sec. 5.2 and 5.5).

5.3.3 Spectra

With all the gates applied as described in Sec. 5.3.2, the in-beam γ-ray spectra were created. As mentioned before, transitions in ^{104}Sn and ^{102}Cd form the base of the relative $B(E2 \uparrow)$ measurement. The two most important variables that need to be known are the number of γ rays emitted by the nucleus of interest and the total number of incoming ions of this nucleus. To convert the detected γ-ray energy in the lab frame into the Doppler corrected energy in the projectile rest frame, Eq. 4.5 was used.

In Fig. 5.24 are the lab frame (upper panels) and Doppler corrected (lower panels) spectra shown for ^{104}Sn and ^{102}Cd. In the lab frame spectra, the background energy peak at 1461 keV from ^{40}K and the 548 keV + 511 keV peak from Coulomb excitations of the gold target and pair production are clearly visible. In the Doppler corrected spectra, those peaks do not appear anymore but the characteristic energies for the $E2$ transitions in ^{104}Sn and ^{102}Cd respectively [6] are clearly visible.
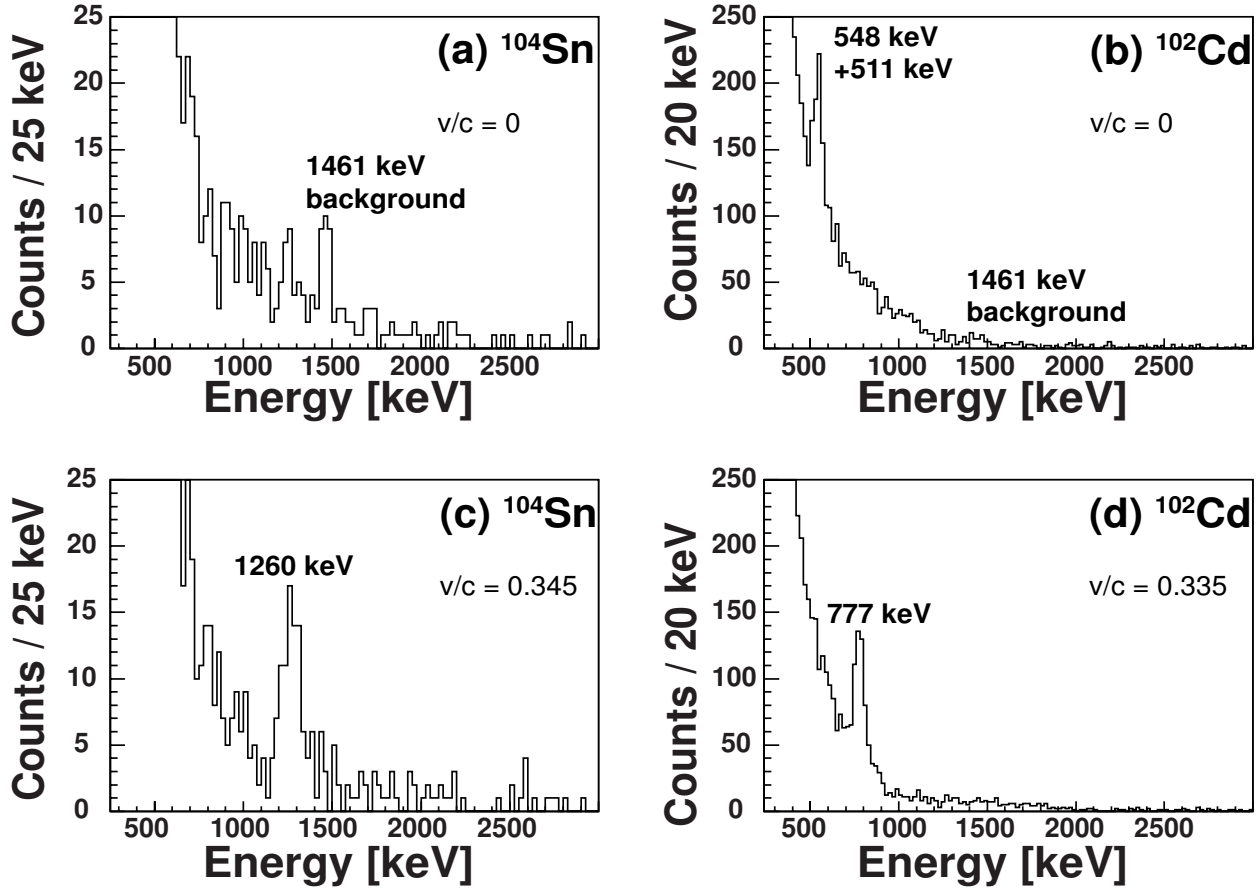
Figure 5.24 Lab frame (upper panels) and Doppler corrected (projectile frame, lower panels) energy spectra for ^{104}Sn and ^{102}Cd, respectively. Characteristic energies are indicated. For more details see text.

5.4 Geant4 Simulations

To determine the total number of emitted γ rays, a simulation was used to take into account geometry, in-beam efficiencies, absorptions, angular distributions and other experimental circumstances. A *Geant4* simulation written by T. Baugher and G.F. Grinyer was implemented to do exactly this (see Sec. 7 and [63]).

For the simulations to work properly, two files had to be prepared. The first was a description of the low-energy threshold for every detector and the second one contained energy resolution functions for each detector.

To obtain a description of the low-energy threshold, the low-energy part of a ^{137}Cs high-activity source spectrum was fitted with half a Gaussian curve. This was done for every detector in *CAESAR* separately. The received fitting parameters sigma (σ) and mean (μ) were used to model the low-energy part of the simulated spectra. The results of the fits for ring 5 are shown in Fig. 5.25.
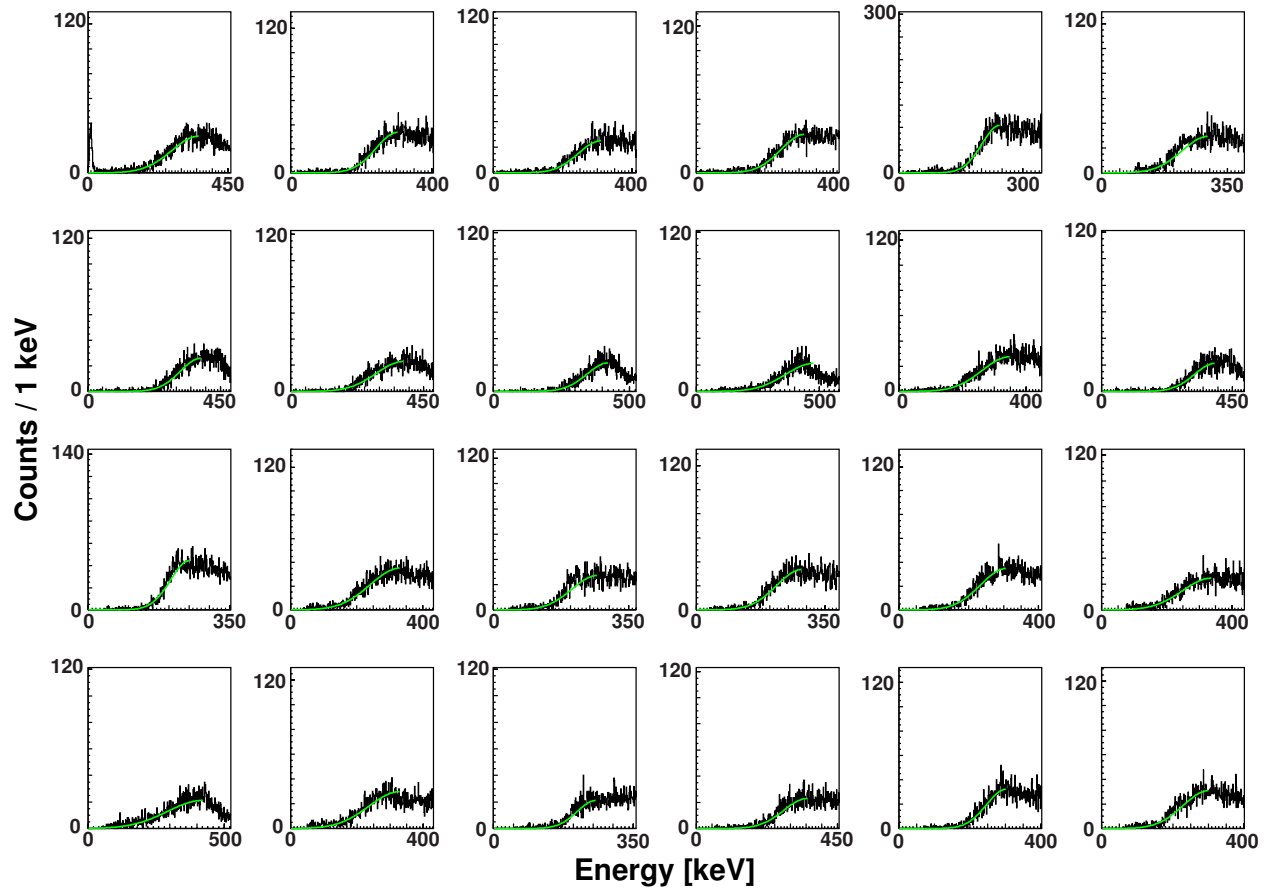
Figure 5.25 Low-energy part for a high-activity ^{137}Cs spectrum for all detectors in ring 5. In green is the half Gaussian fit shown.

To ensure that the low-energy part is not dependent on the energy of the full-energy peak or on the source activity, the spectrum of the high activity ^{137}Cs source was compared to a low activity ^{60}Co source spectrum. After rescaling, there was no visible difference in shape. This confirms that the original ^{137}Cs fits were good and could be used. To see the comparison

for all the detectors in ring 5, see Fig. 5.26.
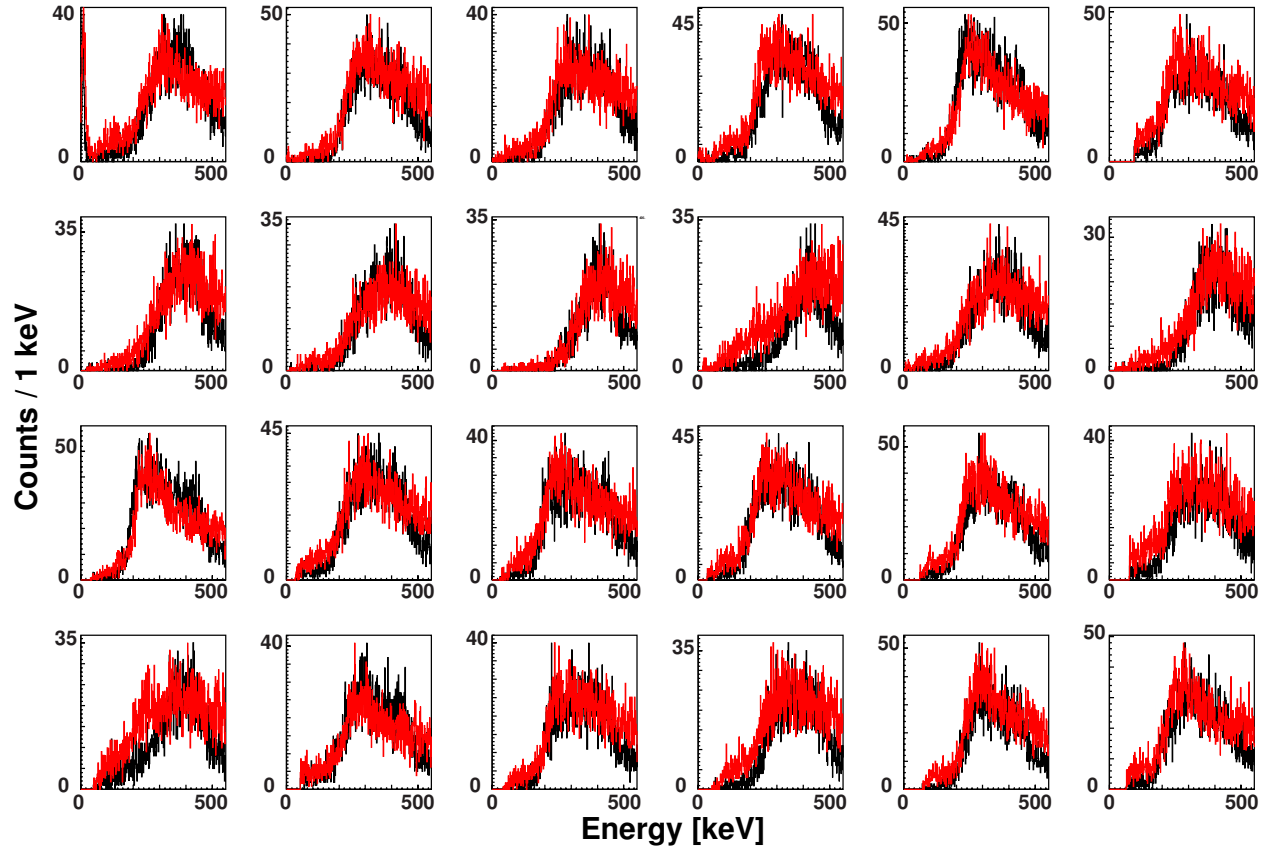
Figure 5.26 Comparison of the low-energy part of a rescaled high activity ^{137}Cs (black) and a low-activity ^{60}Co (red) spectrum.

In a next step, several γ-ray energies from different sources were fitted to gain the function that describes how the *full width at half maximum (FWHM)* changes with energy. The sigma values of the different Gaussian fits at the different energies were fitted with the following formula [21]:

$$\sigma(E) = a \times E^b. \tag{5.4}$$

Again this was done for every detector and the parameters a and b were used to model the *FWHM* behavior in the simulation. Fig.5.27 shows the fits for the detectors in ring 5. The

used sources and their γ-ray energies are listed in Table 5.2

Source	γ-ray energy 1 [keV]	γ-ray energy 2 [keV]
^{22}Na	511	1275.5
^{137}Cs	661.7	–
^{88}Y	898.0	1836.1
^{133}Ba	356.0	–

Table 5.2 Sources and energies used for $\sigma(E)$ fits.
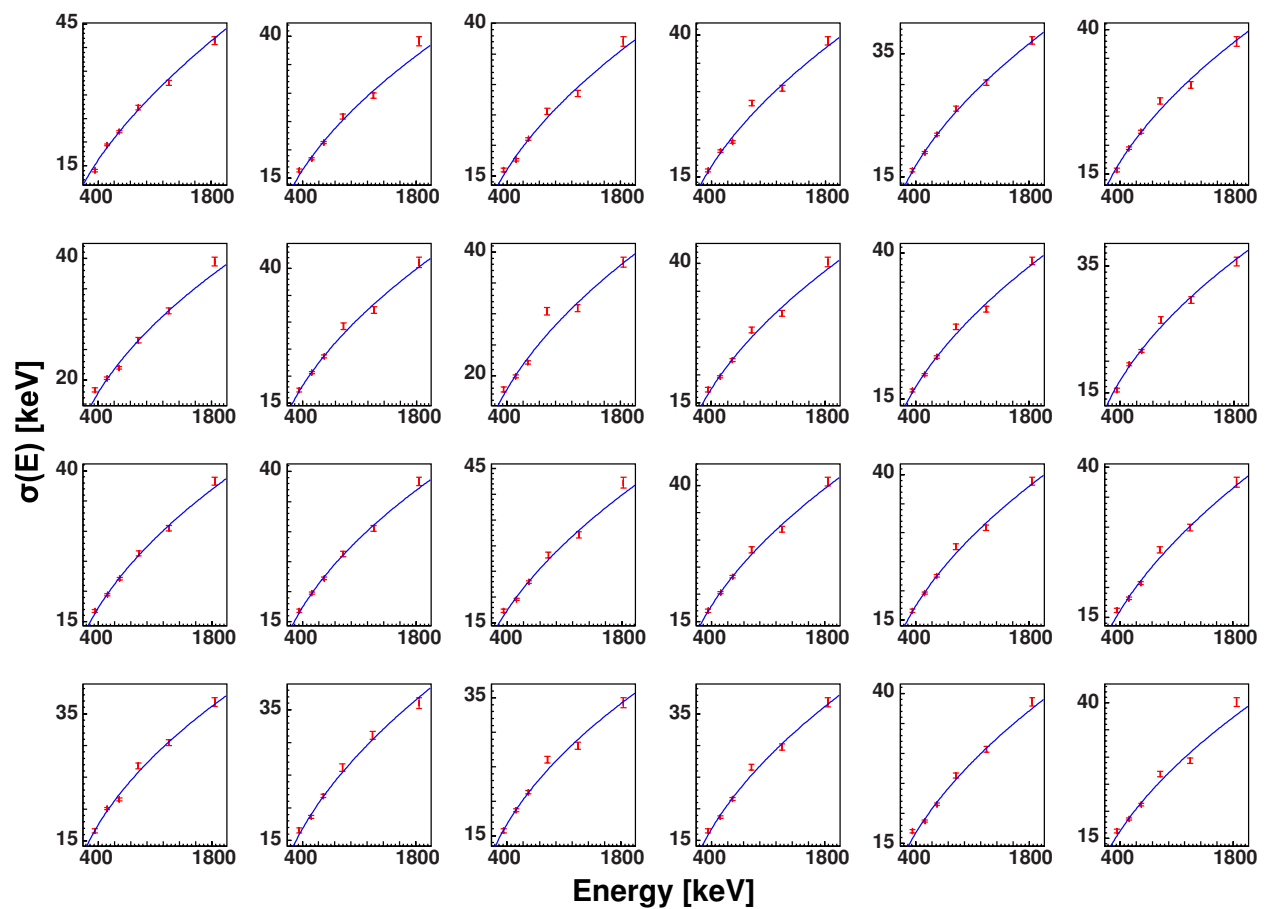
Figure 5.27 Development of $\sigma(E)$ for all detectors in ring 5.

The first test of the *GEANT4* simulation was to simulate source spectra and compare them with recorded source runs. However, during the calibration runs, all the unused sources were stored in a source locker roughly 7m away from *CAESAR* but the locker was not shielded

104

perfectly. Therefore, some of the γ rays from the strongest sources in the source locker were detected in *CAESAR* and slightly contaminated every run. Nevertheless, it was possible to confirm that the simulations reproduce the source spectra well. But because this problem depends on the activity of the source used, we were not able to correct for this effect in a consistent way.

For each source, the total number of γ rays that were expected to be emitted was calculated. First, the activity of the source at the point of the measurement was calculated and then this activity was multiplied with the time the detector system was live (ready for data) during the measurement. This gives the total number of decays that happened during the time of the measurement. Next the simulated spectrum (one energy at a time) was divided by the number of simulated events (normalized), multiplied with the γ ray's specific emission probability (see [6]) and then multiplied with the total number of decays. If necessary multiple energies that belong to the same source were simulated and added together. The last step was to add a scaled background histogram to the simulation. The background histogram was scaled with its data acquisition live time and was needed because the room background is not included in the simulations. The recorded source spectra, on the other hand, have only one gate applied and that is a prompt γ-ray time gate. In Fig.5.28 the results of the comparison are shown. The black histogram is the measured source histogram, the red is the pure scaled simulation and the green is the simulation plus the scaled background.
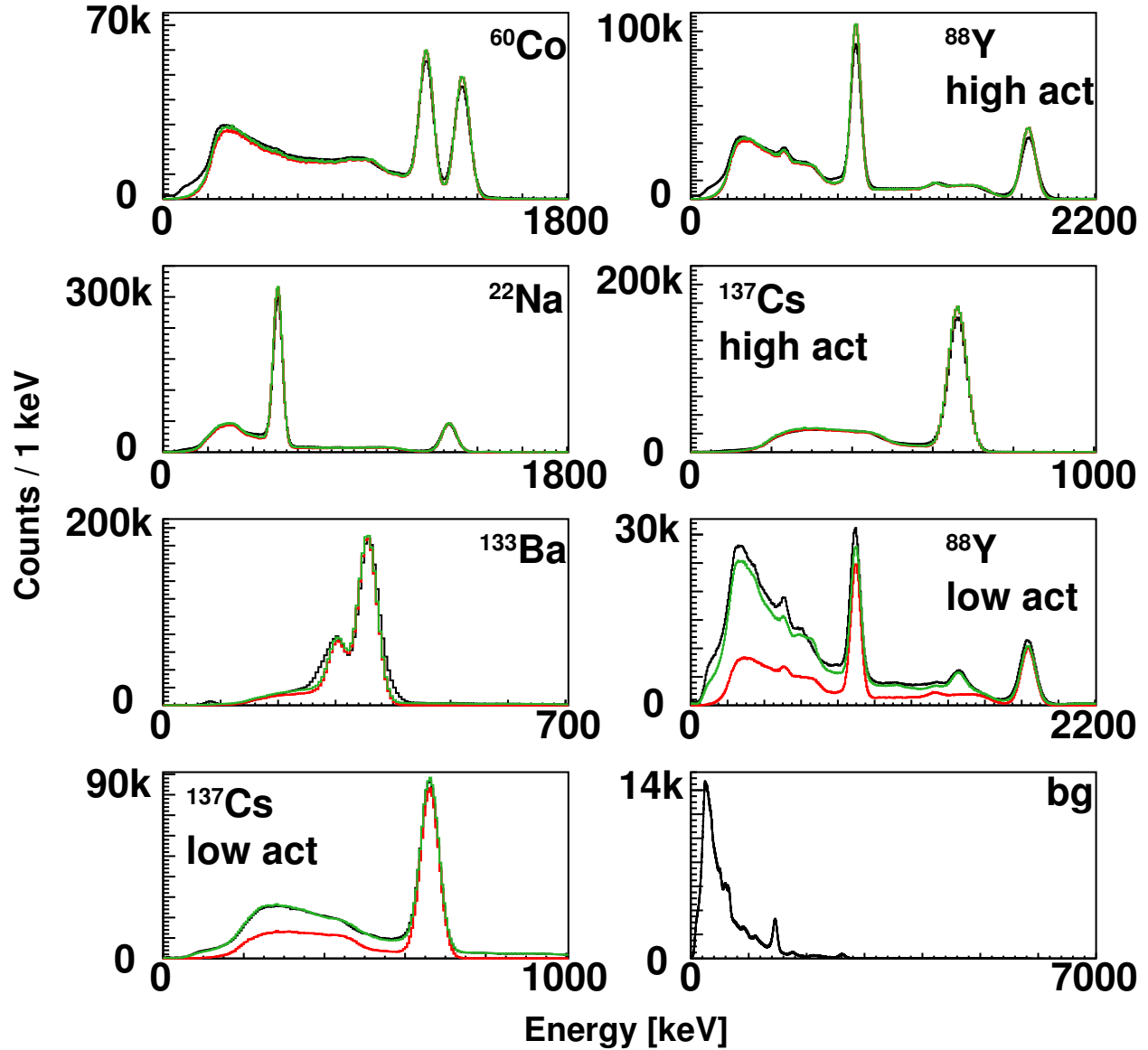
Figure 5.28 Comparison of simulated and measured source spectra. The black histogram is the measured histogram, the red is the pure scaled simulation and the green is the simulation plus a scaled background. The bottom right histogram shows the room background measurement.

5.5   Fits

For the in-beam simulation more information is needed. The kinetic energy of the beam before the target needs to be known (this information was obtained by using recorded $B\rho$ settings and calculating energy losses with *LISE++* [18]) in addition to the momentum

106

spread of the beam (also obtained from recorded settings), the angular distribution of the γ rays which was calculated with the previously mentioned mathematica script [47] and the angular spread of the beam after the target deduced from the data. Ata is the scattering angle in x-direction and Bta the scattering angle in y-direction. Also the thickness, position and dimensions of the target were required. If known, then the lifetime of the excited state was added, too, although the effect is negligible because $CAESAR$ is not sensitive enough to detect changes in γ-ray peak shapes for short lifetimes.

The target used was a gold target of 184 mg/cm^2 thickness and 5×5 cm area, it was placed in the center of $CAESAR$ about 12.8 m downstream from the $RFFS$.

The other settings are displayed in the Table 5.3.

Setting	^{104}Sn	^{102}Cd
Incoming kinetic energy [MeV/nucleon]	76.60	73.37
Incoming momentum spread dp/p	0.41 %	0.41 %
Simulated γ-ray energy [keV]	1260.2	776.6
Lifetime [ps]	–	5.12
Angular distribution a0	1.0	1.0
Angular distribution a2	-0.4690	-0.5710
Angular distribution a4	-0.1137	-0.1740
Sigma Ata [rad]	0.01710	0.01676
Sigma Bta [rad]	0.01292	0.01239

Table 5.3 Input settings used for the in-beam $GEANT4$ simulations.

The simulation was tested and in Fig. 5.29, 5.30 and 5.31 it is shown that the input settings for ^{104}Sn are reproduced by the simulation. The simulation may be improved by getting the energy loss closer to the energy loss calculated by $LISE++$. The energy loss calculations done by $LISE++$ are based on a model that was specifically tuned for the energy region of the nuclei that are produced at the $NSCL$. $GEANT4$ on the other hand uses a different model that is not necessarily optimized for this energy region.

With the in-beam simulation tested, it can be used to fit the ^{104}Sn and ^{102}Cd spectra to

extract the number of detected γ rays.
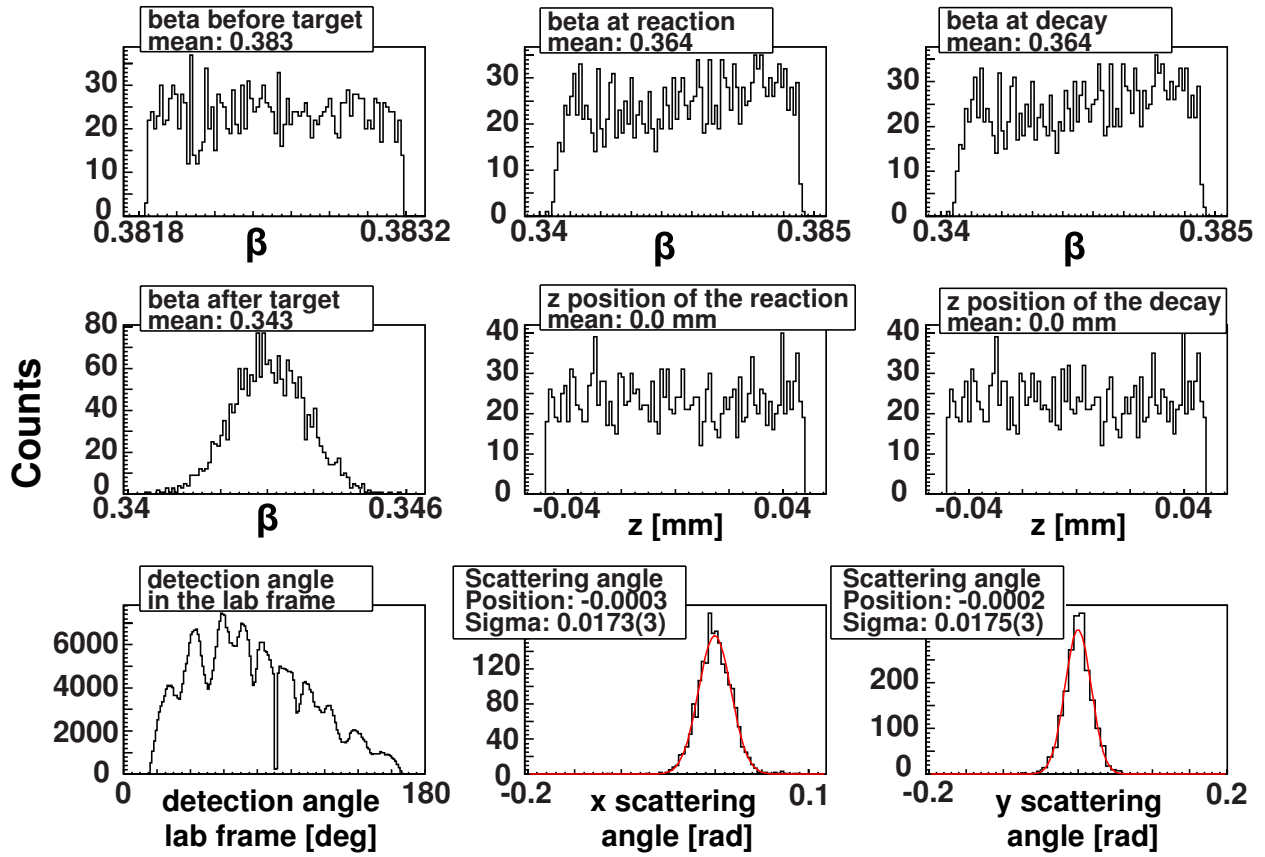
Figure 5.29 Shown are several simulated variables. Comparison with the input values from Table 5.3 shows a good agreement.
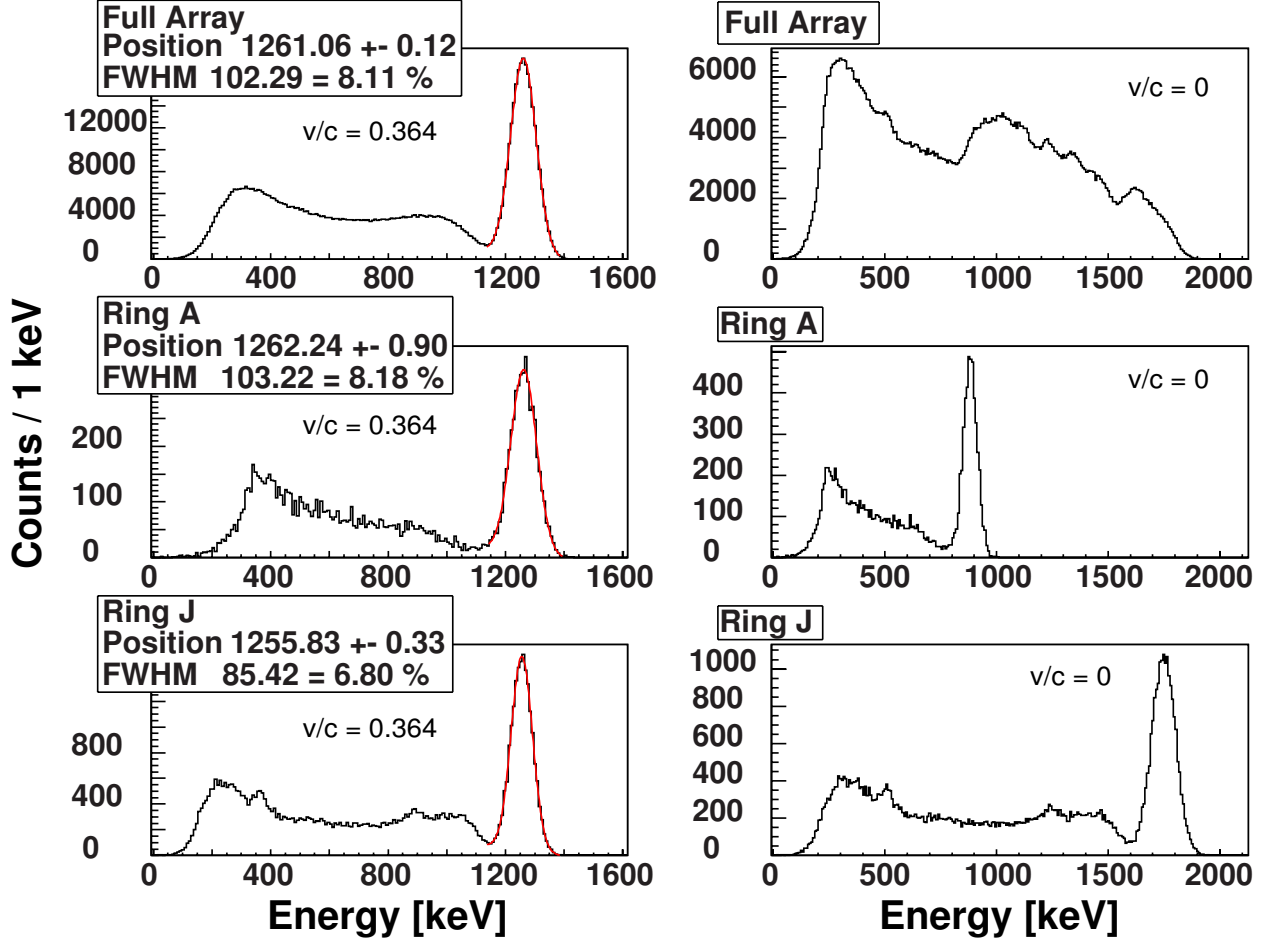
Figure 5.30 Simulated γ-ray spectra for ^{104}Sn. On the left side are the spectra Doppler corrected and on the right side not. The simulation is again in good agreement with the input data and with the expectations of the response of *CAESAR*.

5.6   Relative Measurement Results

In previous experiments, the usual procedure was to determine the absolute angle-integrated Coulomb excitation cross section, $\sigma(\theta_{lab} \leq \theta_{lab}^{max})$, and translate it into absolute $B(\pi\lambda)$ excitation strengths using the Winther-Alder description of intermediate-energy Coulomb excitation [45]. However, this was not possible in the current work as the absolute efficiencies of this new setup and data acquisition system were not as well characterized compared to previous works (e.g. using the *S800* spectrograph - see [68] for example). For more details see Sec. 5.3.2.3. Therefore, the $B(E2 \uparrow) = B(E2; 0^+ \rightarrow 2_1^+)$ excitation strength for ^{104}Sn was
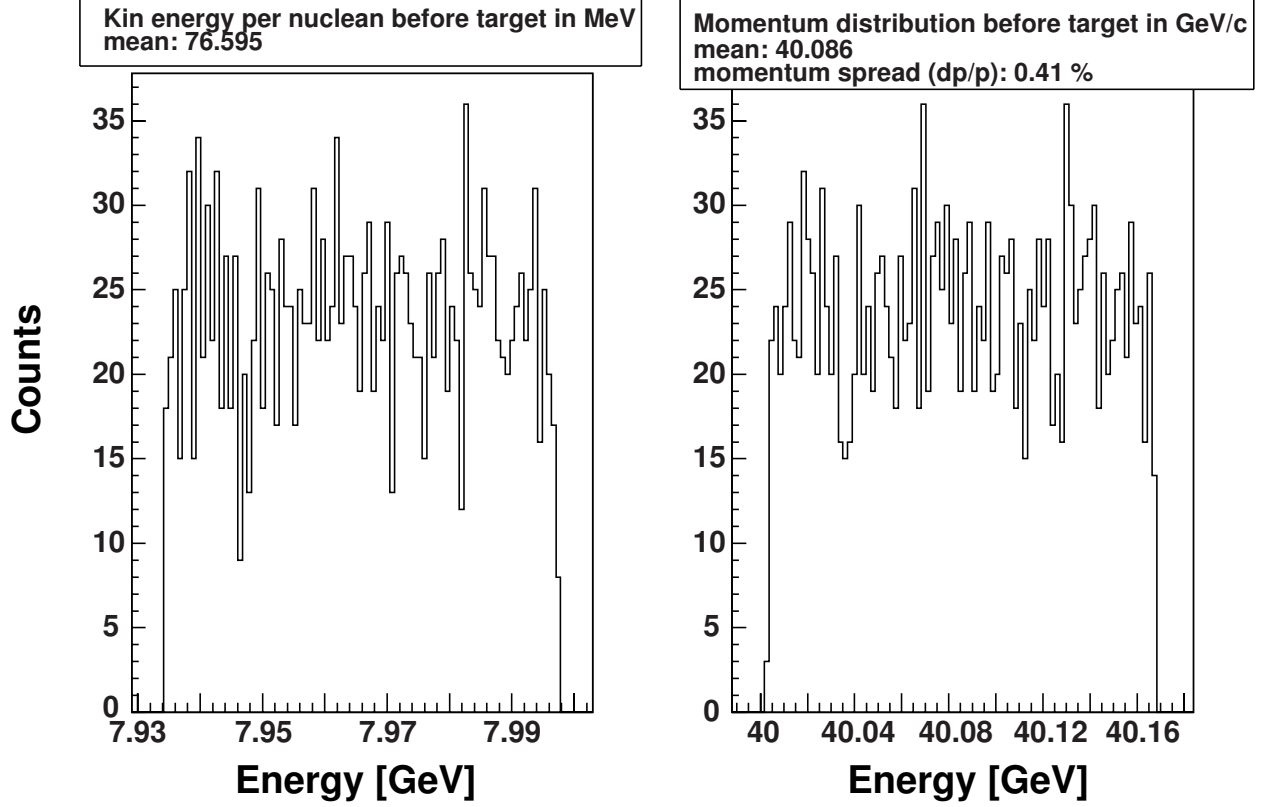
Figure 5.31 Last test of the simulation. Two more variables that were simulated are shown and again a comparison with the input values from Table 5.3 shows a good agreement.

determined relative to the well known $B(E2\uparrow)$ value of ^{102}Cd [2], which Coulomb excitation yield was measured in this experiment at the very same time, under identical conditions and with good statistics. The relative determination of the excitation strength was performed this way:

$$B(E2\uparrow)^{Sn} = B(E2\uparrow)^{Cd} \cdot \frac{N_\gamma^{Sn} N_{proj}^{Cd} AW(Cd)}{N_\gamma^{Cd} N_{proj}^{Sn} AW(Sn)}, \tag{5.5}$$

with $N_\gamma^{Sn,Cd}$ and $N_{proj}^{Sn,Cd}$ the number of 2_1^+ de-excitation γ rays and projectiles for ^{104}Sn and ^{102}Cd, respectively. The term $AW(Sn,Cd)$ is the Alder-Winther angle-integrated Coulomb excitation cross section, $\sigma(\theta_{\text{lab}} \leq 2.578°)$ per unit $B(E2)$ value, for ^{104}Sn and ^{102}Cd, respectively, taking into account the proper kinematics and atomic number of the projectiles. The

error was calculated as follows:

$$
\Delta B(E2\uparrow)^{Sn} = B(E2\uparrow)^{Cd} \cdot \left[\left(\frac{\Delta N_\gamma^{Sn}}{N_\gamma^{Sn}} \right)^2 + \left(\frac{\Delta N_\gamma^{Cd}}{N_\gamma^{Cd}} \right)^2 + \left(\frac{\Delta N_{proj}^{Sn}}{N_{proj}^{Sn}} \right)^2 \right.
$$
$$
\left. + \left(\frac{\Delta N_{proj}^{Cd}}{N_{proj}^{Cd}} \right)^2 + \left(\frac{\Delta B(E2\uparrow)^{Cd}}{B(E2\uparrow)^{Cd}} \right)^2 \right]^{\frac{1}{2}} .
$$

(5.6)

The simulated *Geant4* response of *CAESAR* was scaled to the ^{104}Sn and ^{102}Cd data to determine the number of 2_1^+ de-excitations, N_γ. The simulations takes into account *CAESAR*'s γ-ray detection efficiency and the absorption in the gold target and surrounding materials and include the calculated γ-ray angular distribution in Coulomb excitation [45, 48]. The simulated response functions fitted on top of a double-exponential smooth background are shown in Fig. 5.32.
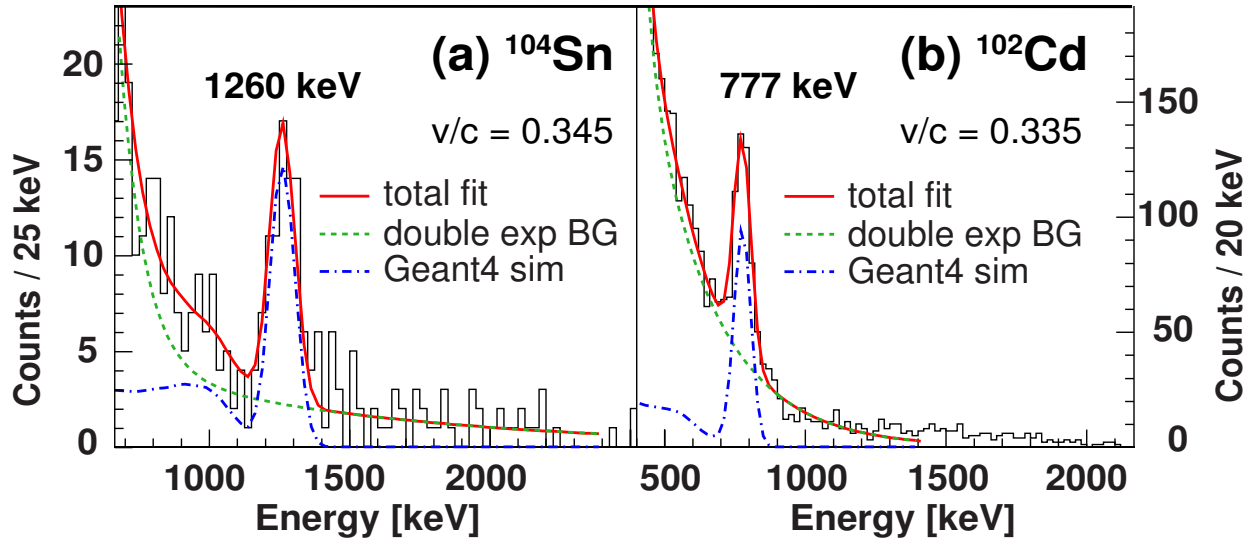
Figure 5.32 Event-by-event Doppler reconstructed γ-ray spectra detected in coincidence with scattered ^{104}Sn (a) and scattered ^{102}Cd (b). γ-ray transitions at 1260 keV and 777 keV can be clearly identified and are attributed to the de-excitation γ rays from the first excited 2^+ state in ^{104}Sn and in ^{102}Cd, respectively.

The shape of the double exponential background was confirmed by rescaling it and comparing it to a γ-ray spectrum of a neighboring nucleus in the cocktail beam which was created under

identical circumstances. To confirm the shape for ^{104}Sn, the spectrum of ^{102}In was chosen and for ^{102}Cd it was ^{100}Ag (see Fig. 5.13). In both cases, the difference between each pair of of the nuclei is one less proton and neutron so they have very similar properties. As shown in Fig. 5.33, the shape of the background is confirmed by the spectra which have no γ-ray transition in the region of interest. Of course, only the main features of the shape can be confirmed and no exact match is expected due to the slight difference in A and Z.
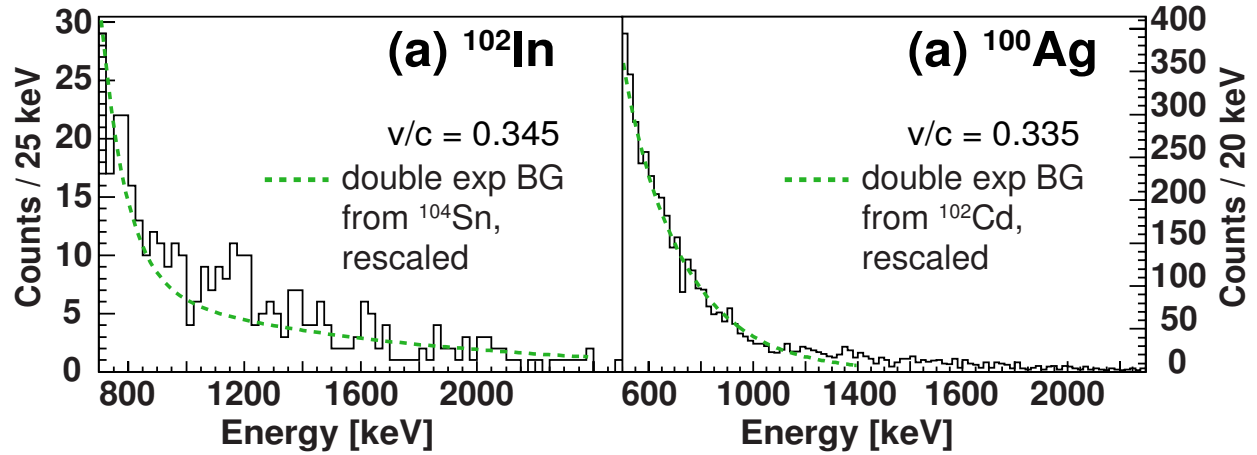
Figure 5.33 Event-by-event Doppler reconstructed γ-ray spectra detected in coincidence with scattered ^{102}In (a) and scattered ^{100}Ag (b). Shown are the ^{104}Sn background fit scaled to ^{102}In (a) and the ^{102}Cd background fit scaled to ^{100}Ag. In both spectra, no de-excitations are observed in the sensitive region.

The number of projectiles, N_{proj}, was determined from the particle identification spectrum shown in Fig. 5.14 which was gated on downscaled particle singles trigger. Two dimensional Gaussian fits, also shown in the figure, were used to estimate the contamination from neighboring, highly intense constituents of the cocktail beam (see Sec. 5.2.2). These corrections to the number of projectiles were below 3% for both ^{104}Sn and ^{102}Cd.

The results of the fits and otherwise necessary information are listed in table 5.4.

Property	^{104}Sn	^{102}Cd
AW coefficient [mb/(100 $e^2 fm^4$)]	15.30	14.92
Corrected number of incoming ions	2.347(10)E+06	6.022(17)E+06
number of 2_1^+ de-excitation γ rays	262(42)	1017(75)

Table 5.4 Important fit and calculation results.

Chapter 6

Results and Discussion

With the known value of $B(E2\uparrow) = 0.28(3)$ e^2b^2 for ^{102}Cd [2], a $B(E2\uparrow)$ value of $B(E2\uparrow) = 0.180(37)$ e^2b^2 is deduced for ^{104}Sn. The uncertainty includes all statistical uncertainties of N_{proj}, uncertainties from the fits of the response functions used to derive N_γ and the uncertainty of the ^{102}Cd $B(E2\uparrow)$ value. The aforementioned normalization eliminates systematic uncertainties stemming from the angle-determination with the PPAC and absolute efficiencies in general. This result compares well with the work by Doornenbal [7] and disagrees with the recently published value from a relativistic Coulomb excitation measurement performed at GSI [1]. In [7], the impact of unobserved feeding is discussed but for the relative measurement performed here it does not play a role. ^{102}Cd and ^{104}Sn have rather comparable proton separation energies, $S_p = 5.614$ MeV and $S_p = 4.286$ MeV, respectively, with a similar potential of unobserved feeding from higher-lying 3^- and 2^+_n states. Nuclear contributions are minimized in this work by very conservative minimum impact parameters that the analysis is restricted to, avoiding model-dependent estimates of the nuclear contribution (see Sec. 5.3.2.2). The result of this work and the literature values are summarized in Table 6.1. An overview of the measured $B(E2\uparrow)$ values along the Sn isotopic chain is given in Fig. 6.1(a).

In order to understand the trend in the $B(E2\uparrow)$ strength toward ^{100}Sn, several large-scale shell-model (LSSM) calculations were performed. A recently parametrized nucleon-nucleon force based on chiral perturbation theory [23] (at next-to-next leading order, NNLO) was used

Isotope	$B(E2\uparrow)_{literature}$ $(e^2\mathrm{b}^2)$	Reference	$B(E2\uparrow)$ $(e^2\mathrm{b}^2)$
^{102}Cd	0.28(3) ^{a} 0.281(45)	[2] [43]	
^{104}Sn	0.10(4) 0.163(26)	[1] [7]	0.180(37)

Table 6.1 $B(E2; 0_1^+ \rightarrow 2_1^+)$ values for ^{102}Cd and ^{104}Sn from literature and from this work (^{104}Sn); the results from [2] are used for normalization in Eq. 5.5.

---

^{a}The error includes statistical and systematic uncertainties.

as well as the N^{3}LO nucleon-nucleon interaction of [24]. The influence of three-body forces following Ref. [69] was also studied. ^{100}Sn was employed as a closed-shell core, which leaves no *valence protons* and only 4 *valence neutrons* for ^{104}Sn. The model space for the neutrons was defined by the quantum numbers of the $0h_{11/2}$, $2s_{1/2}$, $1d$ and $0g_{7/2}$ single-neutron states. In Fig. 6.2 is this configuration shown. All LSSM calculations were performed by Morten Hjorth-Jensen.

One major problem with this model space is that the spacing of the single-neutron states in the model space is not well known. This is because the single-particle energies of ^{101}Sn are not known experimentally, except for the spacing between the $7/2_1^+$ and the $5/2_1^+$ states of 170 keV [70, 71]. The effective neutron charge was set to $0.5e$ for all calculations.

All of these calculations result in rather similar behaviors for the $B(E2\uparrow)$ transitions in the neutron-deficient Tin isotopes. In Fig. 6.1 are therefore only the results presented for the newly optimized NNLO interaction [23], together with those obtained with the N^{3}LO interaction [24]. The latter interaction also gives the overall best reproduction of the excited states and binding energies. Thus, unless one adopts a phenomenological adjustment of the effective neutron charges, see for example Ref. [72], theory based on an inert proton core fails to describe the $B(E2\uparrow)$ strengths in Tin.
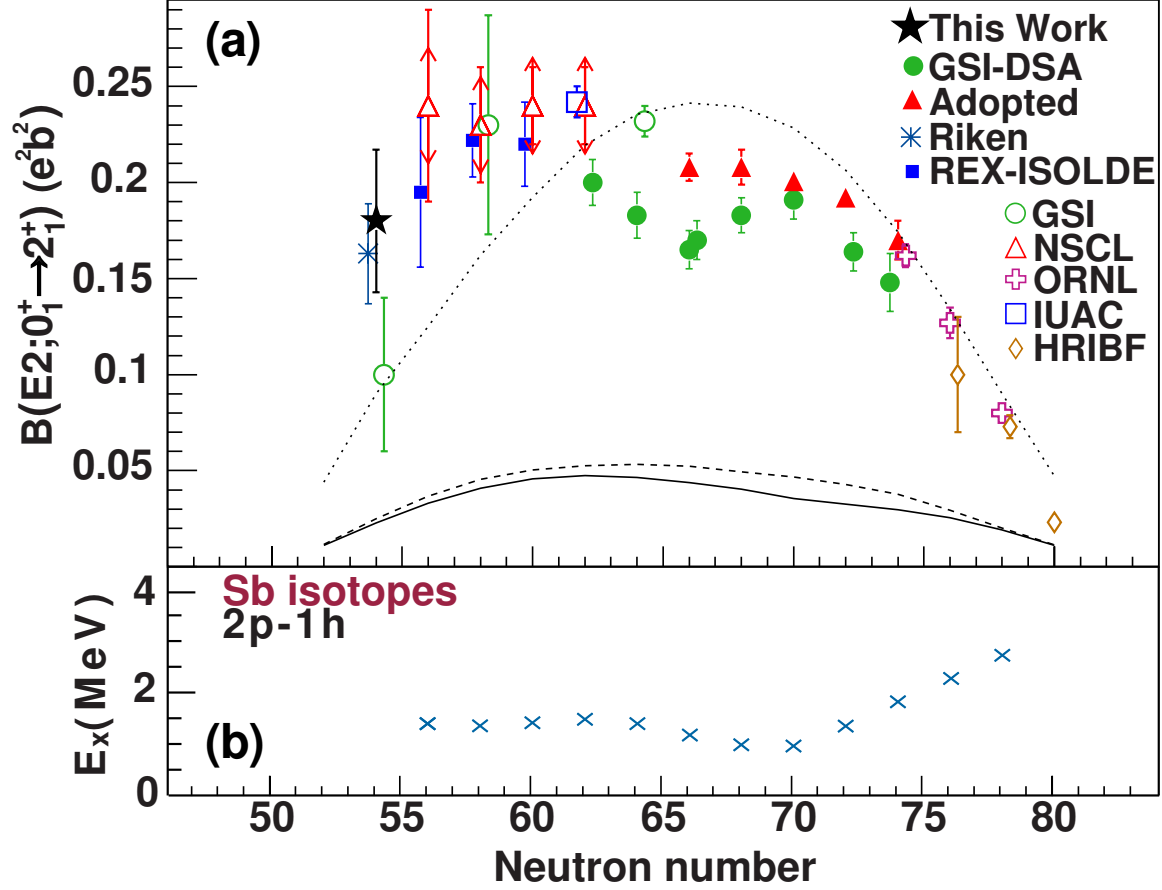
Figure 6.1 (a) Measured $B(E2 \uparrow)$ values for the chain of Sn isotopes: Adopted [6], Riken [7], REX-ISOLDE [8, 9], GSI-DSA [10], GSI [1, 11, 12], NSCL [13], ORNL [14], IUAC [15], HRIBF [16]. Solid line: Large-scale shell-model (LSSM) calculations with NNLO interaction [23]. Dashed line: LSSM with N^3LO interaction [24]. These two lines correspond to calculations performed with an effective neutron charge set to $0.5e$. An increase to $1e$ would yield and increase by a factor of 4 for the calculated $B(E2 \uparrow)$ values. The dotted line reproduces the $0g1d2s$ ($t_\pi = 4$) calculation shown in [11]. See text for details. (b) Energies of the proton $2p - 1h$ intruder states in Sb nuclei [25].

For further references, proton particle-hole excitations (np-nh) will be described by a single letter, $t_\pi = n$. The number of particles and holes for protons has to be the same (both n) because there are only *valence protons* below the Fermi energy.

The results of the here performed calculations are similar to the $t_\pi = 0$ results shown in Fig. 3 of [11]. If the neutron effective charge is increased to $1.0e$, then the $B(E2 \uparrow)$ values are increased by a factor of 4 and are in better agreement with the data. With that increase

Model space

82	$0h_{11/2}$	[12]	82
	$2s_{1/2}$	[2]	70
	$1d_{3/2}$	[4]	68
	$1d_{5/2}$	[6]	64
	$0g_{7/2}$	[8]	58

Fermi energy

50 ^{100}**Sn core** **50**

[10]	50	$0g_{9/2}$		$0g_{9/2}$	[10]	50
[2]	40	$1p_{1/2}$		$1p_{1/2}$	[2]	40
[4]	38	$1p_{3/2}$		$1p_{3/2}$	[4]	38
[6]	34	$0f_{5/2}$		$0f_{5/2}$	[6]	34
			28			
[8]	28	$0f_{7/2}$		$0f_{7/2}$	[8]	28
			20			
[2]	20	$1s_{1/2}$		$1s_{1/2}$	[2]	20
[4]	18	$0d_{3/2}$		$0d_{3/2}$	[4]	18
[6]	14	$0d_{5/2}$		$0d_{5/2}$	[6]	14
			8			
[2]	8	$0p_{1/2}$		$0p_{1/2}$	[2]	8
[4]	6	$0p_{3/2}$		$0p_{3/2}$	[4]	6
			2			
[2]	2	$0s_{1/2}$		$0s_{1/2}$	[2]	2

Protons   **Neutrons**
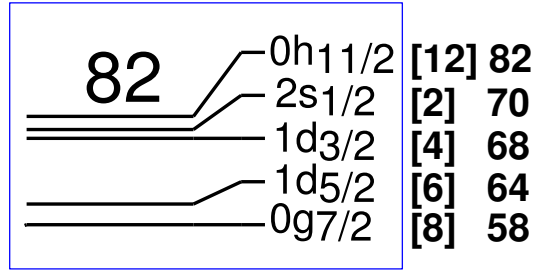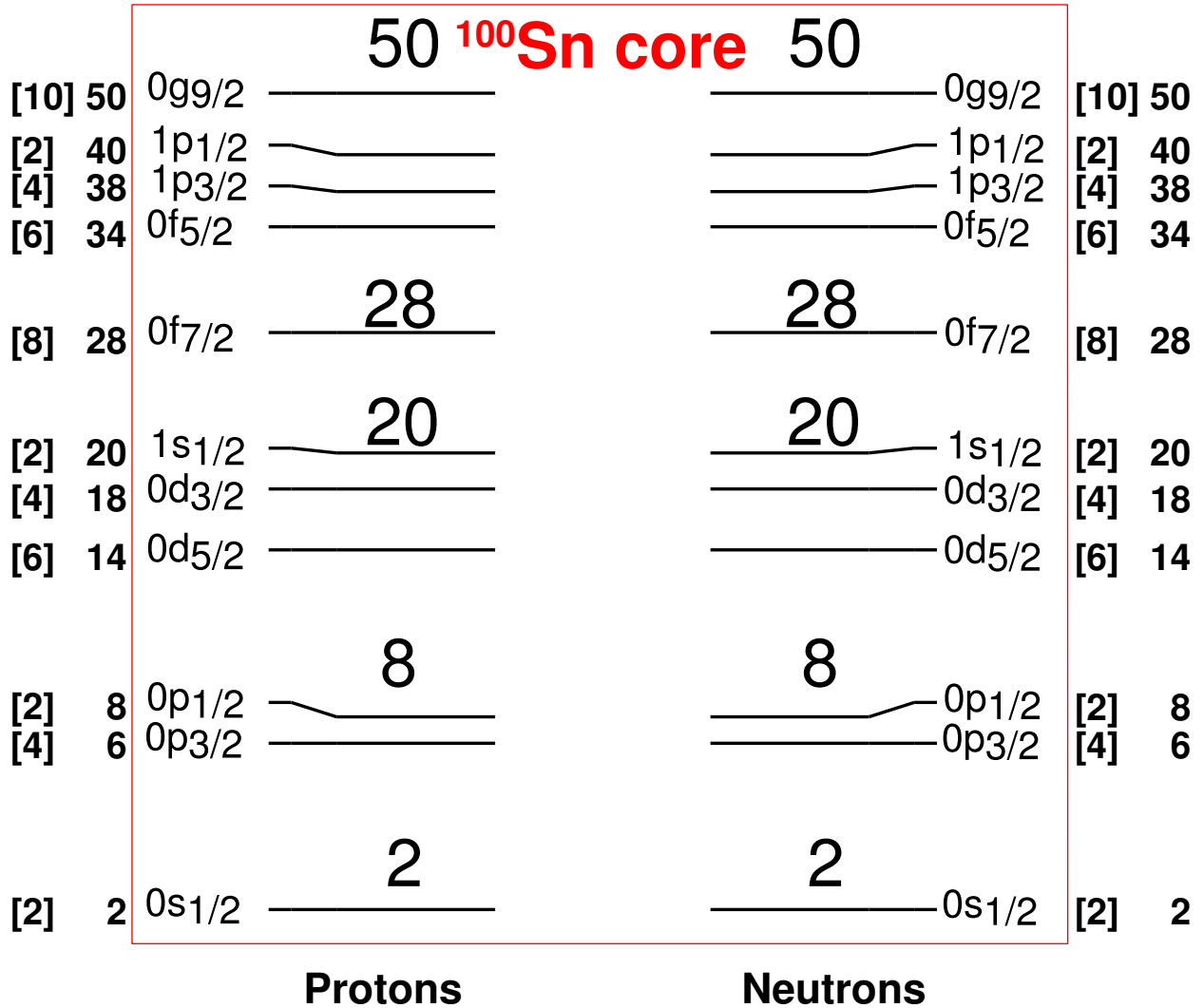
Figure 6.2 Shell model configuration with a closed ^{100}Sn core. The closed core is marked in red, the model space for the *valence neutrons* is marked in blue and the Fermi energy is marked in green. The visible numbers are the same as in Fig. 2.3. Figure is taken and modified from [4].

117

the solid and dashed line in Fig. 6.1 would be very similar to the dotted line. But they are still too small for the neutron-deficient Tin isotopes.

In [11], the model space was increased to allow up to four protons to be excited from the $0g_{9/2}$ orbital to $1d$, $2s_{1/2}$ and $0g_{7/2}$, ($t_\pi = 4$). The inert core used for these calculations was a ^{90}Zr core. This configuration is shown in Fig. 6.3.

The results from this calculation, with effective charges $1.5e$ for protons and $0.5e$ for neutrons, are also shown in Fig. 6.1 as the dotted line. Overall, the data is much better described, except that the extended calculation is symmetric around the middle, whereas experiment shows an asymmetry with an enhancement at the neutron-deficient end.

With the help of B. A. Brown the following interpretation was developed. In [13], the comparison to data and theory for the Nickel isotopes was discussed. ^{56}Ni (28 protons and neutrons) and ^{100}Sn (50 protons and neutrons) are similar with regard to their structure and shell gaps. At the closed-shell limit, they are both jj closed shells with the $0f_{7/2}$ and $0g_{9/2}$ orbitals filled, respectively. There are low-lying particle-hole ($np - nh$) excitations across the shell gap that give a moderately large calculated $B(E2\uparrow)$ strength in ^{56}Ni (it was experimentally observed in [73]) and ^{100}Sn (not yet experimentally observed but calculated for Fig. 4 of [1]). These $np - nh$ proton excitations couple coherently to the neutron configurations. The resulting increase in the $B(E2\uparrow)$ values could be interpreted in terms of an additional neutron core-polarization charge for a model space that involves only the *valence neutrons*.

The ^{100}Sn effective single-particle energy (ESPE) shell gap for the calculations given was about 7.5 MeV (see Fig. 6.4 taken from [11]). In comparison, the ESPE gap for the calculations used for the Nickel isotopes in Fig. 4 of [13] is 7.1 MeV. The correlated gap obtained from the full $1p0f$-shell calculation and from experimental ground-state binding energies of
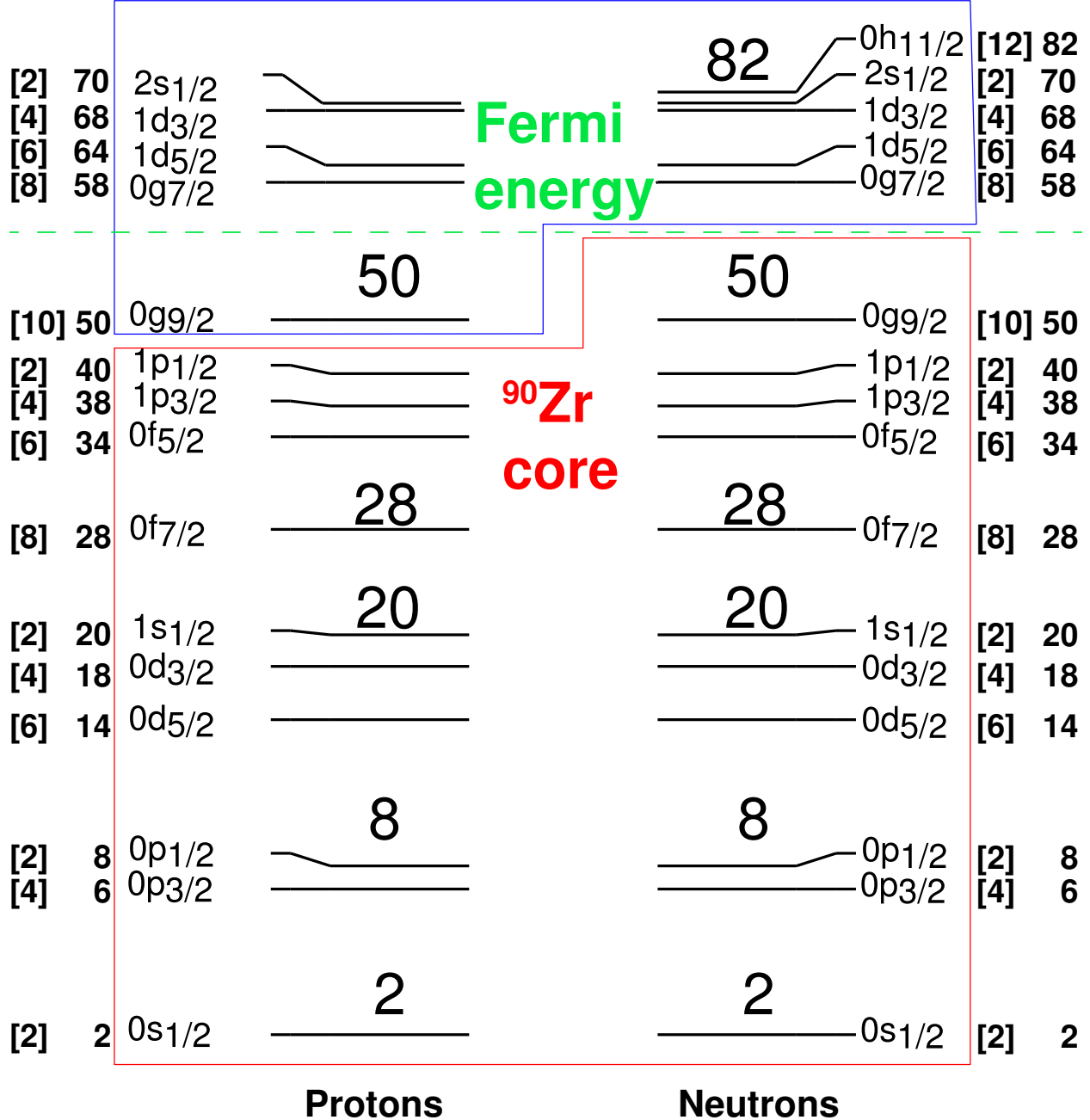
Figure 6.3 Shell model configuration with a closed ^{90}Zr core. The closed core is marked in red, the model space for the *valence neutrons* and up to 4 protons ($t_\pi = 4$) is marked in blue and the Fermi energy is marked in green. The visible numbers are the same as in Fig. 2.3. Figure is taken and modified from [4].
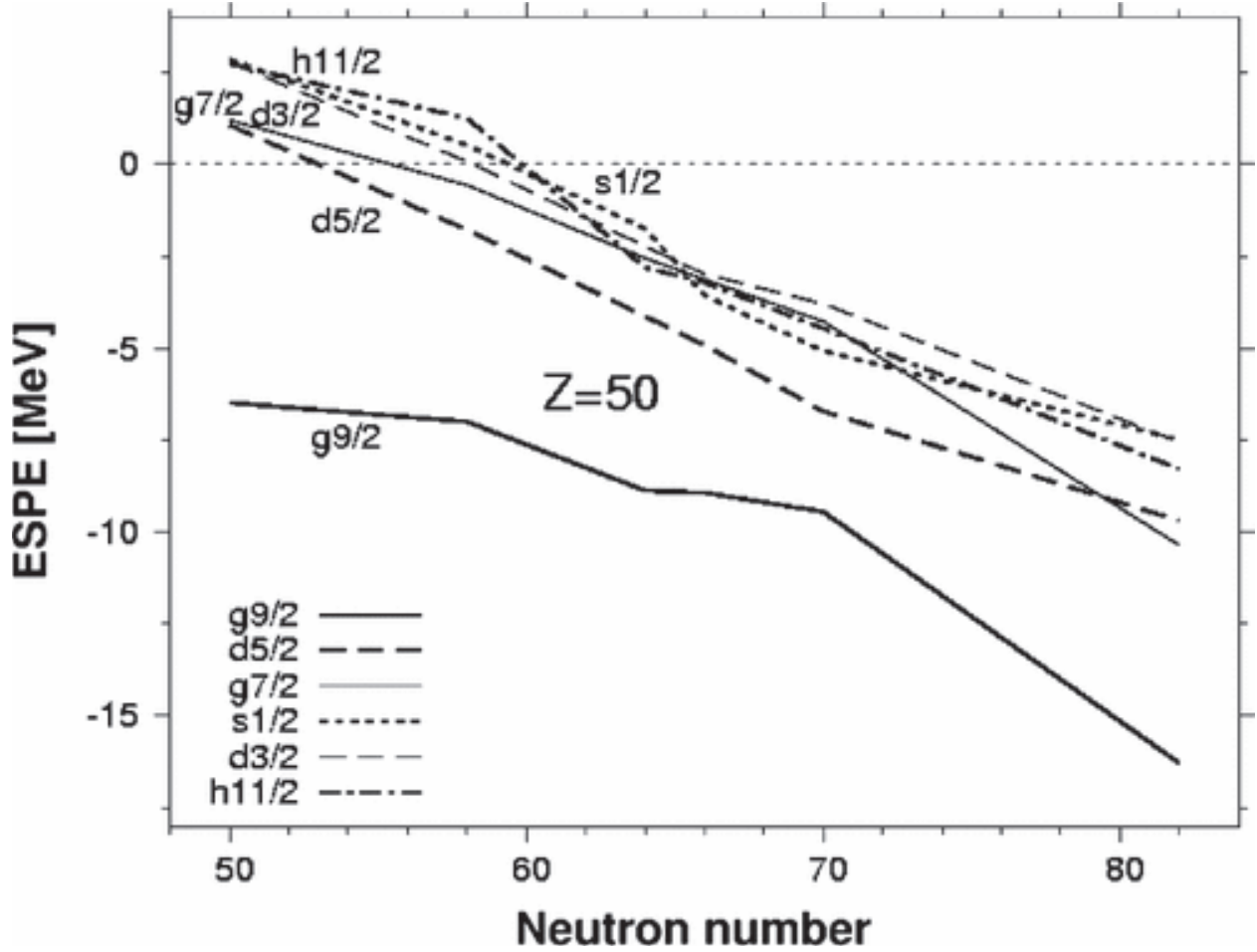
Figure 6.4 Calculated evolution of the proton ESPE with the neutron number N along the chain of Sn isotopes. Figure is taken and modified from [11].

^{55,56,57}Ni is 6.4 MeV. The correlated gap for ^{100}Sn is not known experimentally and the theoretical value is not provided in [11]. The shell gaps obtained with some Skyrme energy-density functionals for ^{100}Sn are 5.2 MeV (Skx) [74], 5.9 MeV (SLy4) [75] and 5.8 MeV (SkM*) [76], and for ^{56}Ni are 4.1 MeV (Skx), 4.8 MeV (SLy4) and 4.7 MeV (SkM*). Thus, the shell gaps for ^{56}Ni and ^{100}Sn are similar.

The energy of the two-proton excitation is much lower than twice the shell gap energy due to pairing and α correlations. For ^{102}Sn, the two excited protons go into the same deformed quantum states that are occupied by the two *valence neutrons* (see Fig. 6.5 taken from [13]). This lowers the energy due to the α-correlation energy and increases mixing with the neutron

configurations near $N = Z$.
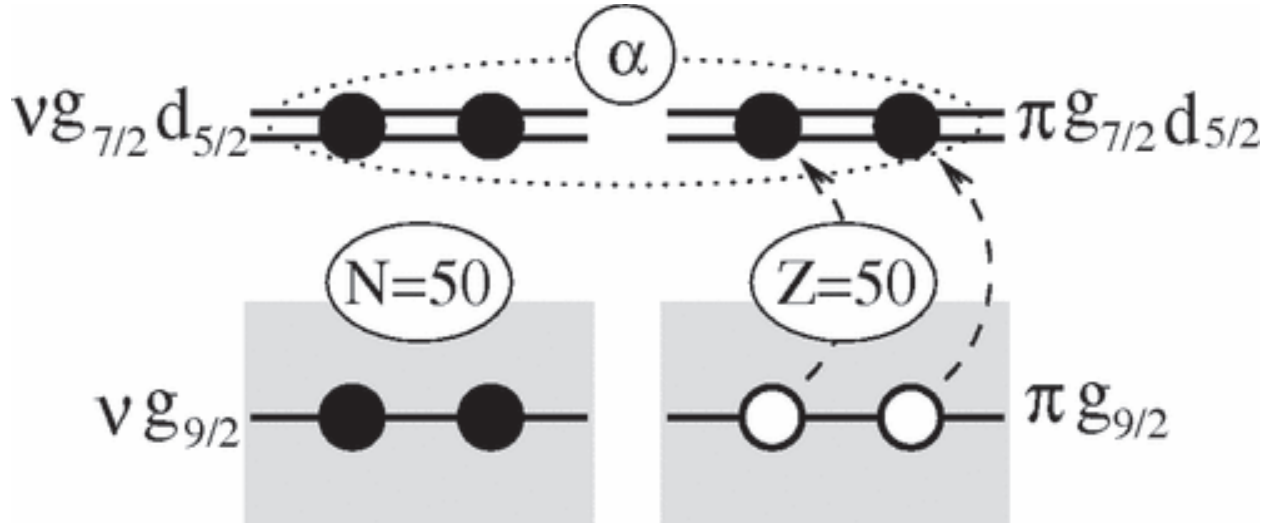
Figure 6.5 Schematic representation of the proton $2p-2h$ excitations across the $Z = 50$ shell gap in ^{102}Sn. The occupation of the same proton and neutron orbitals above the $Z = N = 50$ shell leads to α-like correlations between the *valence nucleons*. Figure is taken and modified from [13].

The α correlation persists for ^{104}Sn and gradually decreases for increasing number of neutrons since the configurations for the added neutrons differ from the proton configurations. Thus, α correlations provides a mechanism to generate an asymmetry in the $B(E2 \uparrow)$ values between $N = 50$ and $N = 82$. Part of the α correlations could be missed in the $(t_\pi = 4)$ calculations due to the truncation that had to be made for Tin. In addition, there is an asymmetry-inducing contribution to the $B(E2 \uparrow)$ values beyond $(t_\pi = 4)$ that is obtained in the Nickel calculations.

In contrast to the $(t_\pi = 4)$ calculation for Tin isotopes that is symmetric around mid-shell, the equivalent calculation for Nickel (Fig. 4 in [13]) shows an asymmetry with larger $B(E2 \uparrow)$ values at the neutron-deficient end. For ^{60}Ni, a calculation with a ^{56}Ni closed shell (4 valence neutrons) yields a $B(E2 \uparrow)$ value of only 0.010 e^2b^2 whereas opening up the full $1p0f$ model space results in a 10-fold increase to 0.105 e^2b^2. This large increase is due to the proton

excitations and their coherent contribution to the $E2$ transition matrix elements. In addition to the increase, an asymmetry is introduced as a function of the number of valence neutrons beyond ^{56}Ni such that the increase is larger at the neutron-deficient end. The energy of the proton core excitations near $N = Z$ is low due to α correlations for the protons and neutrons in the orbitals above $f_{7/2}$. It is likely that the origin of the difference between the calculations for Nickel and Tin comes from the truncations that must be made for Tin. The energy of the low-lying intruder states with $mp - nh$ configurations is also sensitive to these correlations. The $2p - 2h$ state in ^{60}Ni is observed at 3.32 MeV from the ^{56}Fe(^{6}Li,d) reaction [77]. The calculated energy of this state in the full $1p0f$ shell model is in agreement with experiment (see Fig. 20 of [78]). In Sn, the proton core-excitations are connected to the proton particle-hole intruder states observed in Sb isotopes. In the ^{100}Sn region, $2p - 1h$ states have been observed down to $N = 56$ in the Sb chain as shown in Fig. 6.1(b). The energies for the $2p - 1h$ $9/2^+$ levels have been identified and described in [79] for $^{113-119}$Sb nuclei and extended to ^{107,109}Sb in [80]. The trend, shown in Fig. 6.1(b) for Sb [25], may be attributed in addition to the α correlation in part also to shell evolution driven by the robust monopole parts of the proton-neutron tensor force [81]. The strongly attractive tensor force between the $\nu g_{7/2}$ and $\pi g_{9/2}$ orbitals weakens as the $g_{7/2}$ neutron occupation decreases from ^{108}Sn to ^{100}Sn, making the $\pi g_{9/2}$ orbital less bound and effectively narrowing the $Z = 50$ shell gap towards $N = 50$. On the neutron-rich end of the Sn chain, it is known that the $Z = 50$ shell gap is large at $N = 82$ [82–84]. This is consistent with the energy trend of the proton $2p - 1h$ excitations in Sb shown in Fig. 6.1(b), where the excitations across $Z = 50$ become increasingly more expensive towards $N = 82$, making the shell-model assumption of an inert proton core more valid. The role of the protons can be quantified further by comparison to ^{102,126}Cd with 4 neutron particles/holes relative to $N = 50/82$. The ratio of

122

$B(E2 \uparrow, {}^{126}\text{Cd})/B(E2 \uparrow, {}^{128}\text{Sn}) = 3$ [16, 85] indicates that with two protons added to ${}^{126}\text{Cd}$, the collectivity at ${}^{128}\text{Sn}$ drops by a factors of 3, owing to the absence of proton contributions in the heavier Sn. For $B(E2 \uparrow, {}^{102}\text{Cd})/B(E2 \uparrow, {}^{104}\text{Sn})$, the addition of two protons results in a loss of only a factor of 1.6 in collectivity, consistent with more proton contributions to the 2^+ wave function in ${}^{104}\text{Sn}$.

For nuclei closer to ${}^{100}\text{Sn}$ nothing is known yet about proton intruder excitations. Observation of these states and a comparison to the predictions of the models that include proton excitations are required to complete the understanding of the asymmetry. This prevalence of proton core excitations near $N = Z$ is also important for understanding the $B(E2 \uparrow)$ values in ${}^{18}\text{O}$, ${}^{42}\text{Ca}$ and ${}^{44}\text{Ca}$ [86, 87] – making the situation encountered in the Tin isotopes consistent with observations along proton-magic chains across the nuclear chart.

Chapter 7

Summary and Future Work

In summary, $B(E2; 0^+ \rightarrow 2_1^+)$ strength for ^{104}Sn was determined from intermediate-energy Coulomb excitation. The result is at variance with a recently published measurement [1]. Unlike the conclusion of [1], the departure from large-scale shell-model calculations persists for the neutron-deficient Sn isotopes approaching ^{100}Sn. This deviation from shell model seems to originate from the interplay of proton particle-hole configurations beyond the necessarily limited shell-model spaces. Those configurations and their effect on quadrupole collectivity is a common phenomenon along proton-magic isotope chains.

In the future, experiments measuring the $B(E2 \uparrow)$ values of ^{102}Sn and ^{100}Sn are a major goal and will help the understanding of the theory in this region. Especially doubly magic ^{100}Sn is a very interesting case because not even the energy of the first excited 2^+ state is yet known experimentally. With the construction of FRIB at Michigan State, the feasibility of producing ^{102}Sn and ^{100}Sn with a reasonable rate and purity increases greatly.

Following the arguments given in this thesis, one can predict the $B(E2 \uparrow)$ value of ^{102}Sn. Guidance can be given by the Nickel isotopes. In particular, ^{58}Ni is comparabel in its structure to ^{102}Sn. Both isotopes have 2 neutrons in addition to a jj closed $N = Z$ core, namely ^{56}Ni and ^{100}Sn (see Sec. 6). For both isotopes calculations with up to 4 proton particle-hole excitations ($t_\pi = 4$) were done as shown in Sec. 6. For ^{58}Ni the experimental $B(E2 \uparrow)$ value is known, too. Therefore, one can compare the experimental value for ^{58}Ni to

the shell model calculation and extract a scaling factor. This factor is estimated to be roughly 1.6 in comparison to the $t_\pi = 4$ LSSM calculation (estimated from Fig. 4 in [13]). Applying this factor to the $t_\pi = 4$ calculation of ^{102}Sn gives an estimated value of $B(E2 \uparrow) \approx 0.08 \, e^2\text{b}^2$. With the development of more powerful computers it would also be very interesting to lift the so far necessary restrictions of the LSSM calculations and open the proton $0g_{9/2}$ orbital up to allow excitations for all 10 protons. This will most likely confirm the hypothesis that the asymmetry in the experimentally observed $B(E2 \uparrow)$ values stems from proton particle-hole excitations and α correlations and can be reproduced by LSSM with a large enough model space.

APPENDIX

CAESAR Simulations

Travis Baugher and Geoffrey Grinyer wrote the *GEANT4* simulations [63] that were used in this experiment to fit the data. In the following is a summary of how to use the simulation which is taken from [3] with additions. It also entails a description of an analysis program, ions2.C and instructions on how to use the fitting programs. The simulations have been used in two publications so far [88, 89].

User's Guide for CAESAR Simulations

Installation

To use the simulation and sorting code, *Geant4*[1] and ROOT[2] need to be installed. Two versions of the simulation exist, one that can do only in-beam data but can separate the Compton edge from the *full energy peak* (*fep*) if wanted and one that cannot do the separation but can do source simulations. The simulation tarball is available from

`https://groups.nscl.msu.edu/gamma/wiki/doku.php?id=computers:computers`

it should be extracted into a directory of choice (all folder references are found in this directory) and compiled using the following commands.

---

[1]`http://geant4.web.cern.ch/geant4/`
[2]`http://root.cern.ch/drupal/`

On the NSCL network first run:

`export G4WORKDIR=$PWD`

and then

`source $GEANT4_PATH/share/Geant4-9.6.2/geant4make/geant4make.sh`

This sets the environment variables and then one can run

`make clean`

`make`

Running the Simulation

`UCCAESAR run.mac`

will start `UCCAESAR` and execute the commands in `run.mac`. See examples below.

Sorting

The program `caesarsort` is used to sort the output file into histograms. To compile, one has to go into the folder `caesarSort` and then execute

`make clean`

`make`

After that one has to go back into the main folder.

Do `caesarsort -h` for usage instructions.

Depending on which version is used (the in-beam separation version or the source version),

there are different caesarsorts.

For the source version one can just go ahead and run it like this:

```
./caesarsort run.out -o run.out.root
```

For the in-beam version there are three options, first:

```
./caesarsort run.out -o run.out.root
```

which does not separate the Compton edge and the *fep*, second:

```
./caesarsort -fep run.out -o run_fep.out.root
```

which gives one only the *fep* and lastly,

```
./caesarsort -compton run.out -o run_compton.out.root
```

which gives one only the Compton scattered contribution.

Spectrum naming: The naming convention used by `caesarsort` is as follows.

- `n0` means that each event in that spectrum did not have any neighboring detectors fire.

- `n1` means that exactly one of the neighboring detectors fired and add-back was done into the detector that registered the higher energy of the two.

- `n0n1` is `n0` and `n1` added together.

- `ng` means that more than two neighboring detectors fired so we do not know what to do (g for garbage).

- `cal` means not Doppler corrected

- `dop` means Doppler corrected.

Detector numbering: The most upstream ring is called ring A, most downstream is J. Within each ring, detectors are numbered starting from 1 with the upper left corner going clockwise if facing downstream (user is looking downstream).

Important text files: `caesarsort` reads these files at run time. They must be in the same directory as the executable.

- `neighbors.txt` has the neighbor relationships between the detectors for addback. Do not edit this unless one really wants to.

- `detectorPositions.txt` contains the positions of the detectors in space relative to the center of the array. This is another file one probably does not want to edit. This file is also read by the simulation program to set up the geometry.

- `omitDets.txt` one lists in here numbers of the detectors that should be left out of the sort. One might want to do this if there are missing detector signals, for example. Use the command `-x` to activate.

- `threshParams.txt` Model the energy threshold of the CFD for each individual detector. First column is the mean of a Gaussian, second column is FWHM

- `widthParams.txt` Parametrizes the energy resolution of each CAESAR detector as $\sigma(E) = aE^b$

- `Doppler.txt` Contains the β parameter for the Doppler reconstruction.

- `caesarSort/Def.h` Contains the parameter DEFAULT_DIM which defines how many bins are used for the sorting, the default is 8192.

Example Input Files

The following sections contain example macro files typically used to analyze an experiment. There are separate inputs for simulation of sources, in-beam experiments, target excitations, and ion tracking modes.

Before one does any of this it needs to be checked in **src/Beam_Tube.cc** that the parameter of the used beam pipe are the same as the one used in the experiment.

Source Simulations

Run source simulations to compare simulated and measured efficiency, determine resolution and threshold parameters.

```
# set up a simulation of a source

/Experiment/RunSource

/Experiment/Source/Set simple

# $\gamma$-ray energy to simulate

/Experiment/Source/setEnergy 662. keV

# target material and thickness: 'G4_Galactic' is vacuum, i.e., no target

/Target/Material G4_Galactic

/Target/Thickness 0.1 mm

# position of target and source emission point

/Target/SetPosition_Z 2.55 cm

/Experiment/Source/setZ 2.55 cm

# filename to save the output and number of $\gamma$ rays to simulate

/Output/Filename Cs137.out
```

```
/run/beamOn 1000000
```

In-beam Simulations

To simulate a γ-ray spectroscopy run, use:

```
# set up a simulation of an in-beam experiment

/Experiment/Reaction/On

# target material

/Target/Material Au

# thickness of target

/Target/Thickness 332.5 um

# size of target

/Target/X_length 5.0 cm

/Target/Y_length 5.0 cm

# position of target relative to the center of {\it CAESAR}

# positive values are downstream of center

/Target/SetPosition_Z 2.55 cm

# define the beam, this example is 74Ni

/BeamIn/A 74

/BeamIn/Z 28

# energy (per nucleon) of the incoming beam

/BeamIn/KEu 94.5 MeV

# fractional momentum spread of the incoming beam, 0.5\% = 0.005

/BeamIn/Dpp 0.005
```

```
# nucleons removed in the reaction, this is inelastic scattering

/BeamOut/DA 0

/BeamOut/DZ 0

#  excited state energy to simulate

/BeamOut/ProjectileExcitation 1024. keV

#excited state lifetime (not half life)

/BeamOut/tau 0 ps

# angular distribution coefficients for Coulomb excitation, calculated

  for a certain "safe" angle cut (here it is isotropic which is not

realistic)

/BeamOut/seta0 1.0

/BeamOut/seta2 0.0

/BeamOut/seta4 0.0

# outgoing beam angular distribution in the dispersive and non-dispersive

/BeamOut/AngDistSigmaA 0.012 rad

/BeamOut/AngDistSigmaB 0.012 rad

# print information about the simulation parameters

/BeamIn/Report

/BeamOut/Report

/Target/Report

/ExpHall/Report

/CAESAR_Array/Report

# print detailed information during simulation steps (diagnostic

  purposes and usually commented out because it generates a huge output)
```

```
#/IonPrint/Track_Set

# file to save the output

/Output/Filename 74Ni.out

# number of events to simulate

/run/beamOn 1000000
```

Ion Tracking

Ion tracking mode is useful for checking the beam parameters, such as kinetic energy, transverse and parallel momentum distributions, velocity, position and angles at several points during the simulation. To make sure that the set up of the simulation is correct the following steps need to be done:

- Make one simulation with the command /IonPrint/Track_Set active (usually commented out) in the .mac file and use 2000 particles.

- When one starts the simulation it has to be made sure that the output is written into a .log file like this: UCCAESAR test.mac > test.log

- Do a second simulation with the print command commented out: #/IonPrint/Track_Set and use at least 100000 particles

- Sort the last simulation with caesarsort to create a root file

- Start root and Load ions2.C with .L ions2.C.

- Type in the command Do("test.log","real_sim.root",A). The first input is the .log file which was created with only 2000 particles, the second input is the sorted

root file created with at least 100000 particles and the third input is the mass number A of the simulated beam.

This creates a ROOT file out of the `.log` file and also plots some overview spectra to check the simulations. One only has to run this once, if the `.log.root` file already exits and one wants to plot the overview spectra then one can use `Plot("test.log","real_sim.root",A)`.

Target Excitations

To simulate excitations of the target, ^{197}Au, for example, use:

```
# set up a simulation of an in-beam experiment
/Experiment/Reaction/On
# target material
/Target/Material Au
# thickness of target
/Target/Thickness 332.5 um
# size of target
/Target/X_length 5.0 cm
/Target/Y_length 5.0 cm
# position of target relative to the center of caesar
# positive values are downstream of center
/Target/SetPosition_Z 2.55 cm
# Produce only target excitations
/BeamOut/TargetExcitationFraction 1
#  excited state energy to simulate
```

```
/BeamOut/TargetExcitation 547.5 keV

# angular distribution coefficients for Coulomb excitation

# of the target

/BeamOut/setTargeta0 1.0

/BeamOut/setTargeta2 0.0

/BeamOut/setTargeta4 0.0

# print information about the simulation parameters

/BeamIn/Report

/BeamOut/Report

/Target/Report

/ExpHall/Report

/CAESAR_Array/Report

# file to save the output

/Output/Filename target_excitation.out

# number of events to simulate

/run/beamOn 1000000
```

Converting SPECTCL Spectra into Root Spectra

To use the fitting routines one needs to have all spectra in a root format. If one wants to convert SPECTCL spectra into root spectra follow these steps:

1. Make sure that the following programs are in the .bashrc file:

   module load root

   module load tv

2. Create a new directory, lets call it *NewDir* for now.

3. Copy the spectra one wants to transform into *NewDir*.

4. Also copy the programs **spc2root.sh** and **tvtxt2root.C** into *NewDir*.

5. Edit the **spc2root.sh** file so that the file path points to the local copy of **tvtxt2root.C**

6. Run the **spc2root.sh** with the file one wants to convert as an argument:

   ```
   ./spc2root.sh Example_histo.spc
   ```

   This creates the root spectrum!

Creating the right Spectra for the Fitting Procedures

To use the fitting routines the right format of the created simulation spectra is needed, e.g. the forward (ring F-J), backward (ring A-E) and full *CAESAR* (ring A-J) spectra are wanted. For this there are two little scripts called **ForwardBackward_Simulation.C** and **MakeFOrBackHistos_Simulation.C**.

ForwardBackward_Simulation.C is the actual program that creates the spectra. It has a function called plot that needs two input variables:

plot(char* inFile, char* Histogram)

The first is the file name of the created simulation root file but without the .root ending and the second is the histogram type that is supposed to be used. It creates a new file that has the same name as the input file with the difference that it ads **_Forward_Backward.root** to the new file name. One can simply use it by starting root, loading it:

```
.L ForwardBackward_Simulation.C
```

and then typing in the command

```
plot("test.out","cal")
```

which needs the file test.out.root created with caesarsort and then it creates all kinds of groupings for the histograms called "cal".

To make life easier there is also the program **MakeFOrBackHistos_Simulation.C** which simply executes the **ForwardBackward_Simulation.C** script several times in root. A typical command list looks like this:

```
{
  char buffer[1000];
  sprintf(buffer,".L ForwardBackward_Simulation.C");
  gROOT->ProcessLine(buffer);


  plot("56Ni_2700.out","cal");
  plot("56Ni_2700.out","dop");
  plot("56Ni_2700.out","n0_cal");
  plot("56Ni_2700.out","n0_dop");


  plot("56Ni_2700_fep.out","cal");
  plot("56Ni_2700_fep.out","dop");
  plot("56Ni_2700_fep.out","n0_cal");
  plot("56Ni_2700_fep.out","n0_dop");


  plot("56Ni_2700_compton.out","cal");
  plot("56Ni_2700_compton.out","dop");
```

```
    plot("56Ni_2700_compton.out","n0_cal");

    plot("56Ni_2700_compton.out","n0_dop");

}
```

And it can be executed by starting root and then using the command:

`.x MakeFOrBackHistos_Simulation.C`

Fitting Scripts

A script was was written which fits the simulated *CAESAR* spectra to the data. It can do this with as many simulated peaks as one wants and there are two versions. One version fits the Compton part and the *fep* part separately with a scaling factor between the two as free parameter. The other one fits the whole simulation to it. In both cases one can choose if the fit should include all rings of *CAESAR* or only the forward or backward rings. Another option is to choose what simulation should be fitted to the data, either all or n0 and so on. In general the fits can either just fit the simulations to the data or they can include a double exponential background. For the separate version the fitting routine has one free parameter for every Compton-*fep* pair, one free parameter for an overall ratio between the Compton and *fep* part and if wanted 4 more free parameters for the double exponential background. The version that does the full simulation fit just has one free parameter for each simulated peak and if wanted 4 more free parameters for the double exponential background. The first script is called **Fit_seperate_const.C** and the second one **Fit.C**.

How the script for the fits with the separate Compton and *fep* part, **Fit_seperate_const.C**,

works is shown at hand of the Ni56 case. Before one can use the script some settings need to be changed:

```
int comp = 2;    //number of total simulations one wants to fit

int comp2 = 1;   //number of simulation pairs (Compton+fep) one wants to
fit (should be comp/2)

int rebin = 16;  //rebinning for the simulations

int rebin1 = 16; //rebinning for the data

                    (in the end data and sim must have same bin size)

int simPart = 10000000; //number of simulated particles
```

and if one wants to use the double exponential background

```
//bg fit for initial parameters excludes everything between exclude1 and exclude2

double exclude1 = 1600;

double exclude2 = 3200;
```

Then one has to tell the program where the simulations are. The input here have to be the files that were created with the **MakeFOrBackHistos_Simulation.C** program. One has to always give them as pairs so the *fep* part has to be 0 and the Compton part 1 and then the next simulated energy has its *fep* part assigned to 2 and Compton to 3 and so on.

```
TFile *fsim[comp];

fsim[0] = new TFile("56Ni_2700_fep.out_Forward_Backward.root");

fsim[1] = new TFile("56Ni_2700_compton.out_Forward_Backward.root");
```

Next it needs to be specified what simulated histogram should be used for the fitting, all of *CAESAR* or just the forward or backward part and if the full spectrum or for example n0 should be used. Only the spectrum that is desired should be commented in:

140

```
hsim[i] = (TH1F*)fsim[i]->Get("dop");

//hsim[i] = (TH1F*)fsim[i]->Get("dop_forwardrings");

//hsim[i] = (TH1F*)fsim[i]->Get("n0_dop");

//hsim[i] = (TH1F*)fsim[i]->Get("n0_dop_forwardrings");
```

The last change in the script is the naming of the histograms, make sure that all of them are named individually:

```
hsim[0]->SetName("2700_fep_dop");

hsim[1]->SetName("2700_compton_dop");
```

To use the fitting routine start root and compile the script by doing: .L Fit_seperate_const.C+ The script has a function called dofit:

```
dofit(const char* file, char* Histo, double from, double to, double from2, double
to2, int Ex);
```

The first input is the root data file, the second one is the name of the histogram that is supposed to be fitted. If one created the histogram by converting it from *SpecTcl* to root then it is always called `hist`. The next two numbers define the total fit range and the following two numbers define the range where the program gets its initial parameters for the double exponential background (it excludes the range one specified in the script). Not to get confused this is only to get good starting parameters for the final fit. The last number has to be either 0 or 1. It turns the background off or on in the final fit (0=off, 1=on). The fit can be run like this:

```
dofit("a-j_40mrad_m01.root","hist",1700,4500,800,4500,0);
```

It creates a nice little plot with all important information one needs. There are two possible warnings. One is about the exponential background, if this comes up it means that the

background is not monotone decreasing with increasing energy. The other error comes up if the ratio Compton to *fep* is negative. On the plot also show up 2 green and 4 red lines. the 2 green lines indicate the fitting range for the total fit. In between the first two red lines and in between the third and fourth is indicated the range that was used to get starting parameters for the double exponential background.

BIBLIOGRAPHY

BIBLIOGRAPHY

[1] G. Guastalla, D. D. DiJulio, M. Górska, J. Cederkäll, P. Boutachkov, P. Golubev, S. Pietri, H. Grawe, F. Nowacki, K. Sieja, *et al.* Coulomb Excitation of ^{104}Sn and the Strength of the ^{100}Sn Shell Closure. *Phys. Rev. Lett.*, 110:172501, Apr 2013.

[2] A. Ekström, J. Cederkäll, D. D. DiJulio, C. Fahlander, M. Hjorth-Jensen, A. Blazhev, B. Bruyneel, P. A. Butler, T. Davinson, J. Eberth, *et al.* Electric quadrupole moments of the 2_1^+ states in ^{100,102,104}Cd. *Phys. Rev. C*, 80:054302, Nov 2009.

[3] T. Baugher. NEUTRON-RICH CHROMIUM AND MANGANESE ISOTOPES AND THE ROLE OF THE NEUTRON $0g_{9/2}$ AND $1d_{5/2}$ ORBITALS IN THE REGION BELOW ^{68}Ni. PhD thesis, Michigan State University, 2013.

[4] B. A. Brown. Lecture Notes in Nuclear Structure Physics, 2011.

[5] A. Ratkiewicz. COLLECTIVITY OF EXOTIC SILICON ISOTOPES. PhD thesis, Michigan State University, 2011.

[6] BNL Evaluated Nuclear Structure Data File (ENSDF).

[7] P. Doornenbal, S. Takeuchi, N. Aoi, M. Matsushita, A. Obertelli, D. Steppenbeck, H. Wang, L. Audirac, H. Baba, P. Bednarczyk, *et al.* Intermediate-energy Coulomb excitation of 104Sn: Moderate E2 strength decrease approaching ^{100}Sn. *arXiv preprint arXiv:1305.2877*, 2013.

[8] J. Cederkäll, A. Ekström, C. Fahlander, A. M. Hurst, M. Hjorth-Jensen, F. Ames, A. Banu, P. A. Butler, T. Davinson, U. Pramanik, *et al.* Sub-Barrier Coulomb Excitation of ^{110}Sn and its Implications for the ^{100}Sn Shell Closure. *Phys. Rev. Lett.*, 98:172501, Apr 2007.

[9] A. Ekström, J. Cederkäll, C. Fahlander, M. Hjorth-Jensen, F. Ames, P. A. Butler, T. Davinson, J. Eberth, F. Fincke, A. Görgen, *et al.* $0_{gs}^+ \rightarrow 2_1^+$ Transition Strengths in ^{106}Sn and ^{108}Sn. *Phys. Rev. Lett.*, 101:012502, Jul 2008.

[10] A. Jungclaus, J. Walker, J. Leske, K.-H. Speidel, A. E. Stuchbery, M. East, P. Boutachkov, J. Cederkäll, P. Doornenbal, J. L. Egido, *et al.* Evidence for reduced

collectivity around the neutron mid-shell in the stable even-mass Sn isotopes from new lifetime measurements. *Physics Letters B*, 695(14):110 – 114, 2011.

[11] A. Banu, J. Gerl, C. Fahlander, M. Górska, H. Grawe, T. R. Saito, H.-J. Wollersheim, E. Caurier, T. Engeland, A. Gniady, *et al.* ^{108}Sn studied with intermediate-energy Coulomb excitation. *Phys. Rev. C*, 72:061305, Dec 2005.

[12] P. Doornenbal, P. Reiter, H. Grawe, H. J. Wollersheim, P. Bednarczyk, L. Caceres, J. Cederkäll, A. Ekström, J. Gerl, M. Górska, *et al.* Enhanced strength of the $2_1^+ \to 0_{g.s.}^+$ transition in ^{114}Sn studied via Coulomb excitation in inverse kinematics. *Phys. Rev. C*, 78:031303, Sep 2008.

[13] C. Vaman, C. Andreoiu, D. Bazin, A. Becerril, B. A. Brown, C. M. Campbell, A. Chester, J. M. Cook, D. C. Dinca, A. Gade, *et al.* $Z = 50$ Shell Gap near ^{100}Sn from Intermediate-Energy Coulomb Excitations in Even-Mass $^{106-112}$Sn Isotopes. *Phys. Rev. Lett.*, 99:162501, Oct 2007.

[14] J. M. Allmond, D. C. Radford, C. Baktash, J. C. Batchelder, A. Galindo-Uribarri, C. J. Gross, P. A. Hausladen, K. Lagergren, Y. Larochelle, E. Padilla-Rodal, *et al.* Coulomb excitation of ^{124,126,128}Sn. *Phys. Rev. C*, 84:061303, Dec 2011.

[15] R. Kumar, P. Doornenbal, A. Jhingan, R. K. Bhowmik, S. Muralithar, S. Appannababu, R. Garg, J. Gerl, M. Górska, J. Kaur, *et al.* Enhanced $0_{g.s.}^+ \to 2_1^+$ transition strength in ^{112}Sn. *Phys. Rev. C*, 81:024306, Feb 2010.

[16] D. C. Radford, C. Baktash, C. J. Barton, J. Batchelder, J. R. Beene, C. R. Bingham, M. A. Caprio, M. Danchev, B. Fuentes, A. Galindo-Uribarri, *et al.* Coulomb excitation and transfer reactions with rare neutron-rich isotopes. *Nuclear Physics A*, 752(0):264 – 272, 2005. Proceedings of the 22nd International Nuclear Physics Conference (Part 2).

[17] D. J. Morrissey, B. M. Sherrill, M. Steiner, A. Stolz, I. Wiedenhoever. Commissioning the A1900 projectile fragment separator. *Nuclear Instruments and Methods in Physics Research Section B: Beam Interactions with Materials and Atoms*, 204(0):90 – 96, 2003. 14th International Conference on Electromagnetic Isotope Separators and Techniques Related to their Applications.

[18] O. B. Tarasov, D. Bazin. LISE++: Radioactive beam production with in-flight separators. *Nuclear Instruments and Methods in Physics Research Section B: Beam Interactions with Materials and Atoms*, 266(1920):4657 – 4664, 2008.

[19] D. Bazin, V. Andreev, A. Becerril, M. Dolans, P.F. Mantica, J. Ottarson, H. Schatz, J.B. Stoker, J. Vincent. Radio Frequency Fragment Separator at NSCL. *Nuclear Instruments*

and *Methods in Physics Research Section A: Accelerators, Spectrometers, Detectors and Associated Equipment*, 606(3):314 – 319, 2009.

[20] D. Weisshaar, A. Gade, T. Glasmacher, G. F. Grinyer, D. Bazin, P. Adrich, T. Baugher, J. M. Cook, C. Aa. Diget, S. McDaniel, *et al.* CAESARA high-efficiency CsI(Na) scintillator array for in-beam spectroscopy with fast rare-isotope beams. *Nuclear Instruments and Methods in Physics Research Section A: Accelerators, Spectrometers, Detectors and Associated Equipment*, 624(3):615 – 623, 2010.

[21] G. F. Knoll. Radiation Detection and Measurement. John Wiley & Sons, Inc., Third edition, 2000.

[22] D. J. Morrissey. Lecture Notes in Radiation detection and measurement, 2011.

[23] A. Ekström, G. Baardsen, C. Forssén, G. Hagen, M. Hjorth-Jensen, G. R. Jansen, R. Machleidt, W. Nazarewicz, T. Papenbrock, J. Sarich, *et al.* Optimized Chiral Nucleon-Nucleon Interaction at Next-to-Next-to-Leading Order. *Phys. Rev. Lett.*, 110:192502, May 2013.

[24] D. R. Entem, R. Machleidt. Accurate charge-dependent nucleon-nucleon potential at fourth order of chiral perturbation theory. *Phys. Rev. C*, 68:041001, Oct 2003.

[25] J. Shergur, D. J. Dean, D. Seweryniak, W. B. Walters, A. Wöhr, P. Boutachkov, C. N. Davids, I. Dillmann, A. Juodagalvis, G. Mukherjee, *et al.* Identification of low-spin states in ^{111}Sb: Test of spin-orbit coupling in light nuclei. *Phys. Rev. C*, 71:064323, Jun 2005.

[26] T. Otsuka. Exotic nuclei and nuclear forces. *Physica Scripta*, 2013(T152):014007, 2013.

[27] C. Forssn, G. Hagen, M. Hjorth-Jensen, W. Nazarewicz, J. Rotureau. Living on the edge of stability, the limits of the nuclear landscape. *Physica Scripta*, 2013(T152):014022, 2013.

[28] C. B. Hinke, M. Böhmer, P. Boutachkov, T. Faestermann, H. Geissel, J. Gerl, R. Gernhäuser, M. Górska, A. Gottardo, H. Grawe, *et al.* Superallowed Gamow-Teller decay of the doubly magic nucleus ^{100}Sn. *Nature*, 486(7403):341–345, 2012.

[29] A. Korgul, W. Urban, T. Rzca-Urban, M. Rejmund, J. L. Durell, M. J. Leddy, M. A. Jones, W. R. Phillips, A. G. Smith, B. J. Varley, *et al.* Properties of $N = 84$, even-even nuclei populated in the spontaneous fission of ^{248}Cm. *The European Physical Journal A - Hadrons and Nuclei*, 7(2):167–176, 2000.

[30] K. L. Jones, A. S. Adekola, D. W. Bardayan, J. C. Blackmon, K. Y. Chae, K. A. Chipps, J. A. Cizewski, L. Erikson, C. Harlin, R. Hatarik, *et al.* The magic nature of ^{132}Sn explored through the single-particle states of ^{133}Sn. *Nature*, 465(7297):454–457, 2010.

[31] K. S. Krane. Introductory Nuclear Physics. John Wiley & Sons, 1988.

[32] R. F. Casten. Nuclear Structure from a Simple Perspective. Oxford University Press, 1990.

[33] P. J. Mohr, B. N. Taylor, D. B. Newell. CODATA recommended values of the fundamental physical constants: 2010. *Rev. Mod. Phys.*, 84:1527–1605, Nov 2012.

[34] J. Beringer *et al.* Review of particle physics. *Phys. Rev. D*, 86:010001, Jul 2012.

[35] O. Haxel, J. H. D. Jensen, H. E. Suess. On the "Magic Numbers" in Nuclear Structure. *Phys. Rev.*, 75:1766–1766, Jun 1949.

[36] M. Goeppert Mayer. On Closed Shells in Nuclei. II. *Phys. Rev.*, 75:1969–1970, Jun 1949.

[37] B. A. Brown, B. H. Wildenthal. Status of the Nuclear Shell Model. *Annual Review of Nuclear and Particle Science*, 38(1):29–66, 1988.

[38] P. Navrátil, M. Thoresen, B. R. Barrett. Microscopic origins of effective charges in the shell model. *Phys. Rev. C*, 55:R573–R576, Feb 1997.

[39] J. Suhonen. From Nucleons to Nucleus, Concepts of Microscopic Nuclear Theory. Springer-Verlag Berlin Heidelberg, First edition, 2007.

[40] A. Bohr, B. R. Mottelson. Nuclear Structure: Nuclear Deformations, volume 2. World Scientific, 1998.

[41] T. Baugher, A. Gade, R. V. F. Janssens, S. M. Lenzi, D. Bazin, B. A. Brown, M. P. Carpenter, A. N. Deacon, S. J. Freeman, T. Glasmacher, *et al.* Intermediate-energy Coulomb excitation of ^{58,60,62}Cr: The onset of collectivity toward $N = 40$. *Phys. Rev. C*, 86:011305, Jul 2012.

[42] R. Winkler, A. Gade, T. Baugher, D. Bazin, B. A. Brown, T. Glasmacher, G. F. Grinyer, R. Meharchand, S. McDaniel, A. Ratkiewicz, *et al.* D. Weisshaar. Quadrupole Collec-

tivity beyond $N = 28$: Intermediate-Energy Coulomb Excitation of ^{47,48}Ar. *Phys. Rev. Lett.*, 108:182501, Apr 2012.

[43] N. Boelaert, A. Dewald, C. Fransen, J. Jolie, A. Linnemann, B. Melon, O. Möller, N. Smirnova, K. Heyde. Low-spin electromagnetic transition probabilities in ^{102,104}Cd. *Phys. Rev. C*, 75:054311, May 2007.

[44] A. Gade, T. Glasmacher. In-beam nuclear spectroscopy of bound states with fast exotic ion beams. *Progress in Particle and Nuclear Physics*, 60(1):161 – 224, 2008.

[45] A. Winther, K. Alder. Relativistic coulomb excitation. *Nuclear Physics A*, 319(3):518 – 532, 1979.

[46] B. R. Martin. Nuclear and Particle Physics. John Wiley & Sons, Ltd, First edition, 2006.

[47] H. Scheit. Low-Lying Collective Excitations in Neutron-Rich Even-Even Sulfur and Argon Isotopes Studied via Intermediate-Energy Coulomb Excitation and Proton Scattering. PhD thesis, Michigan State University, 1998.

[48] H. Olliver, T. Glasmacher, A. E. Stuchbery. Angular distributions of γ-rays with intermediate-energy beams. *Phys. Rev. C*, 68:044312, Oct 2003.

[49] D. J. Morrissey. The coupled cyclotron project at the NSCL. *Nuclear Physics A*, 616(12):45 – 55, 1997. Radioactive Nuclear Beams.

[50] G. Machicoane, D. Cole, J. Ottarson, J. Stetson, P. Zavodszky. ARTEMIS-B: A room-temperature test electron cyclotron resonance ion source for the National Superconducting Cyclotron Laboratory at Michigan State University. *Review of scientific instruments*, 77(3):03A322–03A322, 2006.

[51] P. A. Zavodszky, B. Arend, D. Cole, J. DeKamp, G. Machicoane, F. Marti, P. Miller, J. Moskalik, J. Ottarson, J. Vincent, *et al.* Design of SuSI Superconducting Source for Ions at NSCL/MSU - I. The Magnet System. In *AIP Conference Proceedings*, volume 749, page 131, 2005.

[52] P. A. Zavodszky, B. Arend, D. Cole, J. DeKamp, G. Machicoane, F. Marti, P. Miller, J. Moskalik, J. Ottarson, J. Vincent, A. Zeller. Design of SuSI Superconducting Source for Ions at NSCL/MSU II. The conventional parts. *Nuclear Instruments and Methods in Physics Research Section B: Beam Interactions with Materials and Atoms*, 241(14):959 – 964, 2005.

[53] H. Wiedemann. Particle Accelerator Physics. Springer-Verlag Berlin Heidelberg, Third edition, 2007.

[54] R. Pfaff, D. J. Morrissey, W. Benenson, M. Fauerbach, M. Hellström, C. F. Powell, B. M. Sherrill, M. Steiner, J. A. Winger. Fragmentation of ^{78}Kr projectiles. *Phys. Rev. C*, 53:1753–1758, Apr 1996.

[55] T. Ginter. *A1900 Fragment Separator and High-Energy Beamline Service Level Description*, 2007. NSCL internal document, `nscl.msu.edu/files/A1900_sld_2007.pdf`.

[56] J.P. Dufour, R. Del Moral, H. Emmermann, F. Hubert, D. Jean, C. Poinot, M.S. Pravikoff, A. Fleury, H. Delagrange, K.-H. Schmidt. Projectile fragments isotopic separation: Application to the lise spectrometer at GANIL. *Nuclear Instruments and Methods in Physics Research Section A: Accelerators, Spectrometers, Detectors and Associated Equipment*, 248(23):267 – 281, 1986.

[57] D. Bazin, F. Montes, A. Becerril, G. Lorusso, A. Amthor, T. Baumann, H. Crawford, A. Estrade, A. Gade, T. Ginter, *et al.* Production and β Decay of *rp*-Process Nuclei ^{96}Cd, ^{98}In, and ^{100}Sn. *Phys. Rev. Lett.*, 101:252501, Dec 2008.

[58] R. D. Evans. The Atomic Nucleus. Krieger, New York, 1982.

[59] A. H. Compton. A Quantum Theory of the Scattering of X-rays by Light Elements. *Phys. Rev.*, 21:483–502, May 1923.

[60] O. Klein, Y. Nishina. Über die Streuung von Strahlung durch freie Elektronen nach der neuen relativistischen Quantendynamik von Dirac. *Zeitschrift für Physik*, 52(11-12):853–868, 1929.

[61] T. Glasmacher. Coulomb excitation at intermediate energies. *Annual Review of Nuclear and Particle Science*, 48(1):1–31, 1998.

[62] S. Agostinelli, J. Allison, K. Amako, J. Apostolakis, H. Araujo, P. Arce, M. Asai, D. Axen, S. Banerjee, G. Barrand,*et al.* Geant4 a simulation toolkit. *Nuclear Instruments and Methods in Physics Research Section A: Accelerators, Spectrometers, Detectors and Associated Equipment*, 506(3):250 – 303, 2003.

[63] T. Baugher *et al.* Simulations of CAESAR. In preparation.

[64] J. W. Mayer. Semiconductor detectors for nuclear spectrometry, II. *Nuclear Instruments and Methods*, 43(1):55 – 64, 1966. Proceedings of the Tenth Summer Meeting of Nuclear Physicists.

[65] D. Swan, J. Yurkon, D. J. Morrissey. A simple two-dimensional PPAC. *Nuclear Instruments and Methods in Physics Research Section A: Accelerators, Spectrometers, Detectors and Associated Equipment*, 348(23):314 – 317, 1994.

[66] F. Lidn, J. Nyberg, A. Johnson, A. Kerek. Identification of charged particles using plastic phoswich detectors. *Nuclear Instruments and Methods in Physics Research Section A: Accelerators, Spectrometers, Detectors and Associated Equipment*, 253(2):305 – 306, 1987.

[67] H. J. Wollersheim, D. E. Appelbe, A. Banu, R. Bassini, T. Beck, F. Becker, P. Bednarczyk, K.-H. Behr, M. A. Bentley, G. Benzoni, *et al.*. Rare ISotopes INvestigation at GSI (RISING) using gamma-ray spectroscopy at relativistic energies. *Nuclear Instruments and Methods in Physics Research Section A: Accelerators, Spectrometers, Detectors and Associated Equipment*, 537(3):637 – 657, 2005.

[68] A. Gade, D. Bazin, C. M. Campbell, J. A. Church, D. C. Dinca, J. Enders, T. Glasmacher, Z. Hu, K. W. Kemper, W. F. Mueller, *et al.* Detailed experimental study on intermediate-energy Coulomb excitation of ^{46}Ar. *Phys. Rev. C*, 68:014302, Jul 2003.

[69] G. Hagen, M. Hjorth-Jensen, G. R. Jansen, R. Machleidt, T. Papenbrock. Evolution of Shell Structure in Neutron-Rich Calcium Isotopes. *Phys. Rev. Lett.*, 109:032502, Jul 2012.

[70] I. G. Darby, R. K. Grzywacz, J. C. Batchelder, C. R. Bingham, L. Cartegni, C. J. Gross, M. Hjorth-Jensen, D. T. Joss, S. N. Liddick, W. Nazarewicz, *et al.* Orbital Dependent Nucleonic Pairing in the Lightest Known Isotopes of Tin. *Phys. Rev. Lett.*, 105:162502, Oct 2010.

[71] D. Seweryniak, M. P. Carpenter, S. Gros, A. A. Hecht, N. Hoteling, R. V. F. Janssens, T. L. Khoo, T. Lauritsen, C. J. Lister, G. Lotay, *et al.* Single-Neutron States in ^{101}Sn. *Phys. Rev. Lett.*, 99:022504, Jul 2007.

[72] T. Bäck, C. Qi, B. Cederwall, R. Liotta, F. Ghazi Moradi, A. Johnson, R. Wyss, R. Wadsworth. Transition probabilities near ^{100}Sn and the stability of the $N = Z = 50$ shell closure. *Phys. Rev. C*, 87:031306, Mar 2013.

[73] K. L. Yurkewicz, D. Bazin, B. A. Brown, C. M. Campbell, J. A. Church, D. C. Dinca, A. Gade, T. Glasmacher, M. Honma, T. Mizusaki, *et al.* Nuclear structure in the vicinity of $N = Z = 28$ ^{56}Ni. *Phys. Rev. C*, 70:054319, Nov 2004.

[74] B. A. Brown. New Skyrme interaction for normal and exotic nuclei. *Phys. Rev. C*, 58:220–231, Jul 1998.

[75] E. Chabanat, P. Bonche, P. Haensel, J. Meyer, R. Schaeffer. A Skyrme parametrization from subnuclear to neutron star densities Part II. Nuclei far from stabilities. *Nuclear Physics A*, 635(12):231 – 256, 1998.

[76] J. Bartel, P. Quentin, M. Brack, C. Guet, H.-B. Hkansson. Towards a better parametrisation of Skyrme-like effective forces: A critical study of the SkM force. *Nuclear Physics A*, 386(1):79 – 100, 1982.

[77] H. W. Fulbright, C. L. Bennett, R. A. Lindgren, R. G. Markham, S. C. McGuire, G. C. Morrison, U. Strohbusch, J. Toke. Four-nucleon transfer via the (^{6}Li, d) reaction. *Nuclear Physics A*, 284(2):329 – 364, 1977.

[78] M. Honma, T. Otsuka, B. A. Brown, T. Mizusaki. New effective interaction for pf-shell nuclei and its implications for the stability of the $N = Z = 28$ closed core. *Phys. Rev. C*, 69:034335, Mar 2004.

[79] R. E. Shroy, A. K. Gaigalas, G. Schatz, D. B. Fossan. High-spin states in odd-mass $^{113-119}$Sb: $\Delta J = 1$ bands on $\frac{9}{2}^+$ proton-hole states. *Phys. Rev. C*, 19:1324–1343, Apr 1979.

[80] H. Schnare, D. R. LaFosse, D. B. Fossan, J. R. Hughes, P. Vaska, K. Hauschild, I. M. Hibbert, R. Wadsworth, V. P. Janzen, D. C. Radford, *et al.* Smooth termination of intruder bands in $^{109}_{51}$Sb. *Phys. Rev. C*, 54:1598–1609, Oct 1996.

[81] T. Otsuka, T. Suzuki, R. Fujimoto, H. Grawe, Y. Akaishi. Evolution of Nuclear Shells due to the Tensor Force. *Phys. Rev. Lett.*, 95:232502, Nov 2005.

[82] G. A. Leander, J. Dudek, W. Nazarewicz, J. R. Nix, Ph. Quentin. Single-particle levels in the doubly magic ^{132}Sn and ^{100}Sn nuclei. *Phys. Rev. C*, 30:416–419, Jul 1984.

[83] I. N. Borzov, S. A. Fayans, E. Krömer, D. Zawischa. Ground state properties and β-decay half-lives near ^{132}Sn in a self-consistent theory. *Zeitschrift für Physik A Hadrons and Nuclei*, 355(1):117–127, 1996.

[84] H. Koura, M. Yamada. Single-particle potentials for spherical nuclei. *Nuclear Physics A*, 671(14):96 – 118, 2000.

[85] R. Krücken. Probing Shell Closures in Neutron-Rich Nuclei. *Proceedings of the 4th international Conference on Fission and Properties of Neutron-rich Nuclei, Sanibel Island*, pages 96–101, 2008.

[86] W. J. Gerace, A. M. Green. The effect of deformed states in the Ca isotopes. *Nuclear Physics A*, 93(1):110 – 132, 1967.

[87] B. H. Flowers, L. D. Skouras. Deformed state admixtures in mass-42 nuclei. *Nuclear Physics A*, 136(2):353 – 384, 1969.

[88] V. M. Bader, A. Gade, D. Weisshaar, B. A. Brown, T. Baugher, D. Bazin, J. S. Berryman, A. Ekström, M. Hjorth-Jensen, S. R. Stroberg, *et al.* Quadrupole collectivity in neutron-deficient Sn nuclei: ^{104}Sn and the role of proton excitations. *Phys. Rev. C*, 88:051301, Nov 2013.

[89] H. L. Crawford, R. M. Clark, P. Fallon, A. O. Macchiavelli, T. Baugher, D. Bazin, C. W. Beausang, J. S. Berryman, D. L. Bleuel, C. M. Campbell, *et al.* Quadrupole Collectivity in Neutron-Rich Fe and Cr Isotopes. *Phys. Rev. Lett.*, 110:242701, Jun 2013.